REVIEW ARTICLE

Check for updates

Trends in the energy and environmental applications of metal–organic framework-based materials

Mohammed Yusuf,*[a] Irina Kurzina,[a] Gulnara Voronova,[a] Md. Monjurul Islam,[b] Salisu Danlami Mohammed[c] and Nurudeen Abiola Oladoja [ID] *[d]

Over the past 20 years, metal–organic framework (MOF) nanosheets have garnered a great deal of interest in the fields of energy and environmental management because of their inherent extraordinary qualities. These qualities include the vast surface areas, nanoscale and tunable pore sizes, adaptable structures and functions, good thermal and chemical stability, high aspect ratios, more exposed accessible active sites, flexible functionality, high electrical conductivity, and optical transparency. An overview of the current advancements in the applications of MOF-based materials in environmental science and renewable energy is provided in this review. Precisely, the advancements, advantages, history and characterization of MOF-based materials are first presented and discussed. Next, we focused on the use of MOF-based materials in the fields of environmental cleaning and monitoring, particularly for the treatment of wastewater and air purification, and energy storage and conversion. We concluded by summarizing the findings on the current state-of-the-art advancements and sharing the perspectives on the prospects and problems facing future research on MOF-based materials.

1. Introduction

The intriguing structures of MOFs and their notable physical attributes, such as tunable pore size, large pore volume, high specific surface area, and the potential for case-specific customization of fundamental molecular architecture, make them an ideal platform for applications in energy storage and environmental management.[1,2] MOFs are crystalline porous solids that are made up of organic ligands and metal ions connected by coordination bonds between the metal ions/clusters and the

[a] *Institute of Smart Material and Technologies, National Research, Tomsk State University, 36 Lenin Ave, Tomsk, 634050, Russia. E-mail: dr.yusuf@mail.tsu.ru; Tel: +2348055438642, +79911181720*

[b] *School of Engineering, RMIT University, VIC 3001, Australia*

[c] *Department of Water Resources Engineering, Kaduna Polytechnic, P.M.B 2021, Kaduna, Nigeria*

[d] *Hydrochemistry Research Laboratory, Department of Chemical Sciences, Adekunle Ajasin University, Akungba Akoko, Nigeria. E-mail: bioladoja@yahoo.com, nurudeen.oladoja@aaua.edu.ng*

Mohammed Yusuf received both his MSc and PhD in Chemical and Environmental Engineering from Universiti Putra Malaysia (UPM) and Universiti Teknologi Malaysia (UTM) respectively. He previously worked as Research Assistant Professor at Tokyo University of Agriculture and Technology Japan. He also worked as an Environmental Consultant at Oil and Gas Company in Al-Khobar, Saudi Arabia. Furthermore, he worked as a Post-doctoral Research Fellow at Chinese Academy of Sciences Wuhan, China and Hanyang University Seoul, South Korea. Presently, he is working as an Associate Professor at Tomsk State University Russia. His current research is directed towards the development of composite materials and their utilization as an adsorbent for the abatement of organic and inorganic pollutants from both domestic and industrial wastewater.

Nurudeen Abiola Oladoja is a Professor and Chair of the Hydrochemistry Research Group, Department of Chemical Sciences, Adekunle Ajasin University, Akungba Akoko, Nigeria. He is also the Head of the Applied Research Unit at the African Centre of Excellence for Water and Environmental Research (ACEWATER), Redeemer's University, Ede, Nigeria. His research has focused on environmental interfacial chemistry, aquatic ecological engineering, and resource recovery from wastewater.
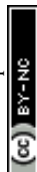
organic ligands.[3] The majority of metals used are the transition metals from the d-block (Ti^{4+}, Zr^{4+}, V^{3+}, Cr^{3+}, Fe^{3+}, Mn^{2+}, Ni^{2+}, Cu^{2+}, Zn^{2+}, and Cd^{2+}) or other s-block (Mg^{2+})/p-block (Al^{3+} and Ga^{3+}) metals. A small number of metals are also employed from the lanthanide/actinide series. The ligands are the donors that contain nitrogen or oxygen functional groups, which act as the linkers between the metal ions.[4] Metal ions are modeled as nodes in the MOF structure, leading to the formation of intricate configurations with hydroxy or oxide anions, ranging from trimmer to octa-nuclear.[5] Depending on whether or not guest molecules are present, MOFs are grouped according to their dimensionality, and because structures of the MOFs are distinct, they exhibit distinctive structural dimensionality on the order of 1D, 2D, or 3D.[6]

MOFs are characterized by their high porosity, which allows for up to 90% of free space, and exhibit a high specific surface area of around 6000 m^2 g^{-1}.[7] MOFs have a wide range of desirable features, which include high porosity, large surface area, and chemical and thermal stability.[8] When there are no guest molecules present in the MOFs' pores, the porosity of the material is maintained, and the pore structure maintains its porosity, even when the guest molecules are eliminated.[9] Materials with special qualities are created by combining elements of organic and inorganic structures. MOFs are distinguished by their notable pore volume, which accounts for at least 50% of the overall volume and their exceptional strength.[10] The selection of the starting building units allows for the modification of a number of parameters, which include the pore size (increasing the pore diameter to 98 Å),[11] density (decreasing to 0.126 g cm^{-3}),[12] and specific surface area (up to 1000–10 000 m^2 g^{-1}).[13]

In this discourse, we showcase the trend in the development of MOF nanosheets for the purpose of energy and environmental applications. In order to achieve the aim of this review, we have provided a brief introduction to the structural advantages of MOFs as well as their physical properties (such as stability, pore characteristics, and surface area) for practical applications. An overview of noteworthy advancements in the use of MOFs for energy storage systems (*i.e.*, supercapacitors, batteries, solar cells, and fuel cells) is presented. The important developments in MOFs in the area of environmental applications, *i.e.*, in the adsorptive removal of dyes and heavy metal contaminants from water and hazardous gases from the environment, were covered. The challenges and future prospects for environmental cleanup were discussed, and perspectives on the future directions in this field of research were highlighted.

1.1 Emergence of MOFs

The first mention of MOFs dates back to 1897, when $Ni(CN)_2(NH_3) \cdot C_6H_6$, a coordination network bonded *via* the CN groups, was described in ref. 14. The molecule's crystal structure was not confirmed until 1952, when it was discovered to be a layered, square network of $Ni(CN)_2(NH_3)$ groups with benzene occupying the channels, indicating that the structure is an extended network.[15] With copper(I) as the metal node and

organic nitrogen ligand as the linker, Robinson's research groups worked on the creation of a coordination polymer in 1989. They reported the synthesis of $\{Cu^I[C(C_6H_4 \cdot CN_4)]\}_n$, a polymer with 3-D network architecture, which served as the initial step toward the development of the metal–organic frameworks when they brought the idea of topology into coordination polymers for the first time.[16] In 1990, Hoskins and colleagues discovered porous coordination polymers that demonstrated ion exchange capabilities, marking the beginning of the development of functional microporous materials.[17] The heterogeneous catalyst $\{Cu^I[C(C_6H_4 \cdot CN_4)]\}_n$ for the cyanosilylation of aldehydes was effectively prepared from a 2-D square network material created by the Japanese professor Fujita in 1994 using $Cd(NO_3)_2$ and 4,4-bipyridine. This material can readily form clathrates with certain aromatic guests with a specific shape. As a result, Fujita postulated that the reaction's selectivity will be influenced by the cavity size.[18]

It was not until 1995 that Yaghi and associates began referring to these materials as metal–organic frameworks.[19] A multilayer material made of pyridine, octahedral Co centers, and 1,3,5-benzenetricarboxylate was successfully designed and synthesized, and it was able to bind aromatic molecules like benzene both reversibly and selectively. Meanwhile, as an alternative to zeolites and activated carbon, Omar M. Yaghi and colleagues synthesized a groundbreaking substance known as MOF-5, which is said to be the first strong and highly porous material.[20]

In 2002, a number of Zn dicarboxylates gained popularity, but the concept of isoreticular chemistry[21] was also applied to other materials. In particular, it has been found that the mixed-linker compounds $[M_2(dicarboxylate)_2(diamine)]$ (M = Zn, Cu) are a versatile class, and several experiments have been carried out by altering the two organic components.[22] The imidazolate-based compounds, now referred to as zeolitic imidazole frameworks (ZIFs),[23] were added to the MOF family in 2003.

1.2 Characterization of MOF based materials

Below is a summary of the instrumentation techniques investigated for the characterization of MOFs and their derivatives.

The microstructure of MOF materials is extensively studied using scanning electron microscopy (SEM), which offers insights into morphology, topography, crystal structure, compositional changes, phase distribution, and defect location.[24] In order to investigate the form and porous structure of microscale adsorbents, the analysis can be carried out at low magnification ($<1000\times$) or high magnification ($>30\,000\times$) for nanoscale adsorbents, such as aggregate formation in metal–organic frameworks (MOFs).[25] In order to evaluate adsorbents post-processing and following adsorption/desorption cycles, this method is helpful for determining materials' stability.[26] The SEM image of yttrium-based metal oxide fillers (Y-MOFs), which is depicted in Fig. 1a, uncovered well-dispersed, sphere-like structures that ranged in size from 3 to 5 μm. The spheres are filled with nanosheets (200 nm wide and 40–50 nm thick), which resemble *Allium giganteum* (see the inset in Fig. 1b) in the extended pictures (Fig. 1b and c).
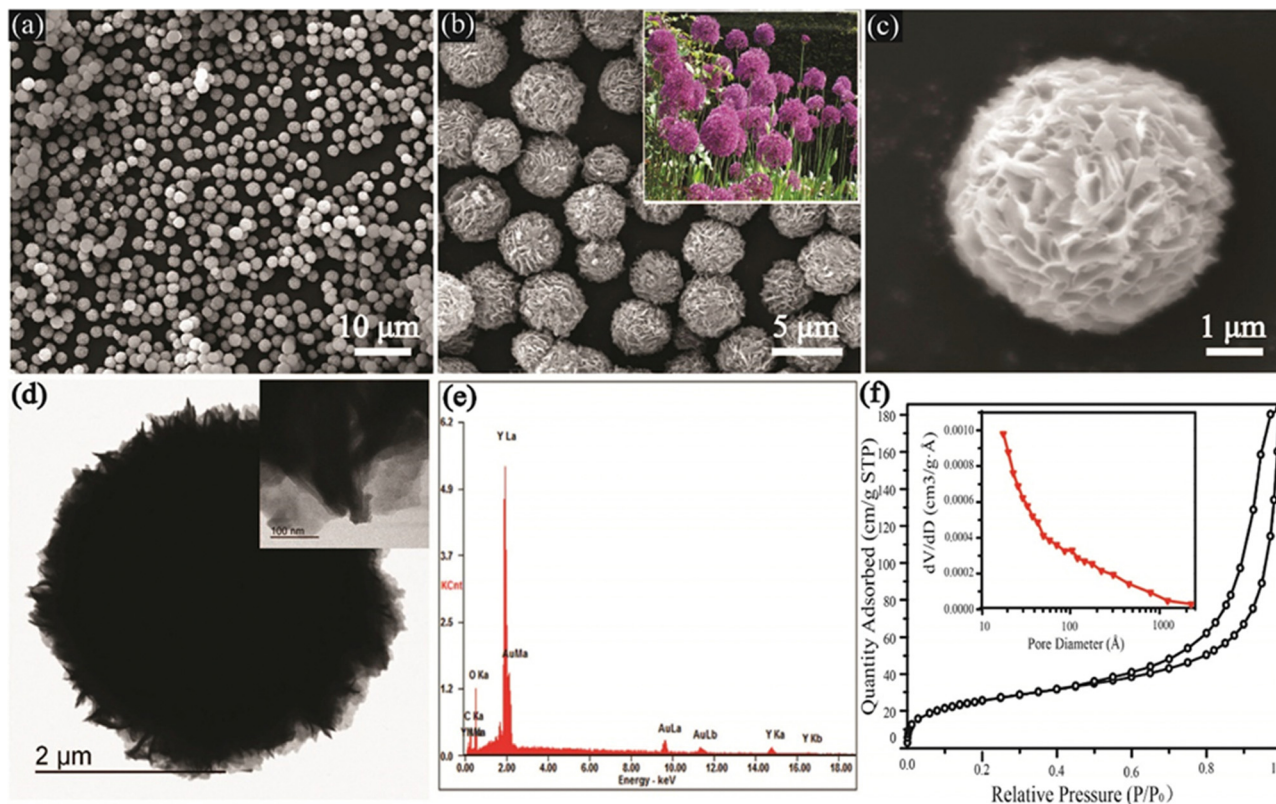
Fig. 1 SEM and TEM images of as-prepared Y-MOF samples at 120 °C for 24 h: (a)–(c) low- and high-magnification SEM images (inset in (b) is the photo of *Allium giganteum*);[26] (d) low- and high-magnification TEM images; (e) EDX spectrum;[26] (f) nitrogen adsorption/desorption isotherms of Y-MOFs:10%Eu^{3+} (inset is pore size distribution).[27]

Particle form, thickness, and size may all be determined as well as defects such as vacancies and dislocations by using transmission electron microscopy (TEM), which is also used to examine the chemical and electrical structures of materials.[28] TEM is perfect for analyzing very small adsorbents because, unlike SEM, it requires the electron beam to pass through the sample. In order to determine metal distribution, agglomeration, crystal size, and particle form on substrates, TEM is frequently used with MOFs.[29] These data facilitate the development of separation techniques and the study of adsorbent behavior in solutions. A TEM image of Y-MOFs, which were synthesized in ref. 26, is shown in Fig. 1d. The analysis reveals radially oriented nanosheets. The presence of C, Y, O, and N is confirmed by energy-dispersive X-ray spectroscopy (EDX) in Fig. 1e, which is in line with the composition of Y-MOFs.

It is possible to determine the MOFs' surface area, pore volume, and pore size distribution using adsorption isotherms of non-reactive gases at cryogenic temperatures. For pores smaller than 0.7 nm, argon at 87.3 K is preferable, but N$_2$ adsorption at 77 K produces an isotherm in this case.[30] N$_2$ adsorption at 77 K indicated a surface area of 2021 m^2 g^{-1}, pore width of 11.7 Å, and pore volume of 0.882 cm^3 g^{-1} for the Ni-MOF produced in ref. 31 utilizing ultrasound irradiation. Their investigation produced MOFs with textural properties that were different from those found in earlier studies on surface areas

and pore volumes, possibly due to ultrasonication. The N$_2$ adsorption–desorption isotherm and pore size distribution of the Y-MOF:10%Eu^{3+} sample are shown in Fig. 1f. Based on IUPAC standards, this isotherm is categorized as type IV with a hysteresis loop.[27] According to Yang *et al.*,[26] Y-MOFs have an average pore diameter of 12.5 nm and a BET surface area of about 90.1 m^2 per g 10% Eu^{3+}.

The identification of IR-active functional groups inside MOFs is a well-established use of Fourier-transform infrared spectroscopy (FT-IR), which is essential for investigating the adsorption performance of MOFs.[32] For example, FT-IR peaks at 1400–1767 cm^{-1} for cross-linked terephthalic acid indicate the presence of carboxylic groups (–CO$_2$), whereas peaks at 1650–1767 cm^{-1} for non-reacted terephthalic acid are observed.[33] A new gadolinium–porphyrin MOF nanosheet was produced and FT-IR characterization was performed[34] (Fig. 2a). The researchers detected absorption peaks at 963 cm^{-1} and 3315 cm^{-3}, which correspond to in-plane vibrations and N–H stretching, respectively. They also noted alterations in peak intensities subsequent to coordination with gadolinium ions (Gd). While the C=O stretching vibration of carboxyl groups dramatically attenuated to 1683 cm^{-1} upon coordination, the C=C stretching vibration of porphyrin showed a new peak at 1651 cm^{-1} and vibration at 1683 cm^{-1}. Furthermore, a decreased peak at 1485 cm^{-1} owing to sulfonic acid groups
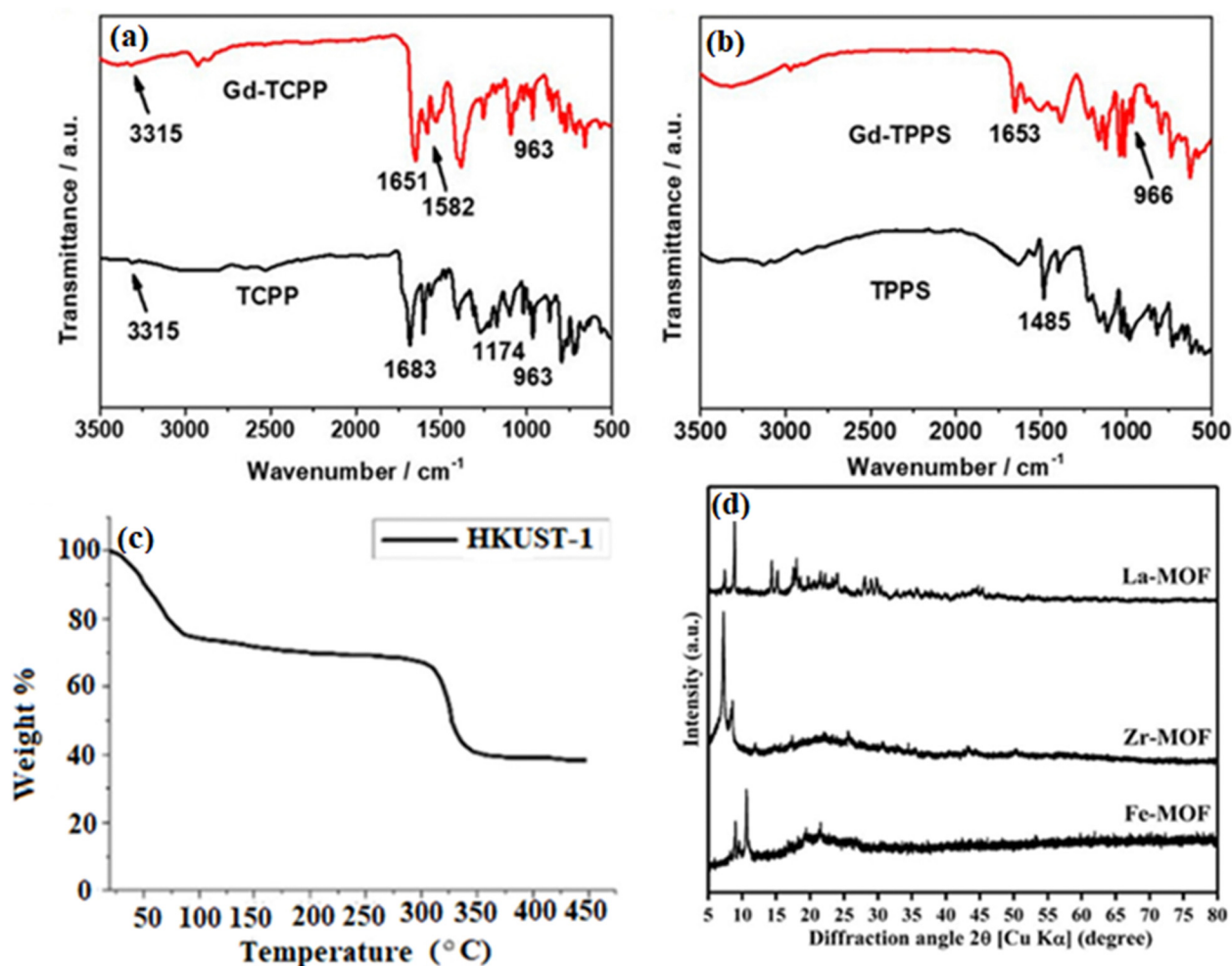
Fig. 2 (a) FT-IR analysis of TCPP and Gd-TCPP.[34] (b) FT-IR analysis of TPPS and Gd-TPPS. (c) Thermogravimetric analysis (TGA) of HKUST-1.[35] (d) Powder X-ray diffraction (PXRD) spectra of Fe-, Zr-, and La-based metal–organic frameworks derived from recycled PET plastic bottles.[36]

and a peak at 1582 cm^{-1} ascribed to the MOF structure's skeletal vibrations were seen (Fig. 2b shows the corresponding results for Gd-TPPS).

In order to determine impurities, unreacted precursors, and breakdown temperatures, thermogravimetric analysis (TGA) profiles are first acquired for freshly synthesized MOFs (pre-activation).[37] MOFs break down in several ways based on the carrier gas (air, O_2, or N_2). To determine which compounds are producing mass changes and temperature variations, mass spectrometry and TGA are frequently employed in tandem.[10] For HKUST-1 samples evaluated within a specific temperature range, the TGA curve in Fig. 2c shows a two-stage thermal breakdown. It is possible that the removal of lattice water/ethanol occurs in the first step (50–125 °C), and the thermal degradation of the organic ligand occurs in the second stage (300–400 °C).[35]

The main technique for accurately figuring out the atomic arrangement and structure of MOF materials in single crystals is X-ray diffraction (XRD). PXRD, or powdered X-ray diffraction, is used to describe MOFs when single-crystal XRD is not feasible because of the size of the crystal. PXRD spectra with sharp diffraction peaks reveal the bulk MOF materials' crystallinity and structural details. To verify the authenticity of a product, experimental powder patterns can be compared with patterns predicted from single crystal structures or computational models.[38] PXRD analysis of Fe-, Zr-, and La-based MOFs made from recycled PET plastic bottles was performed in ref. 36 (Fig. 2d). For example, the production of Fe-BDC was confirmed by sharp (001) and (101) peaks at 9.5° and 10.7°.[39] According to He et al.,[40] the Zr-MOF displayed (111) and (002) peaks at 7.14° and 8.55°, respectively, suggesting intercalated molecular layers. Furthermore, Zr-MOF crystal planes were correlated with strong peaks at 11.87°, 14.71°, 17.33°, 25.73°, and 30.71°.[41] Similar to this, the La-MOF showed crystalline peaks that corresponded to different crystal planes at 15.19°, 23.97°, 28.95°, and 32.87°.[42]

2. Energy applications of MOFs

2.1 MOFs for supercapacitors

Supercapacitors, also referred to as electrochemical capacitors or ultra-capacitors, are some of the most promising energy
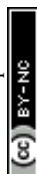
storage technologies that are gaining international interest from researchers because of their special qualities, which include high power density, long cycling life, and quick charge rates.[43] Since pure MOF SCs have poor conductivity, they often have low specific capacitance despite having significant porosities. A new method for enhancing SC performance involves incorporating MOFs with conductive materials, like graphene and conductive polymers, to increase MOF conductivity. Supercapacitors can be primarily divided into three groups based on the principal charge-storage mechanism, electrode/electrolyte interface, and active materials utilized. (1) *Via* an electrochemical double-layer capacitor (EDLC) using electrostatic forces, electrical energy is transferred to their inside surfaces. By allowing electrolyte ions to adhere to the surface of electrode materials, the carbon-based electrodes, or their derivatives, are utilized to store charge.[44] Carbon-based active materials having large surface areas, such as microporous or mesoporous carbon,[45] graphene,[46] carbon nanotubes,[47] and so on, are typically used in these kinds of SCs. (2) Fast and reversible surface redox reactions are the foundation of pseudocapacitors. Typical examples of active materials in pseudocapacitors are transition metal oxides and conductive polymers,[48] and (3) hybrid supercapacitors (HSCs) combine a capacitive electrode with a battery-type electrode (such Li/Na-ion type electrodes) in an electrochemical cell to provide high energy and high power densities.[49]

Excellent energy storage capabilities and high power densities can be achieved by utilizing various electrode materials, such as carbon-based electrodes for electrostatic double-layer supercapacitors or transition metal oxide electrodes for pseudocapacitors. Key factors include high conductivity, large surface areas, and convenient electrolyte access to active sites.[50] Because of the coexistence of organic and metal components in MOFs, materials based on MOFs typically have high surface areas and porous architectures that provide enough electroactive sites for supercapacitors, particularly EDLCs and HSCs. While a great deal of studies have been done on using MOFs as templates to create nanostructured materials like metal oxides or nanoporous carbon, nano-MOFs in different shapes such as particles, rods, and sheets have also been studied for use as supercapacitor electrodes. When creating electrodes, the controlled porous structure of nano-MOFs offers much-desired benefits like low density and extraordinarily large exterior surface area. Furthermore, in contrast to practically inert commercial porous carbon electrodes, the presence of redox-active metal centers may enhance pseudo-capacitance.[50] Depending on the electrode materials, MOFs can be used in three different ways: (i) utilizing pristine MOFs to store charges by physisorption of electrolyte ions on their internal surfaces or by taking advantage of reversible redox reactions of the metal centers; (ii) breaking down MOFs to obtain metal-oxides and preserving electrons through the charge transfer between the electrode and electrolyte; and (iii) pyrolyzing MOFs to yield porous carbons and increasing capacitance by increasing conductivity.[44]

A porous MOF $Ni_3(HITP)_2$ (HITP = 2,3,6,7,10,11-hexaiminotriphenylene) with electrical conductivity has been studied for its possible application in ref. 51; when compared to the bulk electrical conductivity (>5000 S m^{-1}) of porous graphite and active carbon (≈ 1000 S m^{-1}), the EDLC behavior (Fig. 3) indicates 1D channels (≈ 1.5 nm in diameter).[51] This is supposedly the first known instance of a supercapacitor made completely of pure MOFs as active materials, devoid of any binders or conductive additives. At a low discharge rate of 0.05 A g^{-1}, the $Ni_3(HITP)_2$ electrodes had a very high surface area normalized capacitance of 18 mF cm^{-2} and a satisfactory gravimetric capacitance of 111 F g^{-1}, which was among the highest values reported for most carbon material-based supercapacitors.[52] With over 90% capacity retention after 10 000 cycles, this MOF-based device demonstrated superior cycling performance and exhibited a high areal capacitance that surpassed most carbon-based materials.

For high-performance supercapacitors, MOFs with high electrical conductivities are therefore created as appropriate electrode materials based on the aforementioned principles. For instance, Li et al.[55] used a bottom-up synthetic approach to integrate Cu–HHTP single crystal nanowires onto carbon fibers to create conductive MOF nanowire arrays (NWAs). These NWAs were then grown on carbon fiber paper to create nanowire arrays of a copper-MOF that were 200–250 nm in diameter and 3–15 mm in length. The NWAs were then used as electrodes for solid-state supercapacitors.[55] Effective charge/electron transfer at the MOF NWAs/electrolyte interface was made possible by the NWA electrode's significant reduction of the inherent resistance and charge transfer resistance at the electrode/electrolyte interface. The Cu–HHTP NWA electrode demonstrated a high specific capacitance of 202 F g^{-1} at a current density of 0.5 A g^{-1}, which was twice as high as those of the Cu–HHTP powder electrode. This was made possible by the composite's high porosity and strong conductivity. With a strong rate performance, the symmetric solid-state supercapacitor made with Cu–HHTP NWA electrodes had a high surface area-normalized capacitance of ~ 22 μF cm^{-1}. Surprisingly, this work also showed that by manipulating the morphologies from the randomly shaped crystallite to the strongly oriented NWAs, which fully utilized their high porosity and conductivity, their electrochemical performances (e.g., rate performance and capacitance) could be improved.

Another advancement in increasing MOF conductivity was made in ref. 53, where MOFs were combined with conductive materials like graphene and conductive polymers, resulting in a novel approach for enhancing SC performance. The highest SC performance was demonstrated by $Zr_6O_4(OH)_4(BPYDC)_6$ (BPYDC = 2,2-bipyridine-5,5-dicarboxylate, termed nMOF-867), among the 23 distinct nanocrystalline MOFs that were examined. Its performance could be maintained for at least 10 000 cycles. Its stack and areal capacitances were 0.64 and 5.09 mF cm^{-2}, respectively. It was shown that MOF-801 nanocrystals, measuring approximately 100 nm, performed better than those measuring 500 nm. This was likely due to the ease with which electrolyte ions could diffuse into these tiny crystals. Liu et al.[56] reported the first preparation of NPCs using MOF-5-FA composites (FA = furfuryl alcohol) as a secondary carbon
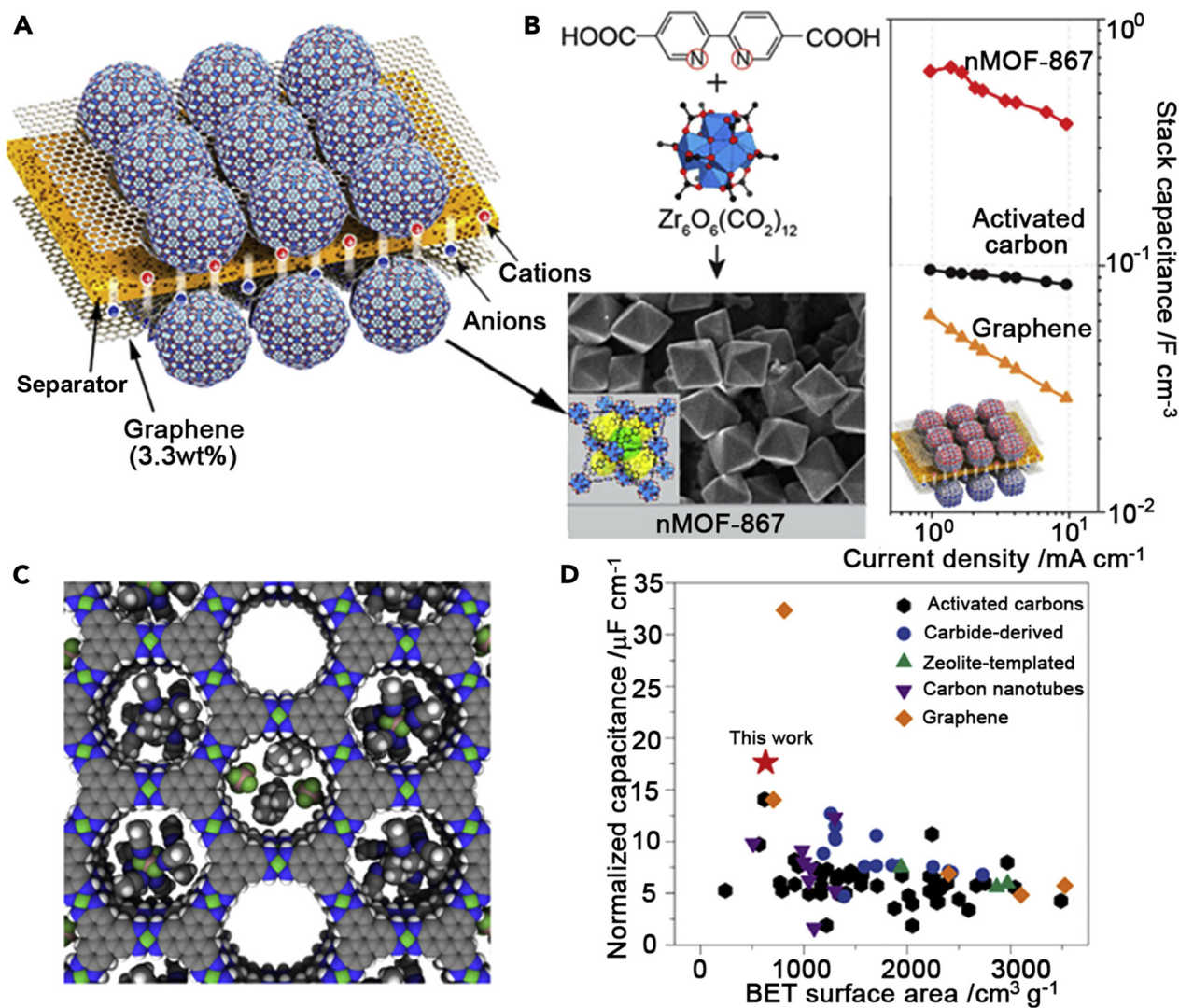
Fig. 3 MOF-based supercapacitors. (A) Schematic construction of MOF supercapacitors.[53] (B) Structure and nanocrystal morphology of nMOF-867 and comparison of stack capacitances among various EDLC materials.[51] (C) A space-filling diagram of idealized $Ni_3(HITP)_2$ (Ni, green; F, lime; N, blue; C, gray; B, brown; H, white).[51] (D) Comparison of BET-surface-area-normalized areal capacitances among various EDLC materials.[54]

source. The as-synthesised carbon electrode in 1.0 M H_2SO_4 electrolyte demonstrated the exceptional performance of the MOF-derived NPCs for the EDLCs, providing a capacitance of 204 F g^{-1} at a sweep rate of 5 mV s^{-1}. The Ni-based MOF electrode's structural layer structure demonstrated capacitances of 1127 and 668 F g^{-1} at rates of 0.5 and 10 A g^{-1}, respectively, as reported by Yang et al.[57] An aqueous solution containing 6 M KOH was used to study the electrochemical behavior of the electrode, which was created by pressing a paste consisting of a 70 wt% Ni-based MOF combined with 20 wt% acetylene black and 10 wt% polytetrafluorethylene (PTFE) binders onto a stainless steel plate. Over a 3000 cycle period, the PTFE binder demonstrated over a 90% cycle lifetime and a specific capacitance of 1127 F g^{-1} at 0.5 A g^{-1}. The greatest exposed (1 0 0) facets and layered structural characteristics were found to be highly advantageous for the kinetics of surface redox reactions and the diffusion of charged species, which

explains why the material showed a satisfactory high specific capacitance and outstanding rate capability.

In a related breakthrough, Wang et al.[58] reported the creation of a flexible MOF-based supercapacitor using a two-step fabrication technique that involved coating ZIF-67 nanocrystals (~300 nm) on a carbon cloth first and then electrochemically weaving polyaniline onto the cloth.

PANI electrochemically connected ZIF-67 had been chosen, after it had been first coated on carbon cloth; the resulting electrode was designated as PANI-ZIF-67-CC. Using polyaniline, which allowed electrons to reach the MOF surface and the open MOF pores, which made electrolyte diffusion simple, a very high areal capacitance of 2146 mF cm^{-2} at 10 mV s^{-1} was achieved. Additionally, two symmetric freestanding PANI-ZIF-67-CC electrodes were used to create a flexible solid-state SC device. After 2000 cycles, the SCC still maintained more than 80% of its initial capacitance and produced an amazing

areal capacitance of 35 mF cm^{-2} at a current density of 0.05 mA cm^{-2}.

According to Feng et al.,[59] 2D black MOFs, Cu-HAB and Ni-HAB, with an ultra-small hexaaminobenzene (HAB) linker demonstrated hexagonal pore packing with d_{100} = 1.5 nm, which in turn produced extremely dense skeletons with superior capacitive behaviors for electrochemical supercapacitors that are submillimeter thick. In 1 m KOH, both HAB MOF electrodes demonstrated distinct reversible redox behaviors in addition to having sizable gravimetric capacitances of 215 F g^{-1} for Cu-HAB and 420 F g^{-1} for Ni-HAB. It has been determined that the main mechanism of charge storage was pseudocapacitance from ligand-based reversible redox processes, with a small contribution from EDL capacitance ($<10\%$ for Ni-HAB and $<20\%$ for Cu-HAB) obtained from moderate SSA (150–200 m^2 g^{-1}). Additionally, after 12 000 cycles, these HAB MOF electrodes showed good cycling stability with a capacitance retention of almost 90%.

Bi et al.[60] investigated the EDL charge storage and charging dynamics of three 2D c-MOFs (Cu-THQ, Cu-HITP, and Cu-HITN; THQ = tetrahydroxy-1,4-quinone, HITN = 2,3,8,9,14,15-hexaimino-trinaphthalene) using constant-potential molecular dynamics simulations. Experiments on the electrochemical performance of macroscale EDL capacitor devices provided support for the results of the computer models. These 2D c-MOF-based devices demonstrate unprecedentedly large specific capacitances, low cell resistances, and unprecedentedly high energy and power densities. The energy density of the supercapacitors can be further enhanced by the crystalline 2D c-MOFs since they have a wider working voltage range and a greater specific surface area, which allows for a capacity that is almost equal to the theoretical value. Additionally, Li et al., 2020[61] presented a thorough investigation of a carbon material with a partial inheritance of the organized linked macroporous structures. Their research showed that when utilized as the electrode in a supercapacitor, the derivative carbon material demonstrated exceptional rate performances and improved cycle stability. These could be brought about by its enhanced diffusion, stronger structure, and decreased resistance. The technique offered significant promise for creating macro–microporous superstructures for a number of exciting energy storage device applications.

Guan et al.[62] reported the creation of multi-shelled metal sulfide particles with a distinctive hollow structure using a MOF-engaged technique as a battery-like electrode. The Co-based MOF precursor must first be directly pyrolyzed in order to produce the onion-like Co$_3$O$_4$ particles. These multi-shelled Co$_3$O$_4$ spheres can be transformed into NiCo$_2$S$_4$ and Co$_4$S$_3$ particles, which resemble onions, by a sequential ion-change process. Due to their high capacitance and exceptional cycling stability, the complex hollow-structured NiCo$_2$S$_4$ particles exhibit enhanced characteristics as a battery-type electrode. Furthermore, an HSC device based on the combination of these onion-like NiCo$_2$S$_4$ particles and the activated carbon manifests excellent cycling stability, enhanced energy density, and power capability. The enhanced performance may largely be attributed to the complex structure and composition of the onion-like NiCo$_2$S$_4$ particles. Specifically, the complex multi-shelled structure can improve the energy density of the electrode material. Moreover, the porous and hollow structure with much higher specific surface area should also be beneficial for electrochemical applications. In addition, incorporation of Ni^{2+} cations into the cobalt sulfide could result in increased conductivity and the creation of new active sites.

2.2 MOFs for solar cells

By creating electrical charges that are free to move about in semiconductors, solar cells use the photovoltaic effect to directly convert solar energy into electrical energy and produce electricity. In contrast to nuclear power plants and coal-fired power plants, solar cells produce no hazardous emissions during the electricity-producing process, which has led to a recent surge in research into solar cells as an environmentally acceptable energy source. The photovoltaic effect, which occurs when the cell's surface is exposed to light, is the basis for how solar cells function. Common solar cells are made of semiconductor materials, which can absorb light and has a bandgap less than visible light's energy. A cell's internal electric field causes the electrical charges created by this light to move, which results in the flow of electricity. By connecting p- and n-type semiconductors, the external voltage is generated. An electric field is created between the p- and n-type semiconductors at their interface, causing band bending due to the disparity in Fermi energy. Because of the band bending of the p–n junction, electrons transported upon light irradiation to the conduction band can pass from the p-type semiconductor to the n-type semiconductor, generating an electric current that flows along the circuit and is used as energy.

The kind of materials utilized and their composition can be used to classify solar cells. The most widely used type of solar cells are the silicon-based ones, which are further classified as amorphous, hybrid, polycrystalline, and monocrystalline silicon solar cells based on the crystallinity of silicon. When compared to other types of solar cells, single-crystal silicon solar cells have the best light conversion efficiency, but they also have the highest fabrication costs. First-generation solar cells are the name given to such solar cells.[63]

2.2.1 Dye-sensitized solar cells (DSSCs). Due to their advantages of charge separation efficiency and low cost of manufacturing, dye-sensitized solar cells (DSSCs) have drawn significant attention from researchers worldwide for more than 20 years.[64] Owing to these exceptional qualities, dye-sensitized solar cells, or DSSCs, have emerged as a viable option that might both alleviate the world's energy crisis and lead to a breakthrough in power conversion efficiency. A dye-sensitizer that may be obtained from natural resources, titanium dioxide (TiO$_2$), makes up the photoanode of a dye-sensitized solar cell (DSSC). In addition, the photoanode is made up of a thin layer of a conducting, transparent metal oxide that is porous and semiconducting; the most popular metal oxide for this purpose is TiO$_2$. A photosensitizing dye is used to sensitize the metal oxide thin layer. DSSCs can be produced using a roll-to-roll
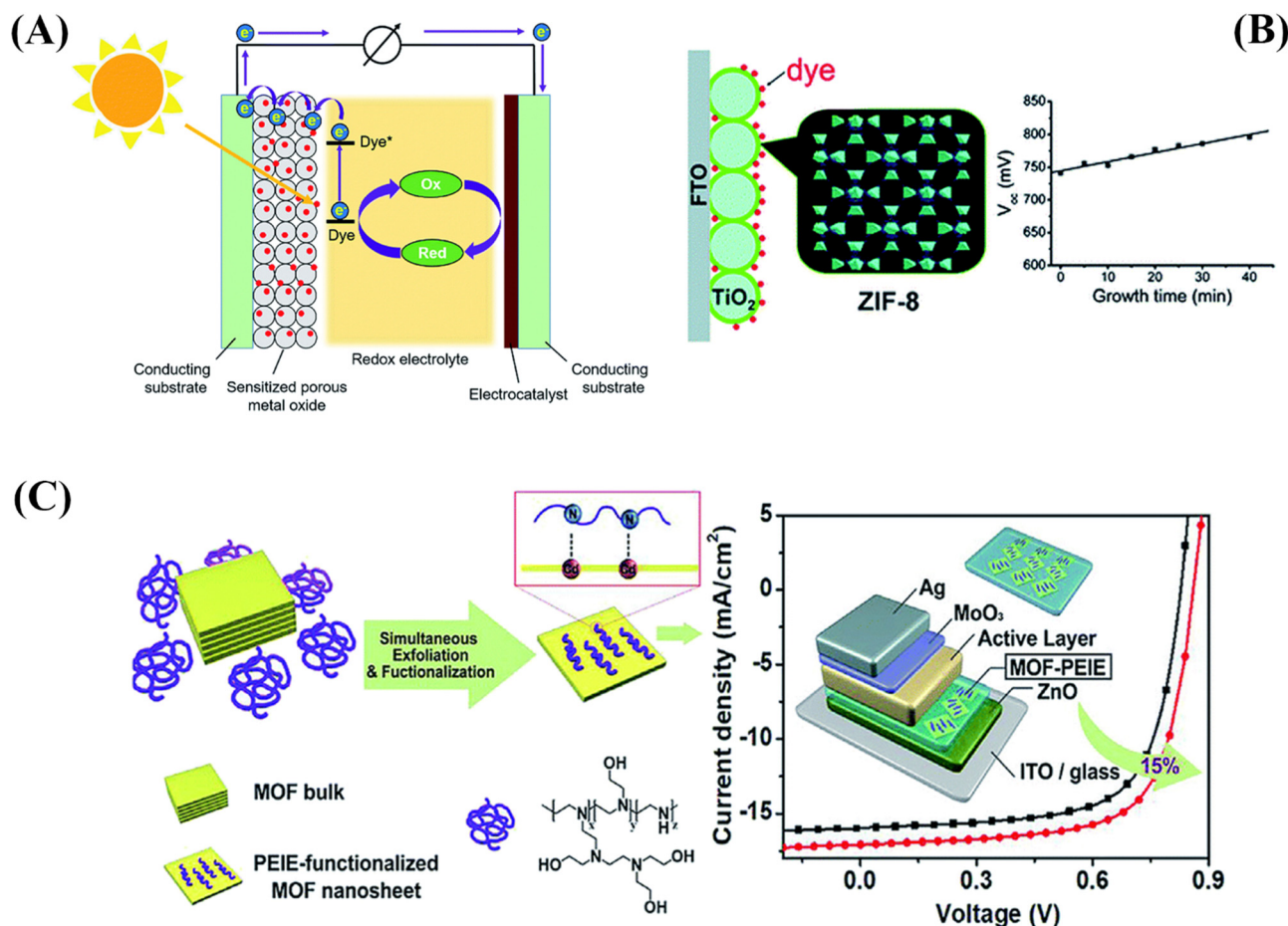
Fig. 4 (A) Schematic representation of typical dye-sensitized solar cells. (B) The use of MOFs for the photoanodes in DSSCs as the blocking layer.[71] (C) Schematic illustration of the preparation of 2D MOF nanosheets and their modified electron-extraction layer for photovoltaic devices.[72]

technique, which is an affordable, continuous printing approach on flexible substrates. The dye molecule absorbs photons from the sun, which results in electron injection into the semiconducting metal oxide's conduction band. As seen in Fig. 4A, the electron moves toward the counter electron CE *via* the outer circuit. The electrocatalyst, which is typically a thin layer of platinum, is placed as a layer on another conducting substrate to form the CE. The space between the CE and the photoanode was filled with an electrolyte solution that contained a redox pair. As DSSCs can operate well with diffused light even under overcast conditions, they can be installed in a variety of spaces, including sunroofs and windows. Due to these benefits, DSSCs have been the subject of extensive research.[65,66] Transition metal materials,[67] metal alloys,[68] carbon materials,[69] and conductive polymers[70] have been used as substitutes for the Pt counter electrode in DSSCs. Although their stability is not as good as that of metal-free electrode materials, carbon materials have a high surface area and electrical conductivity to make up for their drawbacks.

The application of MOFs as semiconductors has been extensively established by experimental and theoretical measurements.[73] Subsequent studies also validate that the semiconducting characteristics of MOFs may be tuned through

metal node size adjustments, organic ligand replacements, and coordination mode adjustment between the organic and inorganic constituents. The potential of MOF-based materials as photoanodes or auxiliaries for electrode sensitization in DSSCs should be explored due to their enormous surface area and capacity to harvest light.

Li *et al.*[71] reported the investigation of a ZIF-8-coated TiO$_2$ hybrid with different thicknesses, which was subsequently effectively applied in a DSSC. As a blocking layer on the photoanode, a thin layer of ZIF-8, a zinc-based zeolitic imidazolate framework, was formed on a TiO$_2$ surface (Fig. 4B). By altering the reaction time, the thin ZIF-8 film's thickness may be precisely regulated. By submerging the built TiO$_2$/ZIF-8 in the dye-containing ethanol solution, electrode sensitization is achieved. The adsorption of dyes is greatly enhanced by the thicker ZIF-8 coating layer. The interfacial charge recombination on the TiO$_2$ surface can be inhibited by the ZIF-8 thin layer, leading to a notably higher open circuit voltage (V_{oc}) than the pure DSSC without ZIF-8. It was also discovered that when ZIF-8 was present on the photoanode, the dye loading was significantly higher. With the ZIF-8 layer's assistance, the cell efficiency increased from 5.11% to 5.34% during the ideal growth period; however, when the growth time increased further, the

cell efficiency decreased because of a sharp decline in the short-circuit current density (J_{sc}).

Lopez et al.[74] reported the development of solar cells employing the MOF thin film consisting of $Al_2(bdc)_3$ (bdc: *p*-benzene dicarboxylate) as the active component in all-solid-state DSSCs. Their investigation showed that, with an optimum thickness of 2.7 mm, $Al_2(bdc)_3$ containing the 1,4-dimethoxybenzene guest molecule performs better than individual components (short-circuit current density = 36 mA cm^{-2}, open-circuit voltage = 0.36 V, and fill factor = 40%). Additionally, materials generated from MOFs may inherit interesting properties from the related MOFs and exhibit high performance as photoanodes. With a pore size of 10 nm and a large Brunauer–Emmett–Teller surface area of 147 m^2 g^{-1}, Dou et al., 2016[75] created a porous TiO_2 hierarchical structure using Ti-MIL-125 as a precursor. With a 7.2% increase in efficiency over commercial TiO_2 (Degussa P25), the as-constructed TiO_2 material has been effectively employed as a photoanode for the DSSC.

2.2.2 MOFs in organic solar cells. Polymer cells composed of carbon-based materials and organic electronics are known as organic solar cells, or OSCs for short. As opposed to the expanding uses in DSSCs and PVSCs, MOFs have not yet been thoroughly investigated in OSCs, and there are currently very few research studies that address this topic. As was previously indicated, using MOFs directly as photoactive materials is very difficult. Moreover, MOF sites in OSCs are limited to interlayer engineering due to the lower semiconducting qualities of organic materials compared to their inorganic counterparts. Plastic solar cells are significantly more robust and have a lot higher coverage area than traditional solar cells, but they lack high PCEs. In contrast, organic solar cells (OSCs) have highly adjustable architectures, are flexible, lightweight, and inexpensive, and are made up of thin films. In order to increase the PCE and stability of OSCs, numerous studies have been carried out.[76–78] Furthermore, compared to silicon solar cells, organic solar cells are far thinner, providing significant material savings that are beneficial to the environment. High conductivity and charge transport mobilities are necessary for the interfacial layers, which include the hole extraction layer and electron extraction layer (EEL), which are critical components of organic solar cells (OSCs). Due to their superior electrical and optical capabilities and wide surface areas, 2D materials are employed as an addition to the interfacial layers.

By creating unique 2D tellurophene-based MOFs and exfoliating them using branched poly(ethylenimine)ethoxylate (PEIE) to create single- or few-layer MOF nanosheets, Xing et al.[72] have presented an efficient peeling technique for MOFs. Using MOF nanosheets functionalized with PEIE as an interlayer, they were also able to improve the PCE of OSCs. According to the findings, a hybrid EEL with this kind of conductivity may outperform pristine PEIE and adjust the ETL's work function to reduce charge recombination in the resulting device. This would allow for a 15% increase in PCE when compared to the control device, as seen in Fig. 4C.[72] Another advancement was the publication of Sasitharan et al.[79] on

production of ultrathin zinc porphyrin-based MOF nanosheets (MONs).

A PCE of 5.2% was demonstrated by the OSCs using MONs as the photoactive layer, which is nearly twice as much as the reference device. Because of their structural, optical, and electrical characteristics, MONs provided a surface template for poly(3-hexylthiophene-2,5-diyl) (P$_3$HT) crystallization. Therefore, enhanced PCEs were obtained by lowering the grain size, increasing the hole mobility and raising the absorbance twice. These findings highlight the possibility of using tunable 2D MOF nanosheets as building blocks to raise the efficiency of various OSCs.

2.2.3 Perovskite solar cells (PSCs) with MOFs. Materials with particular crystal structures that exhibit photovoltaic (electricity from light) properties are known as perovskites. Due to their exceptional efficiency and low manufacturing costs, these materials have the potential to completely transform the solar industry. With efficiency rising quickly from reports of roughly 3% in 2009 to over 25% today, perovskite solar cells have made impressive strides in recent years.[80] Perovskites have the general structural formula ABX_3, where the X site is a halide (I$^-$, Br$^-$, Cl$^-$, or their mixtures; SCN$^-$), the B site is a divalent metal (Pb^2, Sn^{2+}, Bi^{2+}, Ge^{2+}), and the A site is an organic or inorganic cation (Cs$^+$, Rb$^+$, methylammonium Cs$^+$, Rb$^+$, methylammonium (MA) CH$_3$NH$_3$, formamidinium (FA); CH$_2$(NH$_2$)$_2^+$, guanidinium). Perovskite materials have several notable optoelectronic characteristics, including the capacity to transport ambipolar charges, strong and broad light absorption, extended exciting diffusion length, low cost, and solution processability. Relevant research projects are emerging because PSCs show promise for challenging the current inorganic-based photovoltaic approaches.[81,82] Despite the rapid rise in efficiency of perovskite solar cells (Fig. 5A), several obstacles need to be overcome before this technology can be competitively adopted in the commercial sector. The produced perovskite film typically has many flaws and grain boundaries because of the polycrystalline nature restricted by the solution-based fabrication procedures, which will compromise the stability of the devices' performance. Therefore, when exposed to moisture, oxygen, heat, and light, PSCs are susceptible to degradation.[83,84]

Perovskites provide excellent light-absorbing properties such as minimal recombination losses, easy bandgap tunability, long charge carrier diffusion lengths, and inexpensive manufacturing. An electron transport layer (ETL), a hole transport layer (HTL), a light absorber (a perovskite layer), a conductive substrate (either indium tin oxide (ITO) or fluorine-doped tin oxide (FTO)), and a metal electrode make up a PSC. As illustrated in (Fig. 5B), PSCs are mainly classified into mesoporous or planar structures, which are further subdivided into conventional (n–i–p) and inverted (p–i–n) structures.[85] Vinogradov et al.[87] reported the insertion of a Ti-based MOF in a standard n–i–p PSC by depositing MIL-125 onto the surface of TiO_2 nanoproducts *via* a single-step hydrothermal synthesis. Their research verified that micro-mesoporous MOFs can strengthen the interfacial contact between the perovskite films
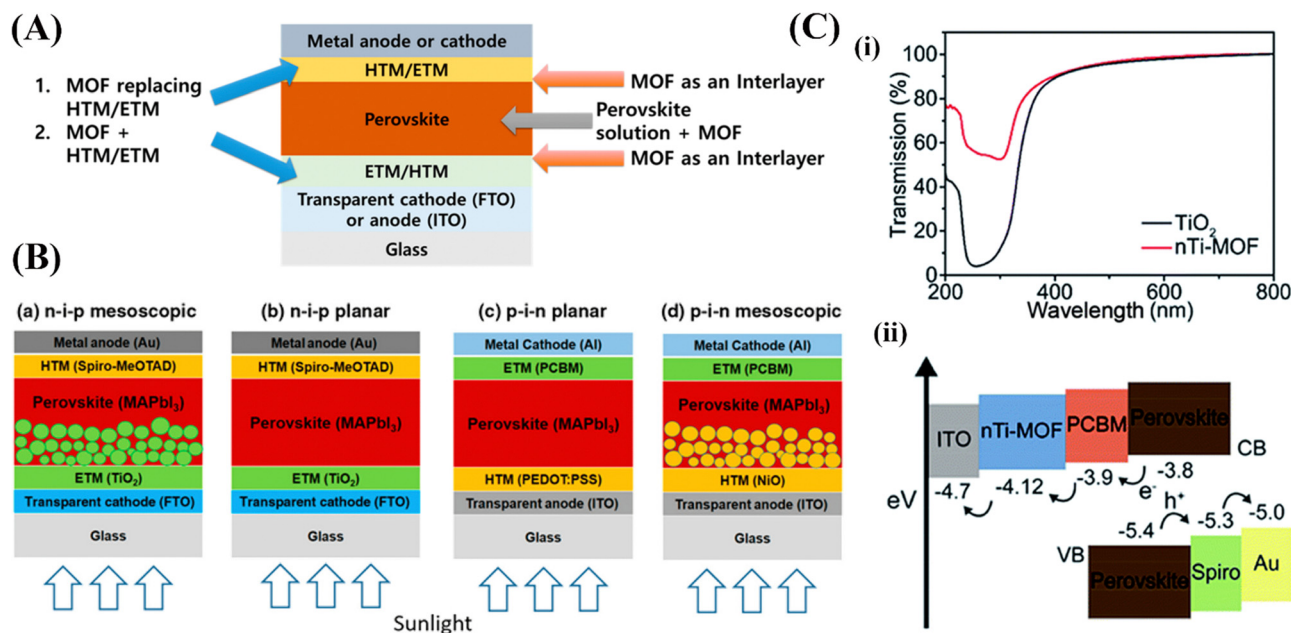
Fig. 5 (A) Schematic of where MOFs can be used in perovskite solar cells (PSCs), (B) schematic of perovskite solar cells with (a) n−i−p mesoscopic, (b) n−i−p planar, (c) p−i−n planar, and (d) p−i−n mesoscopic structures,[85] and (C) (a) the transmission of TiO_2 and nTi-MOF. (b) The energy level diagram.[86]

and promote perovskite crystallization, thereby suppressing interfacial charge recombination and improving device stability and performance. In comparison to the n−i−p structure, the p−i−n structure lowers the process temperature, which is advantageous; nevertheless, the somewhat lower efficiencies are a drawback. Moreover, Lee et al.[88] added insulating porous Zr-MOFs, MOF-808 and UiO-66 at the NiO_x/perovskite interface to give the perovskite materials another scaffold to develop on. These implanted MOFs support the crystallinity of the perovskite film formed on top, much like the advantages of the microporous scaffold that were previously discussed (Fig. 5C).

Li et al.[89] have doped an indium-based MOF, in addition to employing a MOF in the ETL, $[In_2(phen)_3Cl_6]\cdot CH_3CN\cdot 2H_2O$ (In_2), into the HTL of spiro-OMeTAD. The authors first showed that a device can provide more photo-response by including In_2 in the HTL. Furthermore, In_2 has a strong UV absorption due to its large E_g, even though its emission was in the visible light spectrum. In a subsequent evolution, the HTL's cube-shaped In_2 crystals might serve as the light-scattering center, generating many reflections that lengthen the light path inside the apparatus. This adds to the increase in absorption in the 500–700 nm range. With the use of rapid heat transfer, Ryu et al.[86] carried out a thorough investigation to create nanocrystalline Ti-based MOF (nTi-MOF) NPs on ITO glass. This resulted in the successful production of an nTi-MOF as opposed to a Ti-MOF (MIL-125). Their overall electrical structures differed slightly, despite the fact that the chemical state of Ti in an nTi-MOF is comparable to Ti in TiO_2. Because of its larger current energy level, an nTi-MOF has a greater transmittance than TiO_2. Its ability to function as an ETL in a device is indicated by the fact that its energy level, as demonstrated, agrees well with that of the perovskite and ITO. Rather than altering the mesoporous

TiO_2 scaffold, Shen et al.[90] inserted a type of insulating ZIF-8 on top of the mesoporous TiO_2 (mp-TiO_2) layer. ZIF-8 was added to the mp-TiO_2 layer, roughening its surface in a way that encourages the crystallinity of the perovskite layer formed on top, similar to the effects reported in other investigations.

2.3 MOFs for batteries

Through an electrochemical process known as oxidation–reduction (redox), a battery directly transforms the chemical energy found in its active components into electric energy. For the purpose of powering electric vehicles, portable gadgets, grid energy storage, and renewable energy devices, in particular, dependable and efficient energy storage devices are key components of the sustainable use of renewable energy sources.[91] The electrode materials are a crucial determinant of the rechargeable battery's performance. Consequently, a number of investigations have been carried out to create sophisticated electrode materials that have outstanding cycling stability, a high specific capacity, and good rate performance. Due to their unique structural and electronic properties, MOFs a novel class of porous crystalline coordination polymers have garnered significant attention in the field of batteries in recent decades. These features make them useful for investigating advanced batteries, such as zinc ion batteries (ZIBs), lithium-ion batteries (LIBs), lithium–sulfur batteries (Li–S), lithium–oxygen batteries (Li–O_2), sodium-ion batteries (SIBs), and sodium iodine (Na–I_2) batteries.[92–94] Consequently, MOF-based materials show promise as electrode materials for the upcoming generation of long-cycle, high-capacity rechargeable batteries.

2.3.1 Lithium-ion batteries (LIBs).
Lithium-ion batteries (LIBs) are the most significant and widely utilized energy storage technology in our daily lives; they are vital components

of computers, electrical cars, and portable electronics. One of the main factors affecting LIBs' overall performance is the electrode material. Therefore, the creation and manufacturing of novel materials or materials with distinctive architectures, like LIB electrodes, have received enormous attention. Still, they are unable to fulfill today's greater energy and power demands despite their extended lifespan and simplicity of integration into portable devices.[44] Aside from graphite, which is the material used in commercial negative electrodes, a number of nanostructured materials, including carbon nanotubes, graphene composites, transition metal oxides, *etc.*, have been thoroughly studied recently for potential use in LIBs. The low capacity and energy density of graphite is the driving force behind the search for other suitable materials. Due to their large surface area and persistent porosity for Li$^+$ ion storage and migration during charge and discharge processes, pristine MOFs have been used as replacements to traditional graphite anode materials. The MOF IN LIBs comprise the following: (1) rapid charging rates are caused by the rapid electron transport to the redox-active sites, which is facilitated by the high electrical conductivity of 2D c-MOFs.[95] (2) Li ions and other anions are made easier to diffuse and inject by the regular channels of 2D c-MOFs. (3) Stiff and elongated structures ensure superior stability during Li insertion/extraction, ensuring electrodes' electrochemical longevity.[96] (4) To obtain a better specific capacity and enough energy density, both organic linkers and transition metal ions can function as the redox active sites.[97]

A conductive bis(diimino)nickel framework (Ni-HITP) is used as a high-capacity LIB cathode material.[98] The distinct energy storage mechanism that both the cation (Li$^+$) and anion (PF$_6^-$) provided as electron carriers to charge and discharge electrochemical energy was made clear by their discovery. Furthermore, due to the charge distribution between the metal ions and non-innocent ligands, Ni-HITP possesses several redox states. Thanks to its unique redox nature and satisfactory electronic conductivity, Ni-HITP demonstrated a faradaic reaction-driven energy storage function that demonstrated stable cycling performance for up to 300 cycles, an exciting specific capacity of 155 mA h g^{-1}, and a high specific energy density of 434 W h kg^{-1} at a current density of 10 mA g^{-1}. A redox-active 2D copper benzoquinoid MOF (Cu-THQ) was created by Jiang *et al.*[99] as the cathode for rechargeable lithium-ion batteries. According to their findings, plentiful porosity and intrinsic redox properties of Cu-THQ allowed for the achievement of a maximum capacity and specific energy density of 387 mA h g^{-1} and 775 W h kg^{-1}, respectively. In a manner similar to Ni-HITP, there, Li$^+$ and PF-6 were both embedded in the pores of 2D Cu-THQ frameworks as part of the energy storage process. Moreover, research on a variety of morphologies, including hollow microspherical, pillar-layer, lamellar, and shell-like morphologies, was reported in ref. 100 and 101. Their work is helpful for accommodating volume variation, electrolyte penetration, and lithium-ion transportation during the charge/discharge processes. The study conducted by Zou *et al.*[102] on a multipodal composite of NiO/Ni/graphene derived from MOFs

in the form of a hierarchical hollow ball-in-ball nanostructure showed that the material had a high reversible specific capacity of 1144 mA h g^{-1} and good cyclability, with nearly 100% capacity retention after 1000 cycles. Specifically, a NiO/Ni/graphene electrode has been used to create a sodium-ion battery that exhibits exceptional rate capability and great cyclability at a current density of 2 A g^{-1}, with a capacity of 207 mA h g^{-1}.

Qi *et al.*[103] conducted a thorough investigation that demonstrates how ZrO$_2$ produced from UiO-66 effectively acted as a protective layer to enhance the rate capability of the LiCoO$_2$ cathode material. After 100 cycles, the resulting ZrO$_2$@LiCoO$_2$ hybrid cathode produced a reversible capacity of 148 mA h g^{-1} at a high current density of 2325 mA h g^{-1}. By contrast, the capacity of pure LiCoO$_2$ dropped quickly to 20 mA h g^{-1}. It is noteworthy that after 100 cycles at 55 °C, the hybrid cathode also showed a reversible capacity of 132 mA h g^{-1}, indicating remarkable thermal stability. The improved structural stability resulting from the ZrO$_2$ coating, which successfully reduced the volume change of LiCoO$_2$, may be responsible for the hybrid cathode's increased performance. Recently, Ziebel *et al.*[95] reported the design of two iron semiquinoid frameworks based on a deprotonated 2,5-dichloro-3,6-dihydroxybenzoquinone (Cl$_2$dhbqn$^-$) ligand, namely (H$_2$NMe$_2$)$_2$Fe$_2$(Cl$_2$dhbq)$_3$ (MOF 1) and (H$_2$NMe$_2$)$_4$Fe$_3$-(Cl$_2$dhbq)$_3$(SO$_4$)$_2$ (MOF 2). Their findings showed a notable difference in electrical conductivity of 2.6 × 10^{-3} for MOF 1 and 8.4 × 10^{-5} S cm^{-1} for MOF 2, respectively. MOF 2 demonstrated a rapid capacitance degradation with larger charging rates, along with a reasonable discharge capacity of 165 mA h g^{-1} (90% of the theoretical value) in 0.1 m LiBF$_4$ propylene carbonate electrolyte at a modest charging rate of 10 mA g^{-1}. On the other hand, MOF 1 retained a comparatively high capacity of 141 mA h g^{-1} (72% retention) even at a charging rate of up to 150 mA g^{-1}, nearly 100% of its theoretical capacity of 195 mA h g^{-1} at 20 mA g^{-1}. Meanwhile, MOF 1 achieved a coulombic efficiency higher than 100% and a benchmark-specific energy density of 533 W h kg^{-1} at 20 mA g^{-1}.

Yang *et al.*[104] developed porous ZnCo$_2$O$_4$ by carefully calcining Zn-doped MOF-74 at 400 °C. The substantial synergistic impact between Zn and Co has resulted in improved specific capacity, cycling stability, and rate capability of the developed porous nanostructured ZnCo$_2$O$_4$ when compared to Co$_3$O$_4$. It was discovered that adding a doping step to the MOF synthesis could result in metal/metal oxide complexes with improved characteristics during the pyrolysis process.

They created Co-MOFs using various organic linkers (1,4,5,8-naphthalene tetracarboxylic dianhydride (NTCDA) and perylene-3,4,9,10-tetracarboxylic dianhydride (PTCDA)) after realizing that Co$_3$O$_4$ had limited cycling stability and rate capability. They then treated the Co-MOFs with an organic amine solution before using calcination as a novel method to overcome these limitations, as reported by Su *et al.*[105] The material that was developed demonstrated an improved capacity for lithium storage (1370 mA h g^{-1} reversible capacity at a mass normalized current of 100 mA g^{-1}) and this demonstrated
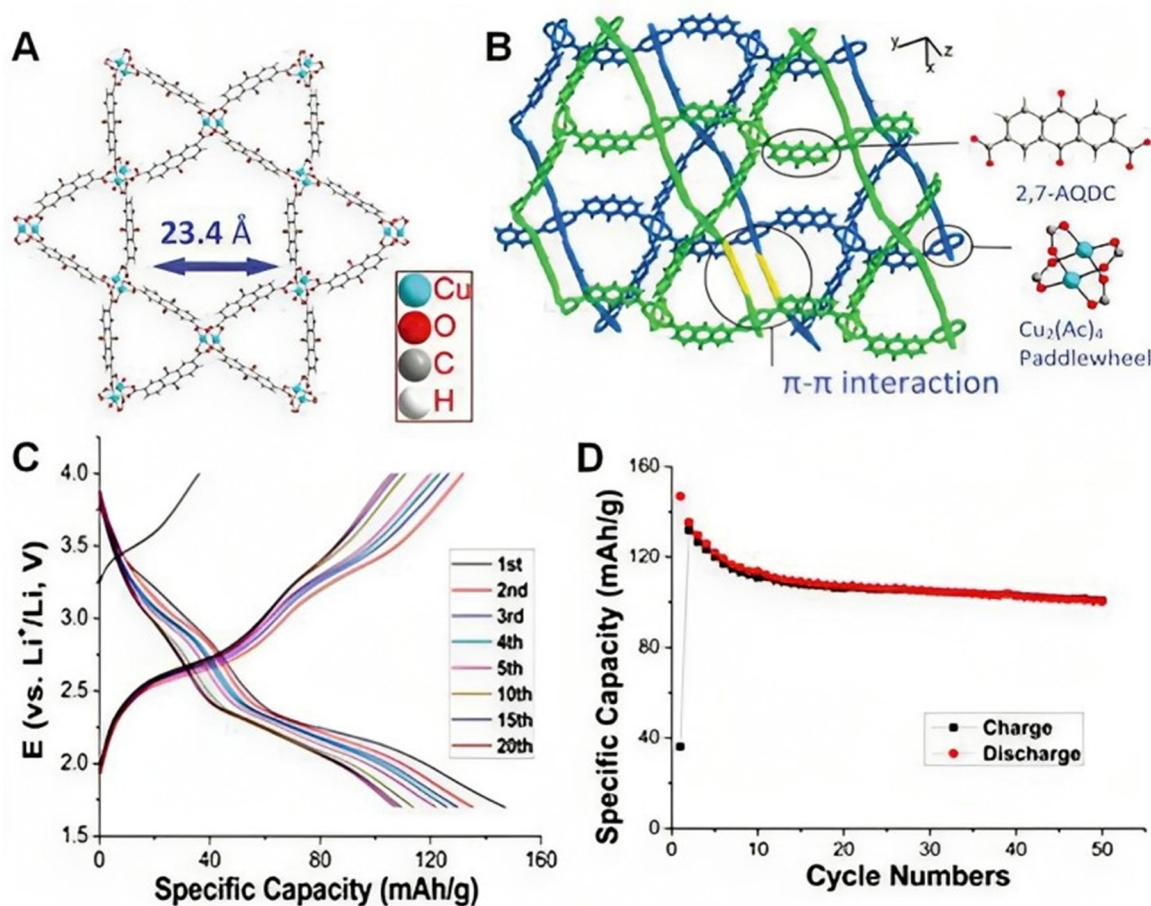
Fig. 6 Structure and performances of Cu(2,7-AQDC) in a battery. (A) The single Kagome layer of Cu(2,7-AQDC). (B) The indication picture of the glided adjacent layers. (C) Charge−discharge profiles of the 10 wt% MOF battery. (D) Cycle performances of the battery for 50 cycles. Reproduced with permission.[97]

that the synthesis process was possible for the fabrication and manipulation of metal oxides/morphology. In addition, depositing metal oxides on electro-conductive substrates can enhance Co$_3$O$_4$'s electrical conductivity. Hu *et al.*[106] carried out an experiment using pyrolyzed Se-doped ZIF-67 to produce CoSe nanoparticles enclosed in a hollow carbon shell. The as-synthesised CoSe@C demonstrated outstanding cyclability by maintaining 91.6% discharge capacity, benefiting from the structural protection and charge transport channels supplied by the hollow carbon matrix. In order to increase the theoretical capacity, Zhang *et al.*[97] used a newly developed MOF of Cu(2,7-AQDC) (2,7-H$_2$AQDC = 2,7-anthraquinonedicarboxylate), which has separate redox activities at both Cu$_2$(Ac)$_4$ nodes and anthraquinone ligands. This resulted in a high initial capacity (147 mA h g^{-1}) (Fig. 6). Regrettably, there was a small capacity decrease ($\approx$42 mA h g^{-1}) following a reversible capacity of $\sim$105 mA h g^{-1} in 50 cycles. The electroactive MOF cathodes were also built using quinone-type ligands as well as a few additional ligands, such as 1,2,4,5-tetraaminobenzene,[107] tetrathiafulvalene tetracarboxylic acid,[108] and tricarboxytriphenyl amine.[109] Guo *et al.*[110] used a Cu–Ni bimetallic MOF as the precursor to create a binary metal oxide hybrid microsphere

with multiple shells (CuO@NiO). Due to its distinct structure and molecular makeup, the CuO@NiO hybrid microsphere demonstrated a reversible capacity of 1000 mA h g^{-1} following 200 cycles, surpassing the theoretical capacities of CuO (674 mA h g^{-1}) and NiO (718 mA h g^{-1}). In order to achieve electrochemical Li storage, Ferey *et al.*[111] studied the usage of the MIL-53(Fe) cathode material to exploit mixed-valence states of metals during discharge and charge. Due to the low density of the material and the restricted amount of Li ions introduced, the cathode exhibits a gravimetric capacity of 75 mA h g^{-1} and a volumetric capacity of 140 mA h L^{-1}. MOFs have been employed as precursors for the synthesis of metal oxides, transition metal oxides, metal/metal oxides, and metal oxides/carbon composites for LIB negative electrode materials in addition to carbon materials. Yang *et al.*[112] reported the production of porous carbon-coated ZnO quantum dots by the controlled pyrolysis of Zn$_4$O-MOF-5. With a mass-normalised current of 75 mA g^{-1}, the as-synthesised material demonstrated a high reversible capacity of 1200 mA h g^{-1}.

2.3.2 Lithium–sulfur batteries (Li–S). Lithium–sulfur (Li–S) batteries are thought to be the most significant technologies for the upcoming generation of electrochemical energy storage.
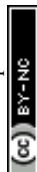
Li–S batteries have the potential to produce high energy densities of up to 2600 W h kg^{-1} and specific capacities of up to 1670 mA h g^{-1}.[113] Their high energy density and lightweight design have drawn more and more attention in recent years. Li–S batteries exhibit additional benefits over lithium-ion batteries (LIBs), including reduced fabrication costs, environmental friendliness, and widespread availability of the electrode-active sulfur material. These benefits offset some of the apparent benefits of sulfur, such as low cost, large natural abundance, and non-toxicity. Additionally, Li–S batteries outperform the existing LIBs in terms of economic viability.[114] On the other hand, before Li–S batteries are widely used in electronic products and hybrid cars, there are a few issues that need to be resolved. The well-known "shuttle effect", which results from the dissolution of intermediate products (i.e., polysulfides) in the organic electrolyte and causes electrode deactivation and poor cycling performance, leads to the following challenges, including low electrode utilization, poor high-rate performance, and rapid capacity fade. To address these problems, a Ni-MOF, $\{\{Ni_6(BTB)_4(BP)_3\}\}_n$ (BTB = benzene-1,3,5-tribenzoate and BP = 4,40-bipyridyl), was chosen to confine sulfur.[115] The typical charge and discharge behaviors of the Ni-MOF/S electrode mentioned above were revealed by galvanostatic charge and discharge tests. After 100 cycles, the Ni-MOF/S composite has a high-capacity retention of 89% at a current density of 0.1C (168 mA g^{-1}). The dissolution and shuttle effects of polysulfides are inhibited by the hierarchical porous structure of the Ni-MOF and the strong contacts between Ni metals and polysulfides. The goal of this study is to improve the cyclability of Li–S batteries by designing Li–S electrodes that include sulfur within the pores of mesoporous MOFs.

However, limited sulfur consumption and a lower performance rate are caused by MOFs' insulating characteristics. An ionic sieve called the HKUST-1@GO separator functions as a buffer against shuttling in Li–S batteries by selectively allowing Li$^+$ ion transport while inhibiting polysulfide migration. The HKUST-1@GO hybrid Li–S battery, used as an ionic sieve membrane for Li–S batteries, was reported by Bai et al.[116] to have low capacity-fading rates of roughly 0.019% per cycle across 1500 cycles. Furthermore, Baumann et al.[117] have demonstrated how to optimize the size of nanocrystals in HKUST-1. This is because the surface of the particle, which has exposed Cu sites, increases the number of sulfur binding sites on the external surface, reducing the particle size and improving the capture of escaping polysulfides from the pores, reducing their diffusion toward the anode. Higher sulfur loading with larger nanocrystals, as illustrated in (Fig. 7), is nevertheless not advantageous to battery performance in this scenario, despite the presence of capture sites on the surface. Through cooperation, these elements can get past the inherent mechanical brittleness and create a strong ionic sieve membrane that effectively suppresses the shuttle effect. With the MOF@GO hybrid-based separator, a low capacity decay rate over 1500 cycles is guaranteed in a Li–S battery with the cathode comprising a sulfur-functionalized mesoporous carbon material (around 70% sulfur content). The HKUST-1 modified separator did not degrade after cycling, according to He et al.[118] They reasoned that since almost all of the Cu sites were occupied by oxygen groups, the quantity of Cu–S forms
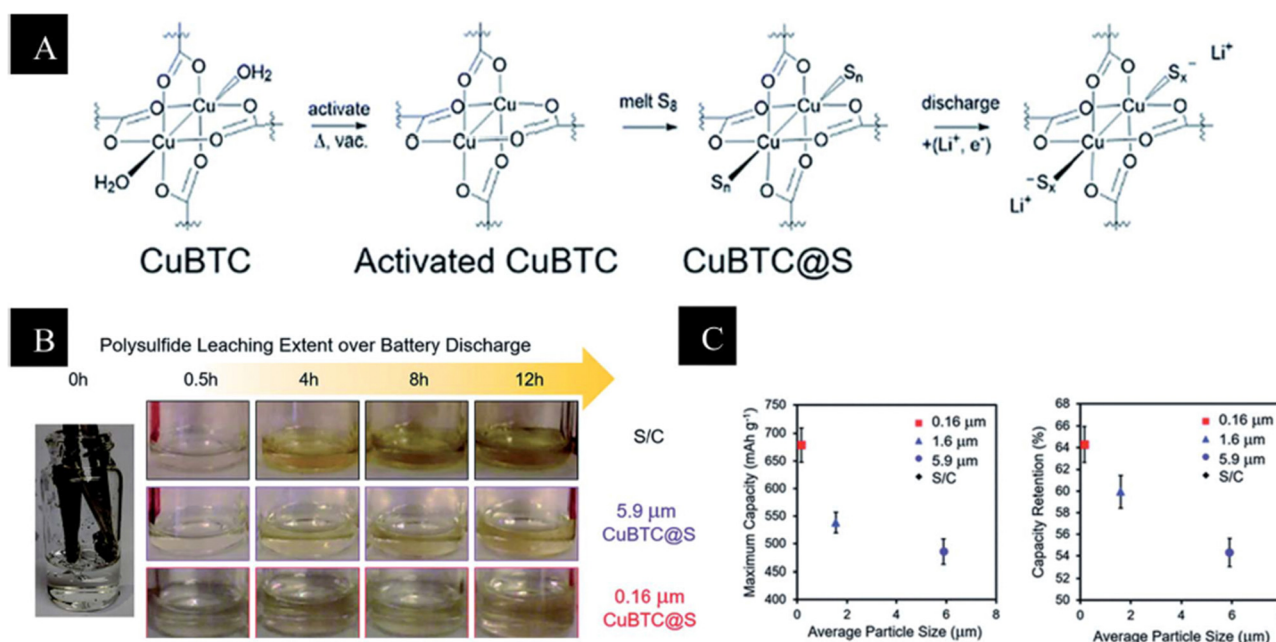

Fig. 7 (A) Activation and sulfur loading of HKUST-1 with potential binding sites at the Cu paddlewheel. (B) Electrolyte samples of 0.16 mm and 5.9 mm CuBTC, and S/C electrodes during a galvanostatic discharge of C/20. Yellow discoloration indicates the amount of leached polysulfide. (C) Coin cell performance of 3 cells as a function of particle size, left: the average maximum capacity and right: the average capacity retention over 20 cycles.[117]

would be limited. Li et al.[119] disclosed the capacity reduction resulting from irreversible Cu–S interactions in an additional HKUST-1 modified separator. Liu et al.[120] produced a 3D monolith by inserting 20–100 nm HKUST-1 agglomerates or 200–400 nm ZIF-67 nanoparticles in a conductive polymer hydrogel. The polymer hydrogel was able to permeate both kinds of nanodomains, and their research showed that the MOFs' aperture openings ultimately determined the performance. Compared to ZIF-67, which has a tiny pore opening of 0.34 nm, HKUST-1, with its large pore opening of 0.90 nm, was more suited to encapsulate S8 (0.64 nm) and contain long chain polysulfides (> 0.4 nm).

Xu et al.[121] conducted an experiment, which demonstrated the synthesis of sulfur-encapsulated hierarchically porous carbon nanoplates (HPCN) by one-step pyrolysis of MOF-5. The nanoplates had a huge pore volume of 1.18 cm^3 g^{-1}, a high specific surface area of 1645 m^2 g^{-1}, and an average thickness of about 50 nm. High specific capacity and superior cycle performance are exhibited by sulfur contained in HPCN. With a reversible capacity of 730 mA h g^{-1}, the hybrid cathode demonstrated exceptional cycling performance after 50 cycles at a current of 0.5C, with charging and discharging at 837.5 mA h g^{-1}. MOFs themselves, with their highly organized pores and tunable porosity, can be used as ionic sieves in membrane separators to lessen the shuttling impact of polysulfides, in addition to the MOF-derived materials that are employed as the sulfur hosts. Wu et al.[122] reported that the sulfur concentration in the hybrid and the type of electrolyte have an impact on the performance of MOF-derived carbon–sulfur hybrid cathodes in Li–S batteries. Furthermore, Liu et al.[123] constructed lithium–selenium (Li–Se) batteries using porous carbon spheres generated from a MOF. It is noteworthy that at ambient temperature, Se has a substantially higher electrical conductivity than S (1 × 10^{-5} vs. 5 × 10^{-30} S cm^{-1}), which may accelerate the cathode material's rate of electron transportation. Cerium(IV) UiO-66 (Ce-MOF-1) and MOF-808 (Ce-MOF-2) nanoparticles (∼180 nm) produced on carbon nanotubes (CNT) were used in a study conducted by Hong et al.[124] to explore the possibility of open-metal-site catalysis of long-chain polysulfide conversion. A high sulfur loading of 6.0 mg cm^2 and an initial specific capacity of 993.5 mA h g^{-1} at 0.1C were achieved by the MOF-808-based hybrid, which consumed Li_2S_6 considerably better than the CNT or UiO-66-based hybrid, which had no unsaturated coordination sites at the Ce(IV) nodes.

Wu et al.[125] have reported the development of MOF-derived microporous carbon polyhedron (MCP) encapsulated PAN nanofibers as an effective sulfur immobilizer for Li–S batteries. This is because sulfur can be uniformly dispersed inside the nanofibers and in the micropores of MCPs. A combination of MCPs and PAN was electrospun to achieve the encapsulation procedure, which was then achieved by loading sulfur through a two-step reaction at 155 °C and 300 °C, respectively. The enhanced S/MCPs–PAN composite, which had 52 wt% sulfur, had a large reversible capacity of about 790 mA h g^{-1} at first, which only slightly decreased to 789.7 mA h g^{-1} in the second cycle. After 200 cycles, the discharge capacity remained at

666.2 mA h g^{-1}, demonstrating both good capacity retention (84.4%) and high sulfur utilization (90.7%). According to Zhou et al.,[126] the particle size reduces with increasing sulfur utilization in a series of nanoscale ZIF-8 frameworks, with less than 20 nm providing a capacity of over 950 mA h g^{-1} at 0.5C. However, the best size for cycling stability (75% over 250 cycles at 0.5C) was ∼200 nm.

Furthermore, Hong et al.[127] found that 100 nm-sized nanoparticles outperformed 200 nm-, 500 nm-, and 1 mm-sized particles for a Cu-MOF that used both ligand Lewis acid sites and node Cu sites for polysulfide interaction. Electrochemical reactions only take place on the particle surface, where electrons and Li ions are accessible due to the conductivity constraints of the MOFs in both scenarios.

2.3.3 Sodium-ion batteries (SIB). Even though Li-ion batteries are the industry leaders in the energy market for portable electronics, they still have a lot of drawbacks, including low power density, safety concerns, and a lack of lithium resources in the Earth's crust. In addition, the price of Li-ion batteries is very high due to the limited availability of lithium (20 ppm) on Earth.[128] Furthermore, as noted by Hwang et al.,[129] large-scale electrochemical energy storage systems (EESs) may also be hampered by LIBs' low power density and lack of safety. Nevertheless, because of their lower energy density, short lifespan, and higher ionic properties to many electrode materials that are appropriate for LIBs, SIBs are no longer able to meet their needs.[130] Due to these constraints, researchers looked for appropriate electrodes for sodium-ion batteries (SIBs) that exhibit electrochemical behavior similar to that of lithium-ion batteries (LIBs). These electrodes were thought to be a viable substitute for LIBs because of the low electrochemical cell potential (−2.71 V vs. SHE) and abundance of sodium.[131]

While a number of materials, including Prussian blue,[132] transition metal oxides,[128] and small organic molecules,[133] have been extensively employed as cathode materials for SIBs, it is still difficult to find promising anode materials with a long cycle life, high capacity, and high energy density. In this regard, MOF-derived nanostructures offer a chance to develop SIB anodes with superior electrochemical performance in a sustainable manner. For instance, numerous published studies on $Na_{1.40}MnFe(CN)_6 Na_{1.72}$ MnFe(CN)₆ and KMFe(CN)₆ (M = Mn/Fe/Co/Ni/Cu/Zn) have demonstrated that the insertion and extraction of Na^+ would cause a reversible reduction or oxidation of the metal ions.[134] Zhang et al.[135] developed a hollow porous CuO/Cu_2O octahedron and evaluated it as an anode for SIBs using a different alternative Cu-BTC MOF as a template. The results of the studies showed that calcination temperature was critical to the CuO/Cu_2O composite's electrochemical performance, and the optimized CuO/Cu_2O-300 had good rate capability, high capacity retention, and a long lifespan. A study conducted by Yue et al.[136] used the pore size and PBA shape to determine the rate capability in SIBs. The analysis of the $KNiFe(CN)_6/t$ series (t = 2, 18, and 72 h) revealed that the presence of big pores would make sodium ion transport significantly easier.
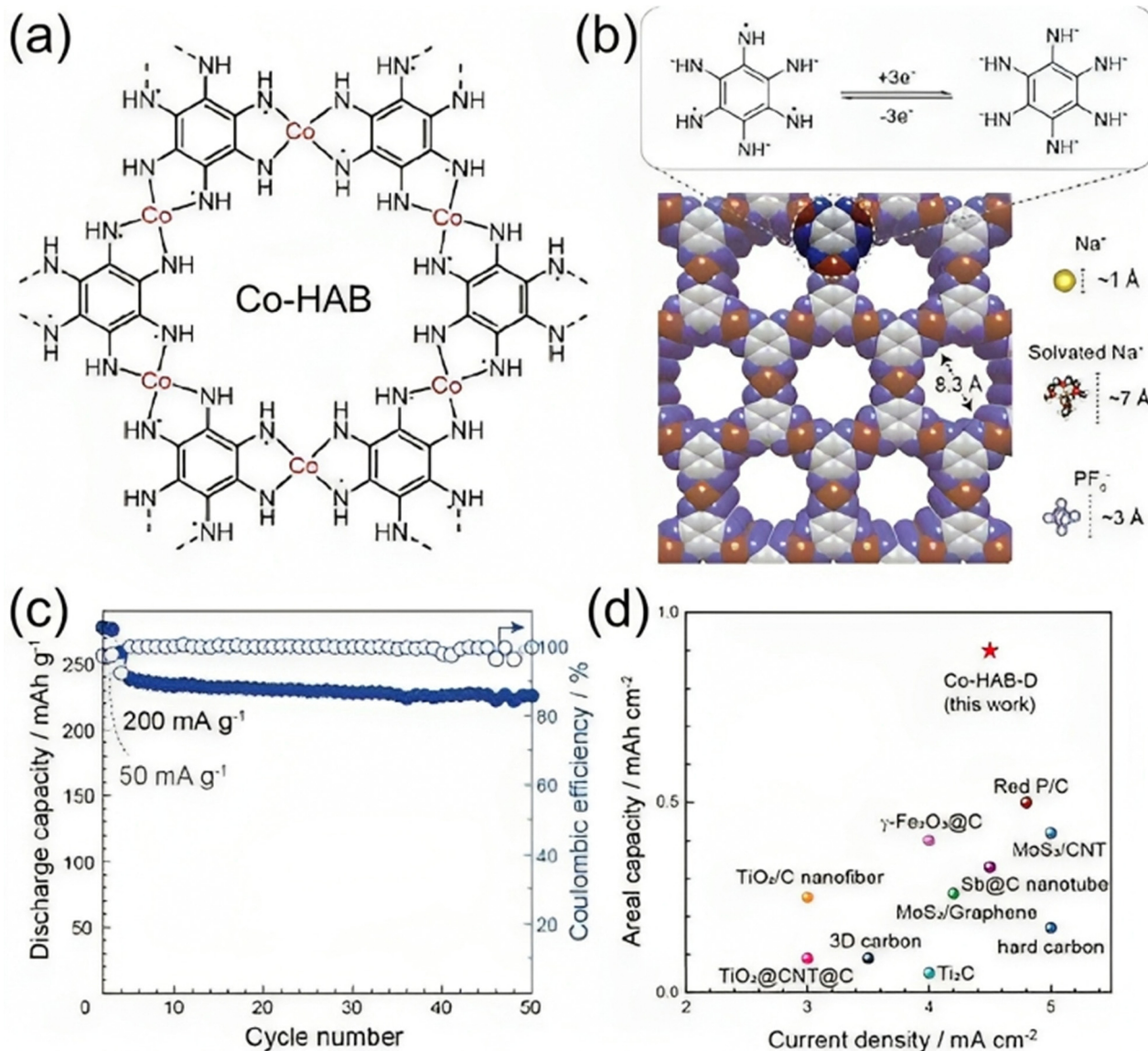
Fig. 8 Electrochemical performance of the Co–HAB electrode for SIBs. (a) Chemical structure of Co–HAB. (b) A space-filling diagram of Co–HAB and the size comparison of the pore with Na⁺, solvated Na⁺ and PF₆⁻ions. Top: proposed three-electron reversible reaction of the HAB ligand in Co–HAB. (c) Cycling stability test of the Co–HAB electrode. (d) Comparison of areal capacity of Co–HAB with representative reported anode materials for SIBs.[137]

Park et al.[137] reported the integration of a 2D c-MOF of Co–HAB (hexaaminobenzene) into high-power SIBs (Fig. 8(a) and (b)). HAB is a good candidate for primary design concepts for high-performance electrode materials since it can theoretically undergo a redox reaction involving up to six electrons and has the largest concentrations of redox centers. Co–HAB electrodes provided a specific capacity of 291 mA h g^{-1} at 50 mA g^{-1} and continued to maintain a capacity of 226 mA h g^{-1} at a higher current density of 500 mA g^{-1} after over 50 cycles with a coulombic efficiency of nearly 100% (Fig. 8(c) and (d)). Zhang et al.[138] reported the production of a porous CoFe$_2$O$_4$ nanocube from the CoFe-PBA (Prussian blue) precursor. For a current density of 50 mA g^{-1}, the sample showed a capacity of 394 mA h g^{-1} and a capacity retention of 91.4%. Upon 500 cycles, a maximum capacity of 152.6 mA h g^{-1} was retained,

despite the high current density of 2.5 A g^{-1}. In order to create MnFe$_2$O$_4$ hollow microboxes, Guo et al.[139] additionally utilized MgFe-PBA as a precursor. Examined as an anode for SIBs, the as-prepared MnFe$_2$O$_4$ demonstrated good rate capability and cycle stability. With a theoretical specific capacity of 312 mA h g^{-1}, the Co–HAB was able to store three electrons per HAB unit in addition to three sodium ions, indicating that the redox-active sites of the HAB had been nearly fully used. Furthermore, Kaneti et al.[140] reported the synthesis of a Ni-doped Co/CoO/N-doped carbon (NC) hybrid employing bimetallic Ni-Co-ZIF as the precursor. The resulting Ni-doped Co/CoO/NC hybrid is very porous and has a specific surface area of 552 m^2 g^{-1}. As an electrode for SIBs, this hybrid may provide a discharge capacity of 218 mA h g^{-1} at a high current density of 500 mA g^{-1} while maintaining strong cycle stability and great rate performance.

Another breakthrough by Zou et al.[141] employed MOF-5($Zn_4O(OOCC_6H_4COO)_3$) as a precursor to create porous carbon in the form of a cube. The porous carbon that was obtained demonstrated excellent overall electrochemical performance when used as a SIB anode. A high current density of 3.2 A g^{-1} was maintained for 5000 cycles, and a capacity of 100 mA h g^{-1} was achieved after 100 cycles at a current density of 100 mA g^{-1}. Furthermore, MOF-derived materials such as Co_3O_4@nitrogen-doped carbon, CoP@C, CoSe/C, and TiO_2@C have benefited from the integration of metal compound components with carbons and have functioned as efficient anode materials for the SIBs.[142,143] Considering the aforementioned factors, MOFs and their derivatives are suitable electrode materials for high-power SIBs that show great promise and possess exceptional cycle stability and ultrafast storage capability.

2.3.4 Lithium–oxygen batteries. As one of the most researched types of metal–air batteries, the Li–O_2 battery is made up of Li metal as the negative electrode, i.e. the anode, reduced oxygen as the cathode active mass, and an electrolyte solution containing Li$^+$. The devices are made up of a cathode, which is a composite porous matrix with electronic conductivity that allows oxygen gas and Li ions in the electrolyte solution phase to interact electrochemically. As schematically shown in Fig. 9A, it primarily operates with the deposition/dissolution of lithium metal at the anode and an oxygen reduction reaction (ORR)/oxygen evolution reaction (OER) at the cathode.[144] As opposed to Li–ion and Li–S batteries, which store just anode active material, the porous cathode of Li–ion batteries leverages atmospheric oxygen to produce a high energy density. Anode Li yields a high specific capacity of 3842 mA h g^{-1} and a specific energy of 40.1 MJ kg^{-1}, which is comparable to gasoline (46.8 MJ kg^{-1}). Even at a less capacity, a robust Li–O_2 battery can supply enough power for automobiles or grid backup systems based on solar energy storage. Investigations are presently being conducted on four distinct categories of Li–O_2 systems: aprotic, aqueous, hybrid, and solid-state batteries. Regarding the types of electrolytes involved, the four types differ from one another. Subsequently, the latter ascertains the particular electrochemical processes involved in energy retention and release. Tan et al.,[145] provided a schematic example of these four battery types in Fig. 9B. Poor cathode and electrolyte performances are the primary bottlenecks preventing Li–O_2 batteries from being commercially viable.

The first MOF-based Li–O_2 batteries were developed by Wu et al.[146] A number of MOFs were carefully chosen to correlate the relationship between the structure and performance, including MOF-5, HKUST-1, and M-MOF-74 (M = Mg, Mn, and Co). According to Wu et al.,[146] MOF-74's accessible metal sites may result in a significant oxygen enrichment of frameworks, facilitating the Li–O_2 reaction and enhancing the performance of MOF-74-based Li–O_2 batteries. Consequently, at room temperature under 1 atm (O_2), Mn-MOF-74@carbon-black exhibits the most notable discharge capacity of 9420 mA h g^{-1} among all cells, with an applied current density of 50 mA g^{-1} and operating voltages of 2.6–2.7 V. The enhanced stability and efficiency in the latter case should be attributed to the synergistic effects of the bimetallic sites, which employ the bimetallic MOF, MnCo-MOF-74, as the cathode. Mu et al.[147] designed a soluble MOF based on heme as an electrolyte additive for Li–O_2. The MOF was synthesized using a surfactant-assisted technique. Specifically, metal nodes function as structural building blocks, heme-like TCPP(Fe) ligands operate as catalytic active sites, and polyvinylpyrrolidone (PVP) is used as a surfactant to regulate the formation of MOF crystals. According to McCloskey et al.[148] paper on fundamental chemistry, the discharge product during the recharging of Li–O_2 electrolytes is comparatively more stable. This can be attributed to the ether solvents' increased cathodic stability and resistance to nucleophilic attack.

Another breakthrough was reported by Liu et al.[149] for a Li–O_2 cell based on super-concentrated salt/DMSO that showed exceptional stability and reversibility even with an exposed Li anode. Additionally, Yuan et al.[150] conducted an examination of the ORR and OER performances of 2D nanosheets. In comparison to the comparable 3D Mn-MOF, the 2D Mn-MOF nanosheets (5.30 nm thickness) showed greater round trip efficiency (66.7% vs. 63.2%), lower overpotential (1.34 V vs. 1.57 V at 200 mA h g^{-1}), and higher electrochemical activity (1.66 V vs. 1.57 V at 200 mA h g^{-1}). The increased catalytic performance of the Mn–O sites was facilitated by a higher percentage of unsaturated metal sites on the surface and the edges as well as better diffusion brought about by the nano-scale 2D structure. This resulted in initial discharge capacities of 9464 mA h g^{-1} and 1000 mA h g^{-1} after 200 cycles at 100 mA g^{-1}. Nonetheless, Liu et al.[149] found that even with an exposed Li anode, a super-concentrated salt/DMSO-based Li–O_2 cell demonstrated outstanding stability and reversibility. The superior performance of the super-concentrated solutions can be ascribed to the presence of solely TFSI-Li$^+$(DMSO)$_3$ complexes and the absence of free DMSO solvent molecules, as DMSO molecules are unstable to O_2-attack and corrosive to the Li metal anode.

Yan and colleagues examined the impact of decreasing crystal size of Co-MOF-74 rods with thicknesses of 1400 and 800 nm as well as nanofibers with a thickness of 20 nm.[151] The enhanced performance of the Co-MOF-74 nanofiber is ascribed to the shorter ion transfer diffusion lengths and easier accessibility of the active Co sites. The existence of more defect sites in the nanofiber MOF, on the other hand, may have been caused by the employment of a size modulator during synthesis, which would account for the almost 2.5-fold increase in the initial specific capacity. Read[152] reported the usage of ethers as electrolyte solvents. Utilizing DME (dimethoxyethane) and DOL (1,3-dioxolane), they reported a Li–O_2 cell with good stability and exceptional rate capability. These characteristics are ascribed to the low viscosity and high oxygen solubility, which promote oxygen transport in the Li–O_2 cell.

2.3.5 Zn-ion batteries (ZIBs). In society, rechargeable ZIBs are used for a variety of purposes. Zn-based batteries come in various varieties. According to Mao et al.,[153] Zn–air batteries (ZABs) and Zn-ion batteries (ZIBs) are further subdivided into Ni–Zn batteries (NZBs) and Zn–Mn batteries (ZMBs). The
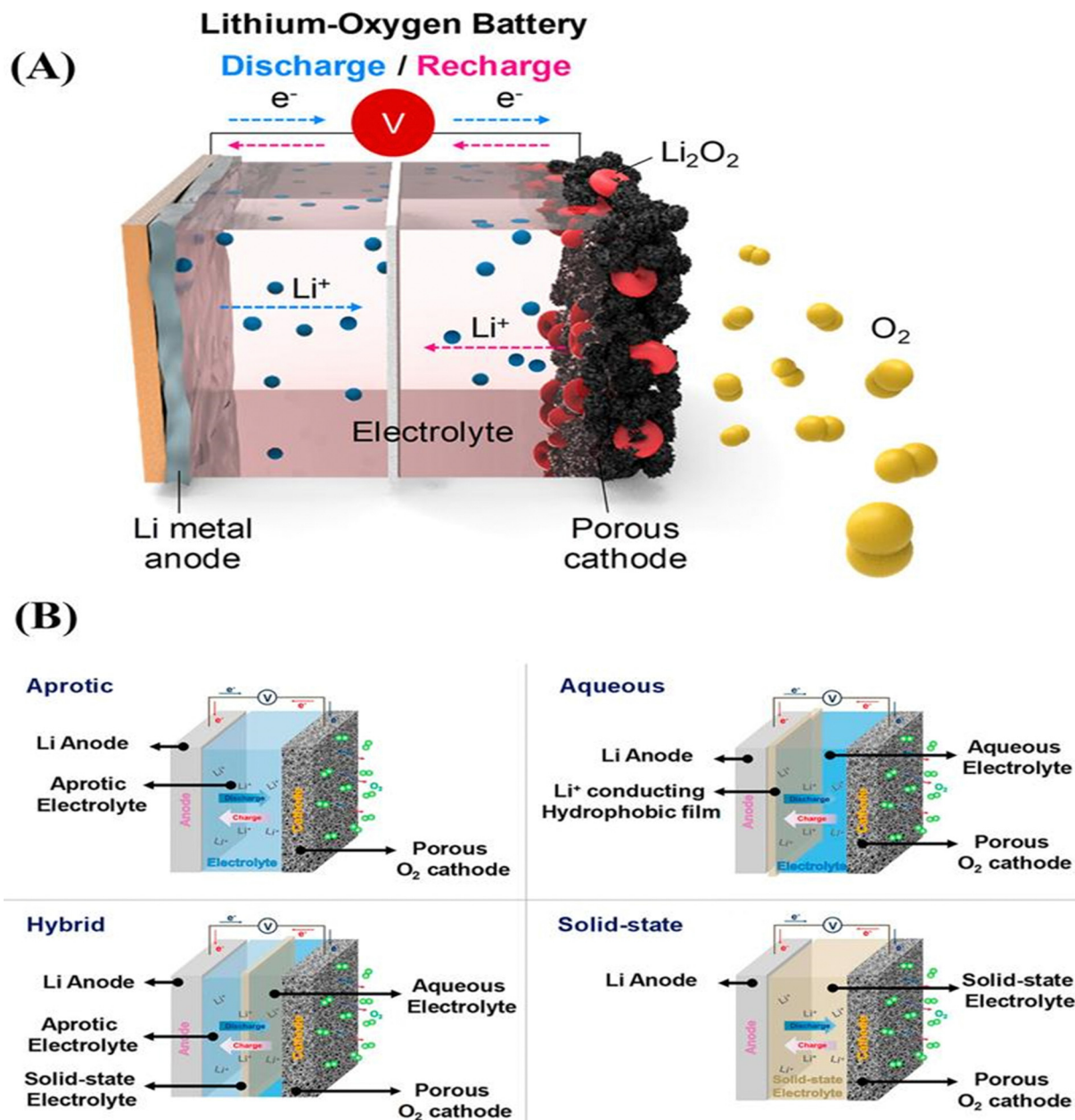
Fig. 9 (A) Schematic representation of a Li−O$_2$ battery. (B) Schematic configuration of all types of Li−O$_2$ cells.[145]

cathode materials used in these various ZIB types differ, further defining their unique characteristics.

According to Yuan et al.,[154] zinc-based batteries are predominantly used as primary batteries. Due to issues with recycling and disposal following usage, there has been significant resource waste and degradation of the environment.[155] As a result, the creation of an ideal anode made of zinc that is inexpensive, nontoxic, nonflammable, and highly water compatible is crucial. In addition to using an aqueous electrolyte, Fang et al.[156] reported rechargeable ZIBs with improved safety, cycle life, and accessibility, high current discharge performance[157] and greater ionic conductivity (10@1 to 6 S cm^{-1}).[158]

Although the overall construction of ZMBs is similar to that of NZBs, technically speaking, ZMBs are one of the ZIBs; the cathode material is typically MnO$_2$. However, ZMBs are frequently discussed separately due to the excellent properties of the manganese-based materials that other positive electrode materials lack.[153,159] Given their ZIB status, ZMBs inherit all of the ZIB's benefits by default, including low reduction potential, high specific capacity, stability, safety, and so forth.[160] Furthermore, low toxicity, low cost, and an abundance of reserves are the benefits of using manganese oxide as the positive electrode. Mao et al.,[153] explained that Zn air batteries (ZABs) and Zn–ion batteries are further, subdivided into Ni–Zn batteries (NZBs) and Zn–Mn batteries.
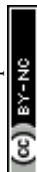
In contrast to standard commercial lithium-ion batteries, ZMBs do not have an exceptional specific capacity, and manganese oxide exhibits a low electrical conductivity and a slow rate of ion diffusion.[161] Furthermore, when manganese oxide is used, it deforms in certain ways and collapses, dissolving manganese in the electrolyte. These drawbacks have an impact on ZMB usage going forward as well.[162]

Additionally, all of these various ZIB variants use zinc metal anodes. Zinc anodes frequently provide a lot of benefits. (1) According to Li et al.,[163] they are reasonably priced and very simple to obtain. (2) Because of their low reduction potential, ZIBs' open-circuit voltage is raised, assuring their stability and safety. (3) Compared to other reactive metals, zinc is more stable and less reactive. (4) According to Sun et al.,[164] zinc anodes have a large volume capacity and a very high theoretical specific capacity. (5) ZIBs are highly environmentally friendly and typically do not release any poisonous or damaging compounds when used.

ZIBs have great qualities, but there are a lot of practical challenges with them. During use, zinc anodes can generate zinc dendrites, which can puncture the septum and cause the ZIBs to short circuit.[165] Additionally, the ZIBs' ion transport capacity needs to be enhanced.

Using a 3.0 M aqueous solution of $Zn(CF_3SO_3)_3$ as the electrolyte (Fig. 10), Nam et al.[157] created a 2D c-MOF, $Cu_3(HHTP)_2$, as a cathode material for rechargeable ZIBs. At 50 mA g^{-1}, $Cu_3(HHTP)_2$ had a high reversible capacity of 228 mA h g^{-1}. These maxima occurred at 0.65/1.10 V and 0.90/1.21 V (vs. Zn/Zn^{2+}), which correlate to the two-electron absorption of HHTP and the Cu^{2+}/Cu^+ redox process. Additionally, after 500 cycles, it retained 75% of its capacity, or 124.4 mA h g^{-1} at 4000 mA g^{-1}. With a Zn ion diffusion coefficient of 3.9×10^{-10} cm^2 s^{-1}, rapid redox reactions were evident. To improve the capacity and cycling performance of ZIB cathodes, Sang et al.[166] created a highly crystalline 1D c-MOF called Cu-BTA-H. Cu-BTA-H has several pore configurations and a π–d conjugated structure that resembles a rod that helps with ion transport. Because of its decreased band gap energy, electrochemical performance is improved by ion–electron transport that is greatly improved. The built ZIBs
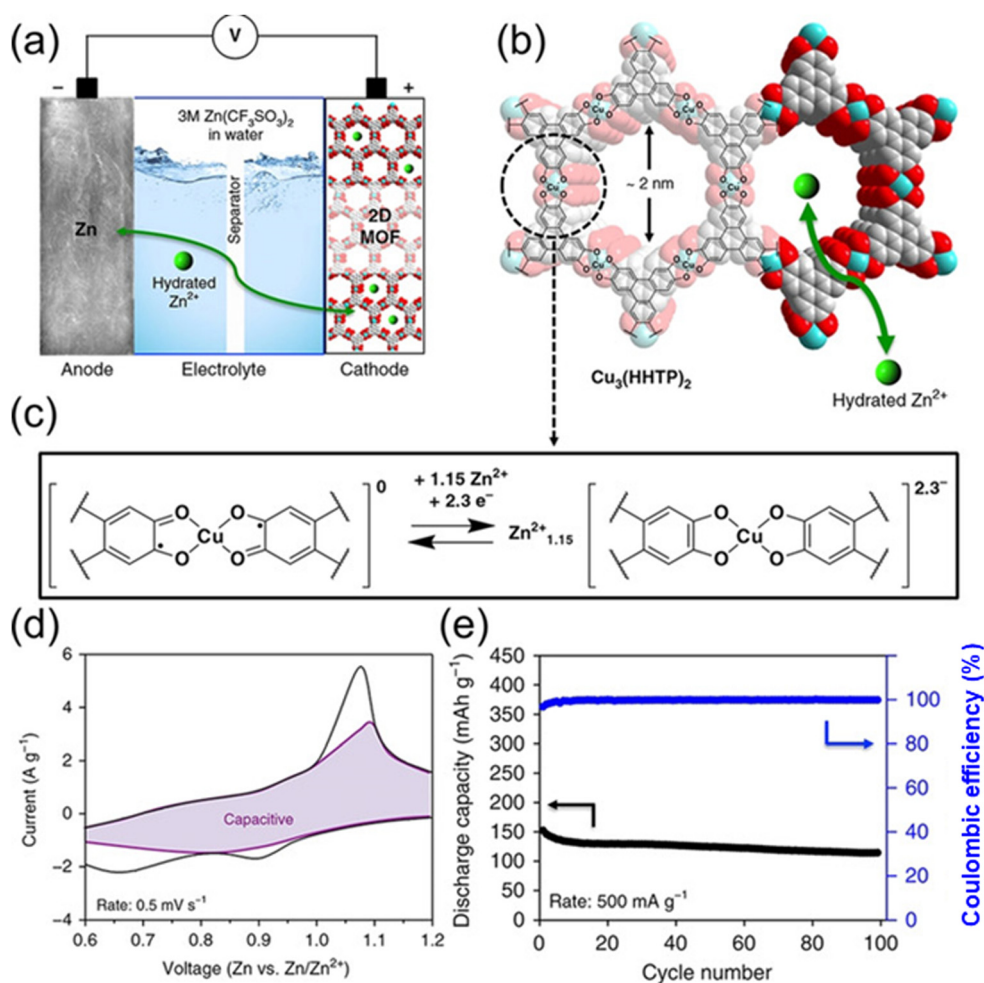

Fig. 10 $Cu_3(HHTP)_2$ acting electrochemically as a cathode for rechargeable ZIBs. (a) Zn-$Cu_3(HHTP)_2$ cell schematic depiction. (b) The $Cu_3(HHTP)_2$ chemical structure. (c) The anticipated redox mechanism in the Cu_3 coordination unit $(HHTP)_2$. (d) CV profile at 0.5 mV s @1, together with the capacitive contribution (shaded region). (e) Cycling efficiency at 500 mA g @1.[157]

maintained a capacity of 106.1 mA h g^{-1} after 500 cycles at a current density of 2.0 A g^{-1}, and they were able to attain a reversible capacity of 330 mA h g^{-1}at 0.2 A g^{-1}. Increased Zn^{2+} storage is made possible by the extra Cu^{2+}/Cu^{2} redox pair, which improves cycle stability and reversible capacity.

Li et al.[167] synthesized Ni–PTA–Mn, a 2D c-MOF intended to enhance the structural stability of electrode materials and inhibit deformation, using a hydrothermal process. This arrangement of parts resembles a flower and is characterized by a special hydrogen-bonded skeleton that was brought about by Mn. Conductivity is improved by the positively charged metal–H$_2$BDC framework, which increases Zn^{2+} diffusion. Because of this, ZIBs built with Ni–PTA–Mn demonstrated exceptional stability, retaining good capacity after more than 300 cycles and 93% discharge capacity after 100 cycles at 1 A g^{-1}. Outstanding long-term cycling stability was demonstrated by the reversible and steady production of zinc intermediates, as validated by in situ XRD.

He et al.[168] used solvent heat and a self-sacrificing method to synthesize V-MOF-48@CNTF, a 3D c-MOF. Through self-assembly, this V-based MOF created a cascading nanowire bundle structure along the CNTF substrate. ZIB electrochemical performance is greatly increased by the special design, which reduces ion diffusion distances, improves ion migration efficiency, maximizes surface area, and increases active sites. Later, Bing employed V-MOF-48@CNTF in all-solid-state fiber-optic ZIBs, which maintained over 80% capacity after 300 cycles at 2.0 A cm^{-3} and produced an energy density of 17.47 mW h cm^{-3} at 1.46 W cm^{-3}. This illustrates how 3D c-MOFs can improve ZIB applications and attributes.

2.3.6 Zn–air batteries (ZABs). Aqueous zinc–air batteries are the most developed class of metal–air batteries and have the most potential for use in future energy applications. The 1930s saw the emergence of commercial items.[169] With a theoretical energy density of 1086 W h kg^{-1} (including oxygen), zinc–air batteries are approximately five times more energy dense than lithium-ion batteries as they stand today. They may be produced for as little as ~10 $ per kW per h (ref. 170), which is around two orders of magnitude less expensive than lithium-ion batteries. Of all primary battery systems, zinc–air batteries provide the best energy density possible for a variety of applications.[169]

Fig. 11 illustrates the components of zinc–air cells: an air electrode with a gas diffusion layer and a catalytic active layer as the cathode, zinc metal as the anode, and a separator. Gaseous oxygen is used instead of liquid oxygen because oxygen is not very soluble at atmospheric pressure.[171,172] In this process, pressure differentials force atmospheric oxygen to penetrate into the porous carbon electrode, where a catalyst harnesses electrons produced by zinc oxidation at the anode to promote its reduction to hydroxyl ions in the alkaline electrolyte. This process, which is depicted in Fig. 11 (red circle), is called a three-phase reaction and involves a solid catalyst, liquid electrolyte, and gaseous oxygen. In zinc–air batteries, this structural layout improves oxygen uptake. Zinc–air batteries (ZABs) are effective in aqueous electrolytes because of their high specific energy of 1218 W h kg^{-1} and volume energy density of 6136 W h L^{-1}.[173]

According to Guan et al.,[175] ZABs generally consist of four main parts: an alkaline electrolyte, a separator, a zinc electrode, and an air electrode with a catalyst-coated gas diffusion layer. ZABs provide electricity when they discharge by connecting zinc metal to the air electrode in an alkaline setting.[176] As atmospheric oxygen diffuses into the porous air electrode, an oxygen reduction process converts it to hydroxide ions. As these hydroxide ions move toward the zinc electrode, they create Zn(OH)$_4$$^{2-}$, which, in supersaturated circumstances, breaks down into insoluble ZnO.

Zinc–air batteries (ZABs) rely heavily on the ORR and OER, which have a major impact on their reaction rates.[177] On the other hand, the oxygen redox process occurs kinetically slowly during the charge–discharge cycle. Electrocatalysts are
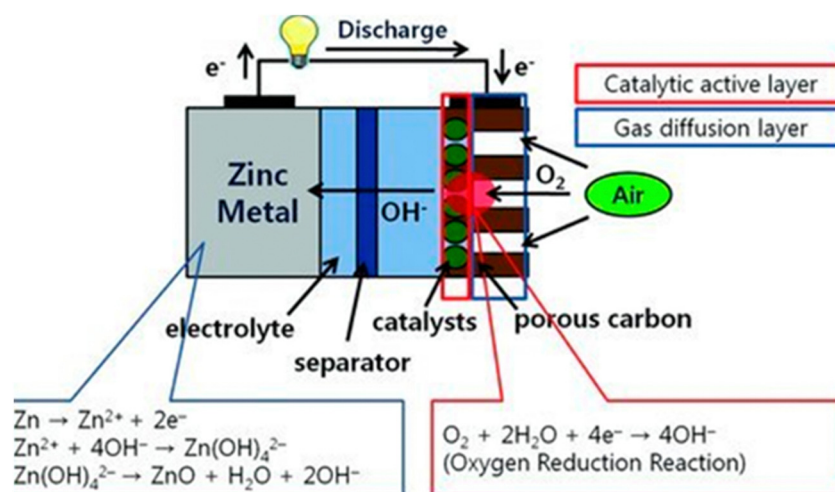
Fig. 11 Working principle and each electrode reaction of zinc–air batteries. Note the red circle where a three phase reaction (oxygen (gas), catalysts (solid) and electrolyte (liquid)) occurs in the air cathode.[174]

frequently used to improve this process.[178] Because of their high specific surface area, porosity, and variety of architectures, MOFs are widely used in ZAB catalyst synthesis.[179] Nevertheless, the electrical conductivity of pure MOFs is low. Consequently, to greatly increase the electrochemical performance of ZABs, modified c-MOFs, which have enhanced electrical conductivity, are favored as electrocatalysts.[180]

Pan et al.[181] created a Ru-doped c-MOF, $Ni_{5.7}Ru_{0.3}(HHTP)_3(H_2O)_x$, for use in ZABs, based on the superior charge transport capabilities of 2D-MOFs with π–π and π–d orbital overlap. When tested at 0.05 S m^{-1}, $[Ni_{5.7}Ru_{0.3}(HHTP)_3(H_2O)_x]$ showed better electrical characteristics than other pure MOFs. Moreover, solid-state ZABs built using this c-MOF showed good stability and strong charge/discharge performance for a period of more than 200 cycles. Motivated by this possibility, Li created a 3D c-MOF called Co-CAT/NiFe-LDH/CNFs by synthesizing Co-CAT using solvent heat and integrating c-MOFs onto NiFe-LDH/CNFs.[182] It was mostly composed of nanosheets organized in arrays with embedded nanorods. With solid electrolytes, assembled ZABs demonstrated superior stability and high power density, attaining 112.04 mW cm^{-2} at 11 mA cm^{-2} for more than 11 hours. Furthermore, after 56 hours of cycling at the same current density, the batteries showed minimal capacity loss and stability in liquid electrolytes, underscoring their great potential for real-world uses.

2.3.7 Calcium-ion batteries (CIB). Calcium-ion batteries (CIBs) have gained interest as possible lithium-ion battery (LIB) substitutes throughout the last seven years. The fifth most abundant element in the crust of Earth, calcium has low reduction potential (-2.87 V vs. SHE, 0.17 V higher than Li/Li$^+$ and 0.5 V lower than Mg/Mg^{2+}), theoretically competitive volumetric and gravimetric capacities, and great promise for secondary battery applications.[183] Precursors for calcium are also far less expensive than those for sodium and lithium.[184]

Additionally, because calcium ions are less polarizing than Mg-ions, they have better reaction kinetics, which could improve performance.[185] Furthermore, because CIBs cannot facilitate dendritic formation, which can result in short circuits and explosion, they are safer than LIBs.[186] But CIB development is still in its infancy, and before going on sale, a few characteristics like superior electrolytes and high-performance cathodes need to be refined.

Using non-aqueous electrolytes in both three- and two-electrode cells, the majority of earlier research on CIB applications was conducted.[187] Designing electrode materials that can withstand the enormous size of Ca^{2+} ions during charging and discharging without suffering significant structural damage is still a difficult task nevertheless. There have been several reported solutions to these cathode problems, including as the utilization of framework-based materials and metal oxides.[188,189]

At a rate of 0.5C, KVO exhibited a reversible 60 mA h g^{-1} Ca–ion intercalation capacity, maintaining 92% of its capacity after 100 cycles. The capacity increased to 78–100 mA h g^{-1} with an average voltage of ~ 3.0 V versus Ca/Ca^{2+} when the current flow was reduced to 0.1C. Prussian blue nanodisks made from

Prussian green and NaI reduction were described by Vo et al.[189] In a full-cell configuration with Ni-MOF as the anode, the optimal sample, $Na_{1.09}FeFe(CN)_{5.11}(CO)_{0.89}$-PAAPANi11(PB41_16/PAAPANi11) demonstrated promising Ca-storage behavior, achieving a specific capacity of 77.6 mA h g^{-1} at 100 mA g^{-1} current density. This impressive capacity retention of 91.0% was significantly higher than that of other Prussian blue analogues. For this reason, creating high-performance cathodes for CIB applications through the use of metal oxides and framework-based materials offers considerable potential.

2.4 MOFs for fuel cells

In recent times, fuel cells have garnered considerable interest due to their exceptional efficiency, high energy density, and minimal release of detrimental gases.[190] Fuel cells, in contrast to most batteries, which store chemical energy inside the cell, use a continuous flow of chemical energy from outside the cell in the form of fuels (such as hydrogen, natural gas, and methanol) to produce electricity for use in stationary buildings, cars, and portable appliances. Internal combustion engines are not as eco-friendly as fuel cells; thus, they could be a viable replacement. An anode, a cathode, and an electrolyte are the three main components of fuel cells. Fuel is often oxidized at the anode using a catalyst to produce electrons and ions, which are subsequently transported to the cathode by the electrolyte for the ions and an external circuit for the electrons. At the cathode, a second catalyst is employed in conjunction with the electrons and ions to lessen the oxygen that is often provided by the air.

Research has been done on MOFs and their derivatives as potential electrode catalysts, electrolyte-holding membranes, and less expensive alternatives to catalysts based on precious metals. Several important electrocatalytic applications, including the following: (a) MOFs for the hydrogen evolution reaction (HER), (b) MOFs for the oxygen reduction reaction (ORR), and (c) composites of MOFs and proton conductive polymers for membranes, are the main drivers of the use of MOFs for increasing efficiency and lowering the cost of fuel cells.[191]

Fenoy et al.[192] presented a compressive example of using a ZIF-8 top layer as an O$_2$ adsorbent to raise the oxygen content on the conducting polymer catalytic surface. The ZIF-8 layer improved the O$_2$ uptake from the solution, which improved the ORR in neutral media. Bureekaew et al.[193] reported the encapsulation of imidazole (Im) molecules into aluminum MOFs, whereby Im@{Al(μ_2-OH) (1,4-NDC)}$_n$ (1,4-NDC = 1,4-naphthalenedicarboxylate) and Im@{Al(μ_2-OH) (1,4-BDC)}$_n$ present enhanced conductivities of 2.2×10^{-5} and 1.0×10^{-7} S cm^{-1}, respectively, when compared to those of their parent MOFs at 120 °C. In a different investigation, Gui et al.[194] synthesized a Zr-MOF with anionic zirconium phosphate chains supported by NH$_4^+$ cations, creating a continuous N–H/O–P chain for improved anhydrous proton conductivity. Taylor et al.[195] reported a different study that utilized a zirconium–sulfoterephthalate MOF as an example to show how the defect affects proton-conducting behavior. The defect-containing samples were created by either immersing the prepared sample in

0.1 M H$_2$SO$_4$ or adding excess acetic or sulfoacetic acid during the preparation process.

According to Ji *et al.*[196] multi-heteroatomic doping (*e.g.*, N, Co, P, B, S, *etc.*) is frequently applied to MOF-derived 1D PCNFs or HCNFs to enhance their ORR by changing their surface polarity and electrical characteristics. They also described the one-step procedure for the tunable synthesis of ZIF-67 and PAN electrospun into carbon microsphere/nanofiber hybrids (CSFHs), and they showed how this process could be used to control the morphology of a nanofiber that resembled a pearl

necklace to a microsphere/nanofiber 3D structure by varying the ZIF-67/PAN ratio.[197]

In the past, a bimetallic Zn, Co-ZIF was combined with electrospun Co^{2+}/PAN fibers to create MOF-based hierarchical carbon fibers containing N, C (Fig. 12a and b). In comparison to Zn, Co-ZIF derived carbon (ZIF-C) and Zn, Co-ZIF free carbon fibers (CP-CFs) (Fig. 12c and d),[198] the ZCP-CFs demonstrated high activity for the ORR in 0.1 M KOH. These features included a more positive half-wave potential (0.135 V *vs.* Ag/AgCl), higher diffusion-limited current density (5.95 mA cm^{-2}) and kinetic
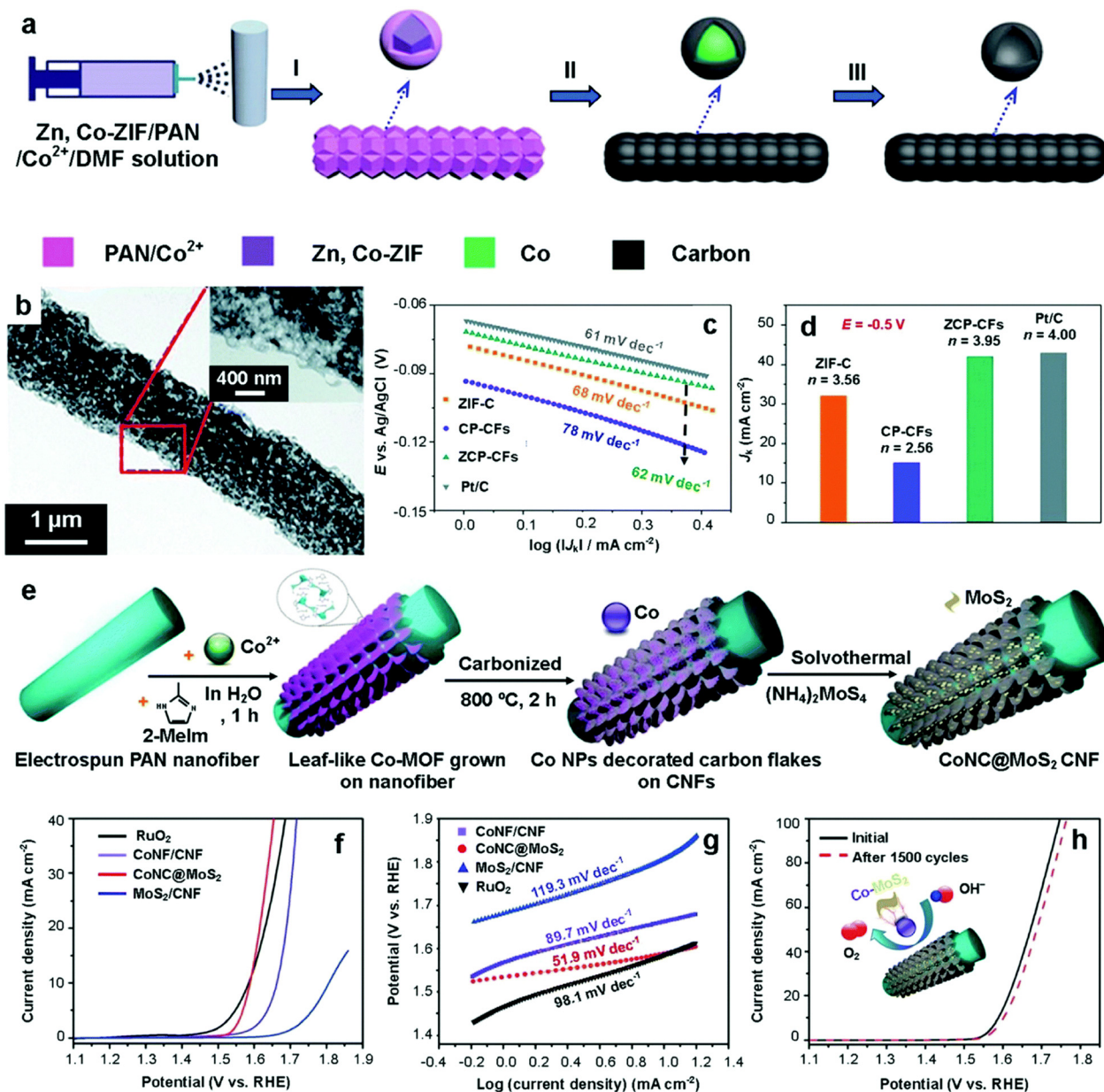
Fig. 12 (a) Schematic illustration of the preparation of the Zn, Co-ZIF-based hierarchical carbon fibers (ZCP-CFs) and (b) the corresponding TEM image of ZCP-CFs. (c) Tafel plots of ZIF-C, CP-CFs, ZCP-CFs, and Pt/C. (d) Kinetic-limiting current densities of ZIF-C, CP-CFs, ZCP-CFs-9, and Pt/C.[198] (e) Schematic illustration of the fabrication of free-standing MoS$_2$ nanosheet grafted Co–N-doped carbon flakes grown on electrospun carbon nanofibers (CoNC@MoS$_2$/CNF). (f) Polarization curves of CoNC@MoS$_2$/CNF, MoS$_2$/CNF, CoNC/CNF, and RuO$_2$ in 1 M KOH in the OER. (g) OER Tafel plots of CoNC@MoS$_2$/CNF, MoS$_2$/CNF, CoNC/CNF, and RuO$_2$ in 1 M KOH. (h) OER cycling stability of CoNC@MoS$_2$/CNFs in 1 M KOH.[196]

limiting currents, a lower Tafel slope (62 mV dec^{-1}), and higher selectivity (the number of electrons transferred, n = 3.97). The number of researchers working around the clock to create bifunctional catalysts for water splitting has grown recently.

The hydrogen evolution reaction (HER) can be effectively catalyzed by molybdenum disulfide (MoS$_2$); however, its low electrical conductivity limits both its charge transfer rate and electrocatalytic effectiveness. The solution to this problem is shown schematically in Fig. 12e, where MoS$_2$ nanosheets were formed on carbon fibers generated from ZIF-67/PAN to increase their electrical conductivity. Furthermore, using the CoN-C@MoS$_2$/CNFs for the oxygen reduction reaction (ORR) in 1 M KOH electrolyte, they showed a better catalytic activity with a low $Z10$ value of 350 mV compared to MoS$_2$/CNFs and CoNC/CNFs (570 mV and 430 mV, respectively) (Fig. 12f). Additionally, as shown in Fig. 12g, the CoNC@MoS$_2$/CNFs displayed a low Tafel slope of 51.9 mV^{-1}, which was significantly lower than those of CoNC/CNF (89.7 mV^{-1}), MoS$_2$/CNF (119.3 mV^{-1}), and RuO$_2$ (98.1 mV^{-1}). This suggests that the CoNC@MoS$_2$/CNFs have high catalytic activity and enhanced catalytic kinetics.[196] Further evidence of the exceptional OER stability of CoN-C@MoS$_2$/CNFs in a basic medium comes from the observation of a 17 mV increase in the $Z100$ value after 1500 continuous cycles (Fig. 12h).

Proton migration networks that are independent of water can be achieved by introducing acid–base pairs through linker alteration or guest encapsulation, as demonstrated by previous research. In an experiment, Dong et al.[199] embedded isomorphous UiO-66 nanocrystals (40–100 nm) attached to NH$_2$ and SO$_3$H in a sugar-based chitosan polymer network. On the other hand, Guo et al.[200] focused on creating a hybrid in which they threaded a zwitterionic polymer containing sulfonate and quaternary ammonium groups through ZIF-8, resulting in improved proton transfer. In addition to the previous quest encapsulation technique, Chen et al.[201] reported adding several ionic liquids to the ~500 nm pores of MIL-101 nanoparticles in order to produce enhanced proton conductivity via acid–base interactions.

A thorough explanation of the low-temperature area and the first proton-conducting MOF, $\{(NH_4)_2(adp)[Zn_2(ox)_3] \cdot 3H_2O\}_n$ (ox = oxalic acid, adp = adipic acid), was provided by Sadakiyo et al.[202] Water molecules, NH$_4^+$ ions, and the carboxyl groups of adipic acid acted as conducting media, which performed similarly to Nafion. At 98% relative humidity (RH) and 25 °C, this MOF exhibits proton conductivity as high as 8×10^{-3} S cm^{-1}. When compared to Nafion, this MOF exhibits a greater activation energy (E_a) of 0.63 eV, suggesting that both Grotthuss and vehicle processes are involved in the proton conduction.

3. Environmental applications of MOFs

MOFs have several potential uses due to their superior qualities (large surface area, pore size controllability, and chemical and thermal endurance). Furthermore, they are also easily tunable to get desired characteristics. MOFs are ideal adsorbents for environmental applications because of their extremely high porosity (about 90% free volume) and specific surface areas (typically greater than 7000 m^2 g^{-1}).[203] To eliminate these contaminants from either air or water, adsorbents such activated carbon, zeolite, metal oxide, resin, and biomass are typically used. Nevertheless, the majority of these materials have issues with their low adsorption capability, especially for low-level pollutants, and their high regeneration energy consumption. Furthermore, it is simple to alter their surface in order to include more functional groups that can help with the adsorption of specific contaminants.[204] On the effectiveness of MOFs as adsorbents, numerous studies have been published. The ability to selectively adsorb gases is made possible by MOFs' enormous surface area and various pore diameters. The storage of hydrogen, methane, and carbon dioxide has been studied in relation to MOFs. MIL-101 and ZIF-8, for example, are two MOFs that have shown promise in the adsorption of carbon dioxide. These MOFs can release carbon dioxide after selectively adsorbing it under certain conditions.[205–207] The potential application of MOFs in water filtration has been studied. MOFs can be used to remove organic materials, heavy metals, and pharmaceuticals from water.[208] The effectiveness of MOFs as adsorbents has been the subject of numerous investigations.

3.1 Adsorption

3.1.1 Adsorption of dye pollutants. Given the availability of a library of anionic and cationic dyes, electrostatic interactions are thought to be one of the most significant types of non-covalent interactions involved in the binding of dye molecules by MOFs. For coloring cotton, silk, and wood, these dyes have been widely employed in industry.[209] Ionic dyes are hazardous and used widely; hence, many MOFs have been created for their capture. In most cases, AC, zeolites, and chitosan beads are frequently used to remove colors like methyl orange (MO), methylene blue (MB), and malachite green (MG). Comparing MIL-100(Fe), MIL-101(Cr), MIL-53(Al), and AC, it was shown that MIL-100(Fe) had a greater adsorption capacity (146 mg g^{-1}) for MG than the other three adsorbents. The electrostatic interaction between MOF and MG was suggested as the cause of MIL-100(Fe)'s excellent adsorption capacity and selectivity.[210] The robust π–π interaction between the guest and host molecules was responsible for this performance, which exceeded several other conventional adsorbents' criteria.

An experiment to synthesize hierarchically mesostructured MIL-101(Cr) by using cetyltrimethylammonium bromide (CTAB) as a surfactant to remove methyl blue MB was reported in ref. 211. For the adsorptive removal of MB in the liquid phase, the material displayed dramatically faster adsorption kinetics. In around 110 minutes, they noticed that all of the MB molecules with a 30 ppm initial concentration had been adsorbed onto the hierarchically mesostructured MIL-101(Cr). In another development, for the purpose of removing methylene blue (MB) dyes from aqueous environments, Li et al.[212] investigated the use of MOF/graphite oxide hybrid (MOF/HKUST1) materials. Investigations were also conducted into

the isothermal, kinetics, and regeneration studies. It was discovered that the adsorption of MB followed both the Freundlich and Langmuir adsorption isotherms. Finally, it was discovered that HKUST-1/GO had superior reusability and a greater capacity for MB dye adsorption.

In order to capture the Brilliant Blue R-250 (BBR) dye molecule from aqueous solution, Liu et al.[213] produced a number of three-dimensional 4,4-connected MOFs based on copper paddlewheel secondary building units and tetracarboxylate linkers made from tetraphenylmethane. There was a direct correlation between the pore diameters of the 4,4-connected MOFs and the dye uptake. The maximum dye absorption capability of the MOF with the biggest pore size was 73 wt%, whereas MOFs with pores smaller than the dimensions of BBR-250 showed negligible dye uptake. The batch adsorption approach was used to remove the methyl red (MR) dye using MOFs loaded onto iron oxide nanoparticles (Fe_3O_4@MIL-100(Fe)).[214] When compared with other adsorbents, the MR removal onto MIL-100(Fe) demonstrated an improved capacity.

For the adsorptive removal of methyl orange, Haque et al.[215] reported the use of two MOFs based on chromium terephthalates, namely MIL-53(Cr) and MIL-101(Cr). Both MOFs were superior to activated carbon in the adsorption of methyl orange, with MIL-101(Cr) showing a higher adsorption capacity than MIL-53(Cr). The adsorption capacities and kinetic constants were in the following order: activated carbon < MIL-101(Cr) < ethylenediamine-grafted MIL-101(Cr) (or ED-MIL-101(Cr)) < protonated ethylenediamine-grafted MIL-101(Cr), and PED-MIL-101(Cr), with a 194 mg g^{-1} adsorption capacity. The cationic PED-MIL-101(Cr) MOF displayed the strongest interaction with the anionic methyl orange molecules because protonated PED-MIL-101(Cr) was positively-charged, and ED-MIL-101(Cr) also displayed a partial positive charge, suggesting that electrostatic interactions were involved in the adsorption mechanism.

Adsorption of methyl orange and methylene blue onto Fe_3O_4–PSS@ZIF-67 (PSS = polystyrene sulfonic acid) with a core–shell structure, named MZIF-67, was reported by Yang et al.[216] According to the tests, an amount of 5 mg and an initial concentration of 400 mg L^{-1} resulted in an optimum adsorption capacity of 738 mg g^{-1} within 7 hours. This outstanding performance was attributed to its high porosity, the presence of unsaturated cobalt sites, and magnetic characteristics, which further increased the removal efficiency for methyl orange and methylene blue. Further investigation revealed that MZIF-67 has the selectivity ability to gradually separate the methyl orange dye from a mixture of solutions that contained 0.04 mg L^{-1} methyl orange and methylene blue dyes. As a result, the removal rate and separation efficiency were both increased to 92 and 96%, respectively.

According to ref. 217, defective UiO-66(Zr) was synthesized utilizing hydrochloric acid as a post-synthetic treatment and benzoic acid as a modulator. The adsorption capacity of safranin T was found to be nine times higher in the faulty MOF (366 mg g^{-1}) than in the defect-free counterpart (30 mg g^{-1}).

Because of the size-exclusion effect, the defective UiO-66(Zr) was nevertheless able to selectively adsorb safranin T over crystal violet in spite of having a bigger cavity and a more uniform distribution of pore sizes.

Under different circumstances, Lin and Chang[218] reported the adsorption of malachite green onto zeolite imidazole frameworks (ZIFs) at 20 °C, with an adsorption capacity of 1500 mg g^{-1}, which quickly increased to 2500 mg g^{-1} at 60 °C. This demonstrated that raising the temperature of the adsorption process had a beneficial effect on the system's performance. After four cycles, the ZIF-67 regeneration and reusability study revealed a 95% discharge rate for regeneration, making it an effective adsorbent for removing the malachite green dye.

Qin and Zeng[219] reported the preparation of ultra-small nanoparticles of several MOFs, such as HKUST-1, ZIF-8, and ZIF-67, supported on copper silicate nanotubes (CuSiNT), for the adsorption of methyl orange, Congo red, and thymol blue. The CuSiNT-supported HKUST-1 nanocomposites exhibited improved methyl orange, Congo red, and thymol blue adsorption when compared with their microsized counterparts. The increased adsorption capability was due to the CuSiNT support, which might offer more accessible functional groups and open metal sites and thus reduce the dye molecules' diffusion barrier in the process. Wang et al.[220] reported the potential of a crystalline triazine-based organic framework (CTF) as a promising adsorbent for removing organic dyes. This material showed an uptake of 0.48 mmol g^{-1} for RhB within 55 min (the weight ratio of RhB/CTF was 0.24), with the adsorption capability for RhB onto CTF reaching 1.01 mmol g^{-1}, showing that CTF was more effective in removing Rhodamine B (RhB).

Haque et al.[221] expanded their research to a MOF based on iron terephthalate, MOF-235(Fe) or [Fe_3O(terephthalate)$_3$(DMF)$_3$][$FeCl_4$]. Despite being non-porous to nitrogen at low temperatures, this MOF absorbed both anionic methyl orange and cationic methylene blue dyes in the liquid phase. With MOF-235, MO and MB had adsorption capacities of 477 and 187 mg g^{-1}, respectively, in comparison with just 11 and 26 mg g^{-1} for each respective dye with activated carbon. They also confirmed that the solution pH had a significant impact on the adsorption of the MO and MB dyes. It was posited that the positive charge density on the MOF-235(Fe) decreased at higher pH levels, leading to a reduction in the adsorption of methyl orange. A low pH value enhanced the negative charge density of the MOF's, which boosted the adsorption capacity for methylene blue.

In another development, MIL-101(Al) was functionalized with amino groups to produce NH_2–MIL-101(Al).[222] NH_2–MIL-101(Al) showed a high methylene blue adsorption capability of up to 762 mg g^{-1}. It was posited that the electrostatic interactions between the MOF and methylene blue increased as a result of the presence of amino moieties on the MOF surface. However, the MOF's X-ray photoelectron spectrum showed that structural changes happened to the MOF during the adsorption procedure and that about 30% of the Al(III) ions were lost to the solution, rendering the MOF useless. A single-walled metal–organic nanotube with an armchair (3,3) structure,

([CH$_3$NH$_3$][Zn(NTB)(NMF)])·4.5NMF (H$_3$NTB = 4,4′,4′′-nitrilotris-benzoic acid, NMF = N-methylformamide), has recently been discovered by Zhou et al.[223] and reported to display an interior channel diameter of 21 Å. The metal–organic nanotube adsorbed dye molecules (i.e., basic red 9 and basic violet 14) with remarkable efficiency (>1650 mg g^{-1}), because of the vast open mesoporous channels.

Another advancement was made by Huo and Yan,[210] when they developed MIL-100(Fe) for the adsorption of the cationic triphenylmethane dye (i.e., malachite green). The study showed that MIL-100(Fe) demonstrated an adsorption capacity of 205 mg g^{-1} at room temperature, which was much greater than those of MIL-101(Cr) and MIL-53(Al). Electrostatic interactions played a role in the adsorption mechanism, as evidenced by the dependence of the adsorption process on pH and the zeta potential measurements. Malachite green and MIL-100(Fe)'s benzene rings also interacted with one another in a π–π fashion. Malachite green was demonstrated to adsorb on MIL-100(Fe) in an endothermic manner, with an increase in adsorption capacity at higher adsorption temperatures. Thermodynamic investigations showed that a positive entropy change is beneficial for the spontaneous adsorption of malachite green on MIL-100(Fe), whereas a positive enthalpy change is undesirable. The open metal sites in MIL-100(Fe) were occupied by water molecules, which may help to explain this. On the other hand, the weaker adsorption of malachite green would be caused by the absence of open metal sites in MIL-53(Al) and the repulsion brought about by surface positive charges on MIL-101(Cr).

In a different study, Li et al.[224] prepared NH$_2$–MIL-53(Al) for the adsorption of the cationic dyes methylene blue and malachite green using the amino functional group. The adsorption process in this instance was not fueled by electrostatic interactions, as evidenced by the comparison of the pH-dependent adsorption studies. Instead, it was found that the amino hydrogen of NH$_2$–MIL-53(Al) and the nitrogen atoms on methylene blue or malachite green exhibited strong hydrogen bonding interactions. The benzene rings of NH$_2$–MIL-53(Al) and the dye molecules also had weak π–π interactions with one another. Seth et al.[225] prepared an anionic trinuclear cadmium MOF using the tetratopic carboxylate ligand 3,3′,5,5′-tetrakis(p-carboxyphenyl)-2,2′,6,6′-tetramethoxy-1,10-biphenyl. This cadmium MOF demonstrated remarkable flexibility and durability and permitted post-synthetic metal exchange with several main groups and lanthanide ions, to produce new MOFs with the same structure. Particularly, the production of cationic MOFs, which have substantially different dye adsorption characteristics, resulted from the substitution of trivalent lanthanide ions for the divalent cadmium ions in the divalent cadmium solution. The anionic dye, bromophenol blue, was selectively adsorbed by the isostructural europium MOF, from a mixture that contained neutral or cationic dyes, in contrast to the parent cadmium MOF, which preferentially adsorbed only cationic methylene blue.

Dong et al.[226] used (E)-4-(2-carboxyvinyl)benzoic acid (H$_2$L) to prepare the cadmium MOF, [[CdL(H$_2$O)]·4DMF·2H$_2$O]. The adsorption of rhodamine B (RhB) by the MOF led to the formation of a luminous adduct. RhB@MOF experienced ligand-to-dye energy transfer, which caused the ligand and RhB emissions to be detected at 420 and 595 nm, respectively, even though the emission of RhB was suppressed in a ground mixture with the MOF. Luo and Wang[227] carried out an experiment on the use of composites formed from MIL-100(Fe) and graphene oxide nanosheets, which were discovered to have a sandwich-like structure when the decomposition temperature increased from 280 to 350 °C. At a graphene oxide loading of 5%, it was discovered that this composite material had improved methyl orange and methylene blue adsorption capabilities from aqueous solution. MOF composites made from ZIF-8 with either graphene oxide or carbon nanotubes were also employed by Abdi et al.[228] The composite materials in this example showed significantly improved malachite green adsorption capabilities, with maximum values of 1667, 2034, and 3300 mg g^{-1} for ZIF-8, ZIF-8@CNT, and ZIF-8@GO, respectively, at room temperature. The potential for practical applications of these composite materials was demonstrated by the increased uptake of malachite green and preservation of their adsorption ability in real wastewater at increasing temperatures.

Li et al.[229] studied the adsorption characteristics of the Fe$_3$O$_4$/HKUST-1/GO hybrid toward methylene blue. With a better dye adsorption capacity than the more straightforward Fe$_3$O$_4$/HKUST-1 composite, the three-component Fe$_3$O$_4$/HKUST-1/GO composite demonstrated a good match in channel diameter and molecular breadth with methylene blue despite having a smaller specific surface area. The adsorption capability of Fe$_3$O$_4$/HKUST-1 was observed from desorption and regeneration studies to rapidly decrease with increasing numbers of cycles, from virtually quantitative adsorption to barely 60% after recycling for five times. The adsorption capacity of methylene blue for Fe$_3$O$_4$/HKUST-1/GO in the presence of graphene oxide as a component material was only marginally reduced, and the value remained over 90% after 5 cycles. Recent research conducted by Pei et al.[230] developed MOF-polymer composites from HKUST-1 and a biocompatible binder consisting of calcium alginate and gelatin using three-dimensional (3D) printing technology. Methylene blue, malachite green, methyl violet, rhodamine B, and auramine O were the organic dyes that the 3D-printed composites adsorbed, and the adsorption performance depended on the printing geometry and the size and loading of the MOFs.

For dye removal from aqueous solution many MOF-based adsorbents have been employed, and the adsorption capacities of these arrays of adsorbents for dye removal are presented in Table 1.

In summary, the carcinogenic effects of synthetic dyes on humans and aquatic life make them a serious environmental issue when it comes to water contamination. While adsorption is a popular method for eliminating dyes from wastewater, traditional adsorbents are sometimes ineffective for usage in industrial settings. These drawbacks can be overcome by using metal–organic frameworks (MOFs), which have good dye
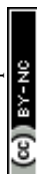
Table 1 Dye removal from aqueous solution and wastewater by MOF-based adsorbents

Adsorbate	Adsorbent	Adsorption capacity (mg g^{-1})	Time (min)	Ref.
Congo red	Ni–Cu MOF	999.20	240	231
	TMU-7(Cd)	97	45	232
	Ni-MOF	276.7	300	233
	Zn-MOF	132.2	300	233
	Ni–Zn MOF	460.90	300	233
	TFMOF(Zr)	252.25	10	234
	Ce(III)-doped UiO-67	799.6	80	235
	ln–TATAB	299	10	234
	Co-MOFs	4885.20	720	236
Methylene blue	UiO-66	69.8	120	237
	Zn-MOF	326	60	238
	Fe_3O_4@-SiO_2@UiO-66	116	60	239
	Fe_3O_4@-SiO_2@UiO-66-NH_2	128	60	239
	Fe_3O_4@-SiO_2@UiO-66-urea	121	60	239
	Fe_3O_4@MIL-100(Fe)	221	5–1440	240
	UiO-66-P	91.1	Over 1440	241
	MIL-100(Fe)	1105	10–1440	242
	Fe_3O_4@MIL-100(Fe)	73.8	420	243
	$H_6P_2W_{18}O_{62}$@$Cu_3(BTC)_2$	298.34	60	244
	MIL-68(Al)	1666.67	8	245
	BUT-29	1119	6	246
	UiO-66	543.48	300	247
	GO–Cu-MOF	262	1440	248
	CuBDC	41.01	20	249
	Ce(III)-doped UiO-67	398.9	80	235
	USTC-1	26.6	240	250
	ABim–Zn-MOF	174.64	60	251
Methyl orange	UiO-66	83.7	120	237
	Fe_3O_4@-SiO_2@UiO-66	219	60	239
	Fe_3O_4@SiO_2@UiO-66-NH_2	130	60	239
	Fe_3O_4@SiO_2@UiO-66-urea	183	60	239
	Ce(III)-doped UiO-67	401.2	80	235
	USTC-1	0.8	240	250
Rhodamine B	MIL-125(Ti)	59.92	180	252
	Zn-MOF	3.75	60	238
	$MgFe_2O_4$@MOF	219.78	5	253
	POM@UiO-66	222.6	120	254
	Fe_3O_4/MIL-100(Fe)	28.36	90	255
	In-MOF@GO	267	60	256
	MIL-68(Al)	1111.11	10	245
	USTC-1	13.4	240	250
Methyl orange	SCNU-Zl-Cl	285	60	257
Acid orange A	SCNU-Zl-Cl	180	60	257
Congo red	SCNU-Zl-Cl	585	60	257
Methyl blue	SCNU-Zl-Cl	262	60	257
Malachite green	Cd-ZIF	395.87	70	258
Malachite green	ZIF-8	1000	180	259
Malachite green	POM@UiO-66	190.6	120	254
Orange G	POM@UiO-66	40	120	254
Chicago sky blue	ABim–Zn-MOF	144.26	60	251
Methyl red	Fe_3O_4@MIL-100(Fe)	625	360	214
Acid red 18	CoOF	44.26	500	260
Rose Bengal	SmBTC	380	1440	261
Crystal violet	BUT-29	832	4	246
Acid chrome blue K	ln–TATAB	343	10	262
Acid red 26	ln–TATAB	259	10	262
Direct black 38	ln–TATAB	242	10	262
Orange II	ln–TATAB	217	10	262

removal and degradation properties because of their multi-functionality, water stability, wide surface area, adjustable pore size, and recyclability. Magnetic MOFs continued to function well after several cycles.

3.1.2 Adsorption of heavy metal pollutants. A lot of research has been done on MOFs and MOF-based composites as possible adsorbents for heavy metal removal because of their

intriguing structure and notable physical characteristics, which include flexibility, functionality, tunable pore size, large pore volume, high specific surface area, and the potential for case-specific customization of fundamental molecular architecture.[2] With careful selection of a metal ion and an organic linker, the structure of a MOF can be designed. The topology, structural properties, and metal speciation of MOFs all influence the

mechanism of heavy metal ion adsorption. Metal ions may transpire *via* diffusion into the MOF's core or *via* interactions at the framework's surface.[263] These interactions may take the form of chemical bonds, coordination interactions, electrostatic interactions, acid–base interactions, van der Waals contacts, or chemical bonding.[264–266] Compared to other common adsorbents such as activated carbon, zeolite, and mesoporous silica, these characteristics make the MOFs more appealing.

3.1.2.1 Arsenic. Arsenic is extremely harmful and causes cancer. Both the arsenate, As(v), and arsenite, As(iii), forms are lethal to all living things.[267] When it comes to metal ion pollution, the World Health Organization (WHO) has designated arsenic pollution as the top concern.[268] The WHO recommends a maximum tolerable content of 10 $\mu g\ l^{-1}$ for arsenic in drinking water.[269] It is estimated that each year more than 60 kg of arsenic are emitted into the atmosphere.[270] Various approaches have been implemented to eliminate As(iii) and As(v) from wastewater. For the treatment of wastewater and water containing arsenic, MOFs have been designated as promising materials.

In order to remove arsenic (As) contaminants from aqueous solutions,[271] a metal–organic coordination polymer (Fe–BTC) was synthesized using iron(iii) and 1,3,5-benzene tricarboxylic acid *via* a solvothermal method. This Fe–BTC polymer demonstrated a significantly higher adsorption capacity for As(v) compared to commercial iron oxide powders and nanoparticles (50 nm). The Fe–BTC polymer exhibited an outstanding adsorption capacity for As(v) at 12.3 $mg\ g^{-1}$, six times higher than that of Fe_2O_3 nanoparticles. Comprehensive analyses using FTIR and XPS spectroscopy confirmed significant adsorption before and after As(v) uptake. The arsenic ions were confirmed to adsorb within the Fe–BTC polymer rather than on the surface, indicated by the Fe–O–As IR peak and the presence of As(v) in the XPS spectra.

In order to address the issue caused by secondary pollution resulting from synthetic procedures for magnetic composites,[272] a direct epitaxial synthesis of magnetic UiO-66 was proposed. The composite material was tested for the removal of As(v) and demonstrated an arsenic adsorption capacity of 73.2 $mg\ g^{-1}$. The characterization techniques such as SEM, TEM, and N_2 adsorption–desorption isotherms revealed that the composite has a unique core–shell structure and a high surface area (124.8 $m^3\ g^{-1}$), greater than that of pristine UiO-66 (27.1 $m^3\ g^{-1}$). Furthermore, due to their ease of material recovery after adsorption, magnetically modified UiO-66 composites attracted a lot of attention.[273]

Liu *et al.*[274] described the adsorptive removal of As(v) using heated MIL-100(Fe) to create α-Fe_2O_3 nanoparticles at various temperatures. According to the findings, there was a positive correlation between increasing particle size and rising calcination temperature (*i.e.*, α-Fe_2O_3-350 °C (50 nm), α-Fe_2O_3-550 °C (150 nm), and α-Fe_2O_3-750 °C (200 nm)). For α-Fe_2O_3-350 °C, α-Fe_2O_3-350 °C, α-Fe_2O_3-750 °C, Fe_2O_3-550 °C, and MIL-100(Fe), the corresponding adsorption capacities were 94.9, 74.1, 70.5, 80.5, and 110 $mg\ g^{-1}$ respectively. According to ref. 275, a

comparable investigation revealed that γ-Fe_2O_3 nanoparticles produced through easy thermolysis of MIL-100(Fe) had a 90.6 $mg\ g^{-1}$ adsorption capability for As(v).

Wu *et al.*[276] created a variety of ZIF-8 polymers with varying cetyltrimethylammonium bromide (CTAB):His (L-histidine) molar ratios (such that the polymers were ZIF-8-H_2O, ZIF-8-MeOH, and 1 : 1 H-ZIF-8-11, 1 : 2 H-ZIF-8-12, and 1 : 4 H-ZIF-8-14). ZIF-8-H_2O has the lowest capacity among all of them. ZIF-8 was hierarchically organized and synthesized using a distinct CTAB : His molar ratio with increased CTAB, indicating that this ratio had great adsorptive capabilities. Specifically, HZIF-8-14 exhibited a 30-fold greater adsorptive ability for As(v) (90.9 $mg\ g^{-1}$) in comparison to active carbon (3 $mg\ g^{-1}$). Additionally, it was reported by Liu *et al.*[277] that zeolitic imidazolate frameworks with a variety of morphologies, including cubic, leaf-shaped, and dodecahedral ZIFs, had superior As(iii) adsorption capabilities of more than 100 $mg\ g^{-1}$. By contrast, γ-Fe_2O_3[274] and ZIF-8[278] demonstrated typical As(iii) adsorption capacities of 62.9 and 49.5 $mg\ g^{-1}$, respectively.

The significant presence of the Zn–OH functional group in the ZIF-8 adsorbent produced by Li *et al.*[279] was responsible for its remarkable adsorption capacity of 76.5 $mg\ g^{-1}$. ZIF-8 was functionalized with ethylenediamine by Massoudine *et al.*[280] in order to increase its adsorption capacity, and the result was an adsorption capacity of 83.5 $mg\ g^{-1}$. Another type of traditional MOF, MIL-53(Fe), which was produced *via* a solvothermal technique, was studied by Vu *et al.*[281] An adsorption capacity of 21 $mg\ g^{-1}$ was attained by the adsorbent. MIL-53(Al), MIL-88A, and MIL-88B are other adsorbents exhibiting adsorption capabilities of 106, 145, and 156 $mg\ g^{-1}$, respectively.[282,283] A number of other studies have demonstrated high arsenic adsorption capacities of adsorbents, including indium-based AUBM-1,[284] Co-MOF,[285] Ni-MOF,[286] and MOF-808.[287] With an adsorption capacity of 303 $mg\ g^{-1}$, UiO-66 showed the greatest adsorption capacity among all of them.

3.1.2.2 Lead. Although lead (Pb) is a naturally occurring element in soil, its presence at lower concentrations can be considered an environmental contamination. Lead (Pb(ii)) is widely used in industrial processes like metal plating, painting, smelting, oil refining, and battery manufacturing. Lead poisoning is a serious concern that has been linked to harmful and cancerous effects on human health.[288] Little children are especially vulnerable to the toxicity of lead, which can impact many body systems such as the brain and nervous system. According to Ghorbam *et al.*, Meng *et al.*, and Qiao *et al.*,[289–291] the growing fetus may be exposed to lead toxicity due to the release of lead from bone into the circulation during pregnancy. Higher amounts of lead consumption also primarily cause renal damage, slowed bone growth, mental decline, and neurological illnesses. Pb(ii) content limits have been set by the WHO, European Union, and USEPA, respectively, at 0.01, 0.01, and 0.015 $mg\ L^{-1}$.[292]

Huang *et al.*[239] synthesized a range of Zr-based magnetic MOFs with core–shell amino functionalizations utilizing various functionalization agents. Three MOFs were prepared for

their study: NH$_2$-functionalized Fe$_3$O$_4$@-SiO$_2$@UiO-66-NH$_2$ (MFC-N), urea-functionalized Fe$_3$O$_4$@SiO$_2$@UiO-66-urea (MFC-U), and non-functionalized Fe$_3$O$_4$@SiO$_2$@UiO-66 (MFC-O). When compared to MFC-O, their findings showed that MFC-N and MFC-U had better Pb(II) adsorption capacities. The high adsorption is significantly influenced by the presence of amino groups. A stronger connection between the NH$_2$ groups anchored on MFC-N and Pb(II) ions is indicated by the fact that MFC-N, out of the two amino-functionalized composites, has a higher adsorption capacity of 102 mg g^{-1} towards Pb(II) ions. According to Huang et al.,[293] there has been further breakthrough on the adsorption of Pb(II) using artificial zeolite-imidazolate frameworks, ZIF-67 and ZIF-8. In comparison to certain other porous materials on the market, the MOFs' adsorption capabilities of 1348 and 1119 mg g^{-1}, respectively, were higher.

In a different study, Luo et al.[294] reported a Cr-based MOF functionalized with ethylenediamine (MIL-101) to eliminate Pb(II). In their research, the adsorption isotherms for Pb(II) adsorption on the amine-functionalized MIL-101 were compared to those for the non-functionalized MIL-101. The amine groups' partial obstruction of MIL-101's pores is indicated by the decreased pore volume following functionalization. For the adsorption of lead ions, the amino groups that have been altered on the MOF's exterior surface offer chelating binding sites. Reduced functionalization extent was observed along with a decline in maximum adsorption capabilities, which decreased from 81.09 to 15.78 mg g^{-1}.

Li et al. 2019[295] assessed the efficacy of two amide-based COFs (COF-TP and COF-TE) in the adsorptive removal of Pb(II). Based on their findings, the maximum adsorption capacities of 140 and 185.7 mg g^{-1} were determined for COF-TP and COF-TE, respectively. By acting as an active adsorption site for the metal ions through multi-coordination, the amide group improved the adsorption of Pb(II). A study conducted by Rivera et al.[296] described the adsorption properties of MOF-5 for the removal of Pb(II). 750 and 660 mg g^{-1} of adsorption were observed at pH 4 and 6, respectively, indicating a rising trend in adsorption capacity with decreasing pH.

Yu et al.[297] evaluated the effectiveness of a new metal–organic framework embellished with O$^-$ and N=N groups in order to adsorb Pb(II) from an aqueous solution. Based on their investigation, the maximum Pb(II) adsorption capacity was discovered to be 463.52 mg g^{-1}, and a noteworthy affinity for the metal ion (K_d = 8.88 × 10^6 mL g^{-1}) was observed. The characteristics of the borderline acid were exposed by the densely packed O$^-$ groups and N=N units, and they could interact with the borderline acid Pb(II) extremely quickly. Hasankola et al.[298] reported the utilization of produced Cu-BTC and Zn-BTC MOFs by solvothermal reaction with benzene-1,3,5-tricarboxylic acid as a linker as a versatile adsorbent for the removal of Pb(II). The generated composites showed maximal adsorption capacities of 333 and 312 mg L^{-1}, respectively. When it came to adsorbing Pb(II) ions, the frameworks performed similarly and could sustain the adsorption–desorption cycle three times.

Carbon paste electrodes utilizing MOF-5 for Pb(II) detection were demonstrated by Wang et al.[299] A carbon-MOF-5 paste was created by combining carbon powder with a few drops of ethanol, allowing the fine powder to evaporate and then mixing it with mineral oil in a mortar. To create a MOF-based carbon paste electrode, the paste was placed within a glass tube and sealed with a copper wire. Using 0.1 M acetate buffer at pH 5, various Pb(II) concentrations were used for the differential pulse voltammetry (DPV) experiments. When the concentration of Pb(II) was increased from 1.0 × 10^{-8} to 1.0 × 10^{-6} M, the DPV peak was detected at −0.45 V and moved to lower potentials. This could be because of distinct interactions between the materials at the electrode surface and the thin layer of Pb that was deposited onto the electrode. A Pb(II) removal of 312 mg g^{-1} was accomplished by Zhang et al.[300] using the synthesized HS-mSi@MOF-5 framework, a silica coated thiolated MOF-5 derivative. The pH of the solution had a significant impact on the MOF's performance, with low pH values producing the best results.

Yu et al.[301] described the utilization of a Zn(II) based MOF decorated with O$^-$ groups for Pb(II) adsorption. The material under investigation showed a remarkable adsorption capacity of 616.64 mg g^{-1}, accompanied by 99.27% selectivity towards Pb(II) ions. Their investigation verified that the negatively charged O$^-$ groups interact electrostatically with the Pb(II) ions to play a significant role in this ultrahigh adsorption capacity. Furthermore, the kinetics analysis demonstrated that Pb(II) sorption happened instantly and was attributed to the existence of several porosities that were heavily populated with O$^-$ groups. A developed MOF (MnO$_2$-MOF) was applied to adsorb Pb(II) in a study conducted by Qin et al.[302] The MOF was synthesized using a simple oxidation process, and an equilibrium time of 1 hour was used to determine the metal uptake efficiency. The material revealed an adsorption capacity of 917 mg g^{-1}, which was attained as a result of inner-sphere complexation of hydroxyl groups with the metal ions.

Yin et al.[303] made an effort to modify melamine using a MOF that possesses a structure similar to that of UiO-66 and used it to remove Pb(II). In comparison with the pristine MOF, the modified MOF exhibited high Pb(II) adsorption capacity (205 mg g^{-1}), at pH 6 and 40 °C. When the pH dropped from 6 to 5, a decrease in adsorption capacity of 122.0 mg g^{-1} was noticed. The adsorption capability dropped when the pH value dropped, and the low pH caused the modified MOF to regenerate by desorbing the metal ion. Abbasi et al.[304] created three-dimensional Co-MOF composites for Pb(II) adsorption. The pH of the solution, the concentration of metal ions, and the duration of treatment impacted the adsorbent's effectiveness.

Ricco et al.[305] produced a magnetic framework composite based on aluminum (MFCs) for the removal of Pb(II) ions. By adjusting the 2-amino-1, 4-benzene dicarboxylic acid loadings, they created a series of amino-functionalized MIL-53(Al) MOFs. The magnetic framework composites based on aluminum demonstrated a noteworthy capacity for adsorption, reaching up to 492.4 mg g^{-1}. The investigation also found that as the degree of amino functionalization of the MOF increases, so

does the metal ion absorption capability. Additionally, Sun et al.[306] reported an Fe–BTC/PDA polymer-based MOF composite for Pb(II) adsorption, achieving an adsorption capacity of 394 mg g^{-1}. Additionally, Chakraborty et al.[307] proposed a MOF based on tetracarboxylate and zinc(II), which demonstrated a maximum metal uptake of 71 mg g^{-1}.

3.1.2.3 Chromium. The two primary forms of chromium ions found in the environment are the trivalent (Cr(III)) and the hexavalent (Cr(VI)) species. Compared to Cr(VI), Cr(III) is less hazardous even though it is a target heavy metal pollutant in water. Because of its high toxicity, Cr(VI) has been linked to a number of disorders, including cancer, bronchial asthma, skin allergies, lung and nasal ulcers, and issues with reproduction and development.[308] As per Lv et al.,[286] the highest allowable concentration of chromium in drinking water is 0.1 ppm.

Using a microwave-assisted technique, Sathvika et al.[309] created a *Nitrosomonas*-modified Uio-66 for the adsorption of Cr(VI). Primarily, the functional groups of the modified-MOF and the chromate ions interacted electrostatically to facilitate the uptake of Cr(VI). As for the *Nitrosomonas*-modified Uio-66, it attained 23.69 mg g^{-1}, while the pristine Uio-66 MOF and *Nitrosomonas* sp. showed Langmuir adsorption capabilities of 13.33 and 8.98 mg g^{-1}, respectively. The synergistic increase in the specific surface area and functional groups of the mixed materials is responsible for the improvement in adsorption performance. Saleem et al.[310] reported the usage of modified UiO-66 for the adsorption of Cr(III). The research yielded a resultant optimal adsorption capacity of 67.3 mg g^{-1} for UiO-66-NHC(S)NHMe. Similar to this, post-synthetic alteration improved the performance of both the modified and unmodified UiO-66-NH$_2$ in Cr(III) adsorption compared to the virgin UiO-66.

A cationic Zr-MOF (ZJU-101) was developed by Zhang et al.[311] to remove Cr$_2$O$_7$$^{2-}$. By post-synthetically modifying MOF-867, they were able to create ZJU-101, which is composed of 2, 20-bipyridine-5, 50-dicarboxylate and zirconium metal ions. Tahmasebi et al.[312] reported the synthesis and manufacture of three Zn-based MOFs using a mechanosynthesis approach: TMU-4, TMU-5, and TMU-6. According to their experimental findings, these MOFs showed maximum Cr(III) adsorption capacities of 127, 123, and 118 mg g^{-1}, respectively. In order to successfully extract Cr(VI) from aqueous solutions, Noraee et al.[313] used pristine Uio-66 and ZIF-8. It was shown that ZIF-8 and Uio-66 had maximal adsorption capabilities of 150 and 85.6 mg g^{-1}, respectively. The greater performance of ZIF-8 was attributed to its higher surface area; the potential impact of the MOF's composition was not considered. In contrast, Yang et al.[314] found that the adsorption capability of ZIF-67 was less than that of MMCs (18.0 mg g^{-1}), a MOF composite composed of MIL-100(Fe) and magnetic iron oxide particles.

In order to remove Cr(VI) from water, Aboutorabi et al.[315] created a novel three-dimensional framework based on lead and isonicotinate N-oxide (TMU-30). At a pH of 2–9, the optimum adsorption capacity was 145 mg g^{-1}. The adsorption of metal ions is significantly aided by TMU-30's N-oxide

functional groups. In order to create an electrostatic interaction with chromate species, the positive N-oxide groups can serve as appropriate sites for their adsorption. With R^2 = 0.999, their findings demonstrated that the experimental isotherm data followed the Langmuir isotherm model.

An enhanced powder for Cr(VI) uptake from simulated wastewater was created by Guo et al.[316] using a BUC-17 MOF [Co$_3$(tib)$_2$(H$_2$O)$_{12}$][(SO$_4$)$_3$]. Ion-exchange and electrostatic interactions between the MOF and Cr(VI) were responsible for the 121 mg g^{-1} adsorption capacity that was attained. In order to adsorb chromate (CrO$_4$$^{2-}$), Fei et al.[317] created a MOF by changing the composition ratio of two transition metals, Co(II) and Zn(II). Adsorption capabilities for CrO$_4$$^{2-}$ varied across MOFs with varying Zn(II)/Co(II) ratios; the highest adsorption capacity for Cr(VI) was discovered for Zn$_{0.5}$Co$_{0.5}$-SLUG-35, which was 68.5 mg g^{-1}, where Zn and Co were distributed evenly.

A solvothermal approach was used by Maleki et al.[318] to synthesize copper-benzenetricarboxylate (Cu-BTC), which was then used to remove Cr(VI) from aqueous solution, and the produced MOF showed efficacious Cr(VI) adsorption. The utilization of a rhombic dodecahedral zeolitic imidazolate framework-67 (ZIF-67) based on Co is investigated by Li et al.[319] as a potential method for eliminating Cr(VI) from water. The first step of the Cr(VI) adsorption process was found to be rapid, and the time taken to attain equilibrium increased with the initial concentrations. With a maximum adsorption capacity of 15.4 mg g^{-1} for Cr(VI), their findings indicate that ZIF-67's adsorption tends to follow the Langmuir isotherm model. Another development was the publication of Li et al.[320] on the adsorption of Cr(VI) by a silver-triazolate MOF. A maximum absorption of 38 mg g^{-1} of the cationic MOF was observed during the adsorption of Cr(VI), which was mostly accomplished through anion-exchange.

Recently, Jamshidifard et al.[321] have reported the adsorption of Cr(VI) using a hybrid system consisting of UiO-66-NH$_2$, chitosan, and polyacrylonitrile. The hybrid Uio-66-NH$_2$ was synthesized with the use of microwaves, and it was subsequently added to the chitosan/polyacrylonitrile solution by electrospinning and ultrasonication. For the regeneration of the adsorbent under study, five cautious cycles were performed, and the maximum adsorption capacity was found to be 373 mg g^{-1}. The increased surface area and surface functional groups of the composite allowed the adsorbent to perform exceptionally well.

3.1.2.4 Mercury. Mercury (Hg(II)) is a heavy metal that can be harmful and deadly and can exist in three different forms: elemental, organic, and inorganic salts.[322] However, there are major health risks associated with exposure to both organic and inorganic forms of mercury.[323] Zhao et al.[324] reported that methylmercury is the deadliest form of mercury, causing Minamata disease in individuals from Iraq and Japan who consumed foods contaminated with mercury. Furthermore, because of its affinity for the thiol group of proteins, mercury (Hg) can readily accumulate in the human body and can be

harmful even at low concentrations. This means that exposure to Hg(II) can have an adverse effect on the human nervous system, brain, and kidneys.[325] One of the most often employed technologies is adsorption, and several studies have documented the use of MOF-based adsorbents to extract Hg(II) from water. Although pristine MOFs can be employed for Hg(II) adsorption, most of these applications include functionalizing the MOFs to improve their Hg(II) selectivity.

According to Ke et al.,[326] a thiol functionalized Cu-based MOF (Cu-BTC-DTG), which was created using a coordination-based post-synthetic approach, was able to adsorb Hg(II). The maximal Hg(II) adsorption capacity from water was found to be 714.29 mg g^{-1}. Adsorption sites are provided by the thiol groups that are present on the porous MOF's inner surface. Additionally, they observed that the pristine MOF is unable to adsorb Hg(II) in comparable circumstances. Because of its special ability to bioaccumulate and biomagnify, mercury(II) is a unique metal ion that should be taken seriously at ultra-low concentrations.[327] Another breakthrough involves an experiment conducted by Li et al.[295] in which the NH$_2$-MiL-68(In) MOF is synthesized using a solvothermal technique, and a thiol group (–SH) is added post-synthetically to generate SH-MiL-68(In), which is then utilized to remove Hg(II). A maximum adsorption capacity of 450 mg g^{-1} for Hg(II) was attained. Strong acid–base interactions allowed for the high adsorption to be achieved.

Liang et al.[328] reported the addition of indium(III) sulphide nanoparticles (In$_2$S$_3$) to the MOF (MIL-101) for the adsorption of Hg(II). The procedure entails utilizing In(NO$_3$)$_3$ solution to transform pristine MIL-101 into In^{3+}@MIL-101, which is then transformed into In$_2$S$_3$@MIL-101 via a solid–gas reaction with H$_2$S, and the composite attained 518 mg g^{-1} Hg(II) adsorption capacity. Rudd et al.[329] found that this method yielded a more potent adsorbent in comparison to certain other investigations that prepared a sulfur-functionalized MOF by the traditional solvothermal methodology.

Yang et al.[330] suggested growing Zr-DMBD (Zr-2,5-dimercaptoterephthalic acid-based MOF) on 3D macroporous carbon using a free-standing electrode. Therefore, a vast surface area with 3D macropores is provided by the uniformly decorated MOF nanoarray, facilitating the quick measurement of Hg(II). Zr-DMBD MOFs demonstrated a dramatic response to the addition of 2 μM mercury under optimal pH settings at 0.2 M HAc-NaAc buffer (pH – 6.0), and the electrochemical response at the modified electrode is found to be six times higher than 3D kenaf stem-derived carbon.

A photo-assisted post-synthetic modification technique was examined by Yin et al.[331] To evaluate the adsorption of Hg(II) from aqueous solutions, a pyrimidine–thione fragment was introduced onto ZIF-90. During synthesis, pristine ZIF-90, thioureas, and either tetrahydropyran (THP) or tetrahydrofuran (THF) under UV radiation underwent a multicomponent reaction. ZIF-90-THP and ZIF-90-THF exhibited the highest levels of Hg(II) adsorption among the functionalized materials, reaching 596 and 403 mg g^{-1}, respectively. The pristine ZIF-90 demonstrated a lower adsorption capacity of only 47 mg g^{-1}.

Li et al.[332] reported using generated ZrO$_x$, ZrO$_{xy}$Phos, and ZrSulf from MOFs for the adsorption of Hg(II) via a ligand extraction approach. In the ligand extraction procedure, inorganic moieties were substituted for the pure MOF's organic ligand. Here, the inorganic moieties that were utilized to make ZrO$_x$, ZrO$_{xy}$Phos, and ZrSulf were NaOH, Na$_3$PO$_4$ and Na$_2$S·9H$_2$O, respectively. ZrSulf had the highest adsorption capability of 824 mg g^{-1}, followed by ZrO$_{xy}$Phos and ZrO$_x$ at 663 and 485 mg g^{-1}, respectively. In comparison to the pristine UiO-66-50Benz, which has an adsorption capacity of 363 mg g^{-1}, both demonstrated a strong removal capability.

3.1.2.5 Copper. Living organisms need trace elements like copper ions (Cu(II)) at low concentrations.[333] However, at certain environmental concentrations, it becomes a contaminant to the environment and public health.[334] Copper is released into the environment by several industries, including metal cleaning and plating, paints and pigments, mining, smelting, petroleum refinery, brass rinsing, paper board, wood pulp, and printed circuit boards. The environment frequently contains significant amounts of copper because of its widespread industrial use.[335]

Numerous health issues, including neuro/hepatodegenerative diseases like Alzheimer's and Wilson's diseases, have been connected to the use of Cu(II).[336] Furthermore, a high consumption of Cu(II) will raise blood pressure, cause damage to the kidneys and liver, and increase respiration rates.[337] Strict recommendations have been made regarding the content of Cu(II) in drinking water in order to safeguard human health. For instance, the United States Environmental Protection Agency (USEPA) sets the maximum limit of Cu(II) in drinking water at 1 mg L^{-1},[338] whereas the World Health Organization (WHO) set it at 2 mg L^{-1}.[339]

Ghaedi et al.[340] investigated the usage of a Cd-based MOF (Cd-MOF-74) as an efficient adsorbent for the removal of Cu(II) from aqueous solutions. The optimum adsorption capacity of 435 mg g^{-1} for Cu(II) is exhibited by the produced MOF. While retaining its effectiveness, three conservative cycles were also noted throughout the regeneration research. To create the Cd-TPA template, terephthalate, dimethylformamide, and Cd(CH$_3$COO)$_2$·2H$_2$O were combined in a room temperature ultrasonic driven reaction. Wang et al.[341] reported the use of a ceramic membrane and a Zr-MOF functionalized with amino groups to remove Cu(II). Based on their research, a comparison was made between the adsorptive capacities of a ceramic membrane and a pure Zr-MOF. Cu(II) adsorption capacities of 988 and 60 mg g^{-1} were attained for the Zr-MOF/ceramic membrane and pristine Zr-MOF, respectively. The stability of the MOF is still a problem, despite the concerning improvement in the combined Zr-MOF/ceramic membrane adsorption capability.

Bakhtiari and Azizian[342] examined and documented the adsorption of Cu(II) ions using a nanoporous zinc-based MOF. Results obtained from their experimental study showed a maximum adsorption capacity of 290 mg g^{-1} and a BET surface area of 888.5 m^2 g^{-1}. They also clarified that non-uniform adsorption of Cu(II) ions and slow kinetics are caused by the

heterogeneity of the MOF surface. Graphene oxide was integrated into a pristine 2-aminoterephthalic acid-ZnO_4 MOF (IRMOF-3) in an experimental work conducted by Rao et al.[343] The objective of the work was to remove Cu(II) from an aqueous solution. The addition of graphene oxide increased the pristine IRMOF-3's adsorption capacity and selectivity; the maximum adsorption capacity reached 254 mg g^{-1}. Zheng et al.[344] used a solvothermal technique to create a Cd-based MOF (Cd-MOF-74) and evaluated its efficacy as an adsorbent to remove Cu(II) from solutions. An adsorption capacity of 190 mg g^{-1} was reached by the produced MOF. Mohmoodi et al.[345] presented an example of how a magnetic bio nanocomposite consisting of an eggshell membrane-zeolitic imidazolate framework (ZIF) can be used to extract Cu(II) from an aqueous medium. The ZIF-67 MOF was effectively stabilized on the magnetic eggshell membrane surface functionalized with iron oxide, resulting in the formation of the ZIF-67@Fe_3O_4@ESM composite. ZIF-67@ Fe_3O_4@ESM has a maximum adsorption capacity of 344.82 mg g^{-1}, which means that it may be effectively employed to remove Cu(II) ions. A significant contribution to the high Cu(II) can be attributed to the novel adsorbent's high surface area of 1263.9 m^2 g^{-1}.

3.1.2.6 Cadmium. Even in low amounts, cadmium (Cd) is one of the most hazardous non-essential heavy metals found in the environment. The exposure to Cd at low concentration levels is extremely harmful to the kidneys and can result in renal failure.[346] Many industries, for example, electroplating, waste discharged nickel runoff, phosphate fertilizer, cadmium-nickel batteries, mining, pigments, stabilizers, alloys, petroleum refining, welding, and the pulp and paper sectors, release cadmium into the environment.[347] Despite being present in the environment in small amounts, Cd is known to be bioaccumulative and to negatively impact a variety of creatures.[348] When it comes to non-essential heavy metals in the environment, cadmium is among the most dangerous even in little amounts. The USEPA has set a maximum contamination level (MCL) of 0.005 mg L^{-1} for cadmium in drinking water.[349]

Wang et al.[350] performed an experiment in order to determine Cd concentration at ultra-trace levels and also to improve the conductivity of a MOF. They did this by dispersing UiO-66-NH_2 in HCl and then adding aniline and APS, which self-polymerizes to produce PANI loaded on the UiO-66-NH_2 matrix. The deposition potential response indicated a linear connection between current and Cd content across the range of 0.5 to 600 mg L^{-1}, and the detection limit was determined to be 0.3 mg L^{-1}. A deposition potential of −1.2 V, an accumulation period of 120 s, and an optimum pH of 5.0 were selected. In a separate study, Roushani et al.[351] reported the adsorption of Cd(II) on a TMU-16-NH_2MOF. It was possible to get the maximal adsorption capacity of 126.6 mg g^{-1}.

Wang et al.[352] conducted an experiment to test the viability of removing Cd(II) from aqueous solution using the $Cu_3(BTC)_2$-SO_3H framework, which was created by oxidizing $Cu_3(BTC)_2$. At a pH of 6, the maximum adsorption capacity was attained. Because SO_3H has numerous binding sites and coordination modes, the sulfonic groups of the MOF and Cd(II) ions

Table 2 Summary of reported results for heavy metal removal from aqueous solution and wastewater by MOF-based adsorbents

Adsorbate	Adsorbent	Adsorption capacity (mg g^{-1})	Time (min)	Ref.
As	NH$_2$–MIL-88(Fe)	125	60	282
	UiO-66	303	2880	268
	Fe–BTC	12.3	10	271
	Fe$_3$O$_4$@UiO-66	73.2	100	354
	UiO-66-(SH)$_2$	40	1440	355
	γ-Fe$_2$O$_3$@CTF-1	198	1440	356
	Zn-MOF-74	As(V): 325	4	357
		As(III): 211		
Pb	MIL-101(Fe)/GO	128.6	15	358
	Fe$_3$O$_4$–NHSO$_3$H@HKUST-1	384.6	90	359
	Cu(TCPBDA)	300	60	360
	UiO-66-NH$_2$@CA	89.40	4080	361
	Amide-based COF	185.7	1440	362
	PAN/chitosan/UiO-66-NH$_2$	115	60	321
	UiO-66-RSA	189.8	180	363
	Fe–BTC/PDA	394	1440	306
	MOF-2(Cd)	434.78	180	340
	Cu-MOFs/Fe$_3$O$_4$	219	60	364
Cr	ZIF-8 (150)	150	350	313
	Cu-BTC	48	—	318
	UiO-66	85.6	350	313
	Nitrosomonas modified-UiO-66	921	180	309
	IMF-Cr-MOF	321	50	365
	PAN/chitosan/UiO-66-NH$_2$	99.5	60	321
	[Co$_3$(tib)$_2$(H$_2$O)$_{12}$](SO$_4$)$_3$(BUC-17)	121	480	316
	HKUST-1	24.20	60	366
Hg	γ-Fe$_2$O$_3$@CTF-1	165.8	1440	356
	SH-MIL-68(In)	450	120	295
	UiO-66-50Benz	824	120	367
	In$_2$S$_3$@MIL-101	518.2	60	328
	ZIF-90-THP	596	10	331
	Fe–BTC/PDA	1634	1440	306
Cu	MOF-2(Cd)	769.23	180	340
	[[Zn$_3$L$_3$(H$_2$O)$_6$]][(Na)(NO$_3$)]	379.13	—	368
	Cd-MOF-74	189.5	10	344
	IRMOF-3/GO	254.14	480	343
Cd	γ-CD MOF-NPC	140.85	60	369
	PAN/chitosan/UiO-66-NH$_2$	107.6	60	321

exhibited a chelation reaction during the adsorption process, which increased the selectivity for Cd(II).[352] The PCN-100 MOF was presented by Fang et al. (2010) and was synthesized from TATAB ([[Zn$_4$O(C$_{24}$H$_{15}$N$_6$O$_6$)$_2$(H$_2$O)$_2$]·6H$_2$O·DMF]$_n$ (1) using Zn$_4$O(CO$_2$)$_6$ secondary building units and 4,4,4″-s-triazine-1,3,5-triyltri-p aminobenzoate) linkers. It was discovered that the MOF used linkers to engage in chelating coordination mode interactions with metal ions. Rahimi and Mohaghegh[353] also assessed the Cd(II) adsorption potential of a magnetic Cu-terephthalate MOF. The maximal adsorption capacity of 100 mg g^{-1} is achieved by the chemical adsorption technique. COOH groups on the MOF significantly improved the adsorption performance. Cd(II) adsorption by AMOF-1 was reported by Chakraborty.[307] Utilizing Zn and tetracarboxylate linkers as its foundation, the MOF attained an adsorption capacity of 41 mg g^{-1} (Table 2).

In summary, metal–organic frameworks and their composites exhibit favorable adsorptive features for heavy metal removal. Functionalization of such metal–organic frameworks can increase their environmental acceptability, strengthen their bonds with heavy metals, decrease coagulation and enhance the adsorption efficiency, resulting in increased removal of heavy metals from wastewater and aqueous solutions. Moreover, most adsorption kinetics can be illustrated by the pseudo-second-order model and the adsorption equilibrium is well described by the Langmuir isotherm model. Comparative results of heavy metal removal utilizing metal–organic frameworks and other adsorbents are summarized, clearly indicating the relatively higher removal capacities of MOFs.

3.1.3 Adsorption of toxic gases. Actually, a significant portion of MOFs have demonstrated adsorption behavior for gas molecules, and a smaller subset of these MOFs has also been examined for the combination of gases through the use of techniques like gas chromatography or breakthrough tests. Additionally, it has been demonstrated that MOFs' selective adsorption performance may be adjusted by altering their molecular architectures and pore characteristics. The majority of these gases are waste products of industrial operations that are discharged into the environment; in certain instances, individuals are even exposed to them directly. Effective capture of these dangerous gases is extremely important for the protection of the environment. According to recent findings, MOFs are superior to other materials when it comes to the high adsorption of poisonous gases like CO_2, CO, NO_2, and H_2S.[370]

According to Yazaydin et al.,[371] the carbon dioxide adsorption capacities of Ni/DOBDC and Mg/DOBDC, which are also referred to as Ni-MOF-74 and Mg-MOF-74 or CPO-27-Ni and CPO-27-Mg, are 5.95 mol kg^{-1} and 4.07 mol kg^{-1}, respectively, at 0.1 atm and 298 K. The authors observed that MOFs with a high density of open metal sites, such as Ni/DOBDC and Mg/DOBDC, are attractive candidates for CO_2 extraction from gas samples instead of MOFs with high surface area or free volume. At 0.1 atm and 25 °C, they found that Ni/DOBDC has a greater CO_2 adsorption capacity than 5 A zeolites and NaX. The possibility of using composites of MOFs (MOF-5, Cu-BTC, or MIL-100(Fe)) and a graphitic substance (graphite or graphite oxide, GO) as adsorbents for the removal of NH_3, H_2S and NO_2 in ambient settings was investigated by Petit and Bandosz.[372] In order to create composites with unique characteristics, a new pore space was created at the interface between the carbon layers and the MOF units as a result of the coordination between the oxygen groups of GO and the open metal sites of porous MOFs. When a GO/Cu-BTC composite was used instead of virgin Cu-BTC, there were increases in the adsorption capacity of over 12% for NH_3, 50% for H_2S, and 4% for NO_2. The creation of additional porosity in the interface, where dispersive forces were strongest, provided an explanation for the increased adsorption capabilities for the dangerous gases. Ebrahim and Bandosz[373] conducted an experiment showing that after grafting with melamine (melamine@UiO-66(Zr)-COOH and melamine@UiO-67(Zr)-COOH), respectively, the adsorption of NO_2 gas onto UiO-66(Zr)-COOH and UiO-67(Zr)-COOH was dropped from 40–73 and 79–118 g kg^{-1} to 3–10 and 41–93 g kg^{-1}.

The study conducted by Choi et al.[374] involved the synthesis of a three-dimensional (3D) ABDC MOF (In) through the interaction of a ditopic azobenzene-4,4′-dicarboxylic acid (H_2ABDC) and salt with 1-ethyl-3-methylimidazolium tetrafluoroborate ([EMIM][BF_4]) as an ionic liquid. When the 3D ABDC (In) MOF was used for CO_2 gas adsorption, the pre-adsorbed CO_2 molecules improved the subsequent adsorption of freshly introduced CO_2 molecules. The amount of CO_2 adsorbed by the ABDC (In) MOF was 81.3 cm^3 g^{-1} (3.63 mM g^{-1}). A fluorinated metal–organic framework (FMOF-2, derived from 2,2′-bis(4-carboxyphenyl)hexafluoropropane and zinc nitrate hexahydrate) was investigated by Fernandez et al.[375] for the potential application in the elimination of harmful acidic gases. The adsorption of SO_2 and H_2S on FMOF-2 was remarkably stable. The weight capacities of SO_2 and H_2S with FMOF-2 at room temperature and 1 bar were calculated to be 14.0% and 8.3%, appropriately.

Glover et al.[376] investigated the adsorption of various hazardous gases, such as NH_3, $CNCl$, SO_2, and octane vapor, using M-CPO-27 (M Zn, Co, Ni, or Mg) in both dry and humid settings. The results of this ground-breaking experiment showed that all of these MOFs with open metal sites can only effectively adsorb the hazardous gases under study when the environment is dry. In humid environments, on the other hand, the adsorption capacity is significantly decreased as water begins to adsorb competitively. With regard to NH_3 gas, adsorption of ammonia occurred under both humid and dry circumstances, with little discernible drop in adsorption capability. Overall, it can be said that water vapor hinders different gases from adhering to CPO-27 type materials. A study conducted by Petit et al.[377] found that the adsorption capacity of the Cu-BTC composite increased from 92 to 200 g H_2S per kg in moist settings and from 110 to 135 g NO_2 per kg under dry conditions as a result of graphite oxide (GO) grafting. However, as indicated by Petit and Bandosz,[372] the adsorption of H_2S and NO_2 onto the GO@Cu-BTC composite under ambient circumstances resulted in a 50% and 12% increase in the adsorption capacity, respectively.

Comparative research on MOFs that exhibit stability and ease of regeneration upon H_2S sorption via pressure swing adsorption mechanisms was conducted by Hamon et al.[378] Low pressure causes the pores of MIL-53s(Al, Cr) to close due to the strong interaction between the polar H_2S molecules and μ_2-OH of the inorganic chain. Remarkably, as pressure increased, the strong $H_2S\cdots HO$ (on the metal site of MOFs) contacts broke, reopening the pores. This led to the filling of all the pores through weak host–guest interactions, resulting in steps in the adsorption isotherm. The initial and subsequent phases commenced at 4.5, 118 kPa and 9.0, 210 kPa for MIL-53(Al) and MIL-53(Cr), correspondingly. At high pressure (1.6 MPa), the maximum H_2S sorption capacities were reached at 13.12 and 11.77 mmol g^{-1} for MIL-53(Al) and MIL-53(Cr), respectively. The adsorption capacities of MIL-47 and MIL-53s(Al, Cr) at high pressure were comparable, indicating that the pores in MIL-53s reopened at high pressure. Additionally,

the large pores of MIL-100(Cr) and MIL-101(Cr) showed type-I shaped adsorption isotherms, indicating significant uptake of H_2S by the authors nevertheless, and the adsorption seemed to be irreversible. For MIL-100(Cr) and MIL-101(Cr), the optimum adsorbed quantities at 2 MPa were 16.7 and 38.4 mmol g^{-1}, respectively. The irreversible adsorption phenomenon was explained by the possibility of either the framework being partially destroyed or experiencing significant interactions with the H_2S molecules. Furthermore, in a separate research, it was also revealed by Hamon et al.[379] that the adsorption of H_2S primarily takes place via the hydrogen bond formation between the H_2S molecules and the μ_2-O atom of the V=O···V moiety in MIL-47, wherein H_2S functions as a hydrogen donor. It was also proposed that acidic H_2S interacts with additional basic centers in MIL-47, such as the π electrons of the benzene ring and the oxygens of the carboxylate group.

Additional noteworthy instances are the flexible MOFs, where the opening of the pores is contingent upon the pressure at which the adsorbed guest molecules occur. Kitaura et al.[380] originally noticed this phenomenon in Cu(dhbc)$_2$(bipy) (dhbc = 2,5-dihydroxybenzoate; bipy = 4,4'-bipyridine). In a different study, Dathe et al.[381] tested the efficacy of Ba(CH$_3$COO)$_2$ (or Ba(NO$_3$)$_2$) and BaCl$_2$-impregnated Cu-BTC in adsorbing SO_2. Little barium salt microcrystals were produced by impregnation in the pores of Cu-BTC, although only BaCl$_2$ showed signs of partially destroying the host structure. Based on the concentration of Ba^{2+}, the authors noted that at high temperatures, SO_2 uptake exceeded the stoichiometric capacity. Thus, chemical interaction between the metal cations (from the MOF) and SO_2 is responsible for the excess SO_2 adsorption and for the synthesis of Cu-sulfates at the end. Cu-BTC responded well as a host material to hold widely distributed barium salts at low temperatures. Conversely, Cu-BTC broke down at high temperatures, resulting in isolated Cu species that served as SO_x storage locations before Cu-sulfates were eventually formed.

Furthermore, Garcia-Ricard and Hernandez-Maidonado[382] assessed the dynamics of CO_2 adsorption on three distinct forms of Cu$_2$(pzdc)$_2$(bipy) (pzdc = pyrazine-2,3-dicarboxylate) pretreated at varying temperatures, while Zhao et al.[383] investigated CO_2 diffusion in cubic MOF-5 crystals and found that the process is activated and that CO_2 loading has very little effect on the rate of diffusion. Gravimetric adsorption of NO on Cu-BTC's open metal sites at 196 K (1 bar) was reported by Xiao et al.[384] The results showed that around 9 mmol NO was adsorbed over 1 g of Cu-BTC, which was much more than any other porous solid that had been reported for the adsorption of NO. MOF-74(Mg) demonstrated a much greater CO_2 adsorption of 5.3 mM g^{-1} when exposed to 40 °C and 150 mbar.[385] Lower adsorption capability (2.3 mM g^{-1}) at 40 C and 150 mbar was obtained by using MIL-101(Cr)-SO$_3$H-TAEA [tris(2-aminoethyl)amine], which was further lowered to 1.1 mM g^{-1} by lowering the temperature and pressure to 20 C and 0.4 mbar, respectively.[386] Following cationic exchange, the adsorption capacity of CO_2 onto the 3D anionic MOF (Ni) was greatly enhanced.[387]

A Cu-BTC framework with 4 weight percent water molecules coordinated to the open metal sites of the framework showed remarkable improvements in CO_2 adsorption and selectivity over N_2 and CH_4, as reported by Yazaydin et al.[388] The quadrupole moment of CO_2 interacts with the sorbent's electric field gradient, which is enhanced when water fills the copper open metal site, and it was proposed that these interactions account for the majority of the boost in CO_2 adsorption. The impact of the metal center on the CO_2 adsorption selectivity and adsorption capacity was demonstrated by Dietzel et al.[389] using a set of isostructural MOFs M-CPO-27 (M: Ni, Co, Zn, Mg, and Mn). The CO_2 uptake values for CPO-27(Ni) and CPO-27(Mg) were reported to be 51 weight percent and 63 weight percent, respectively, at 298 K and high pressure (50 bar). According to Caskey et al.,[390] using CPO-27(Co) and CPO-27(Mg), CO_2 uptake values were 30.6 and 35.2 weight percent at 1 atm, respectively.

Furukawa et al.[391] demonstrated a remarkable CO_2 uptake using MOFs that have an ultrahigh surface area. MOF-210 [Zn$_4$O(BTE)$_{4/3}$(BPDC)] comprises two components: BPDC (biphenyl-4,4'-terephthalate) and BTE (benzene-1,3,5-triyl-tris(ethyne-2,1-diyl)). At 50 bar, MOF-200 [Zn$_4$O(BBC)$_2$(H$_2$O)$_3$ in which BBC: 4,4',4''-(benzene-1,3,5-triyl-tris(benzene-4,1-diyl))tribenzoate] with BET surface areas of 6240 and 4530 m^2 g^{-1}, respectively, were able to absorb 2400 mg g^{-1} CO_2, surpassing the uptake values of other highly porous MOFs such as MOF-177, MIL-101(Cr)c, and so forth.[392] Another development was the discovery by Karra and Waiton[393] that Cu-BTC was a highly selective CO adsorbent at 298 K, as demonstrated by a molecular simulation analysis. The partial charges of CUS of Cu-BTC (Cu^{2+} sites) and the CO dipole were said to interact electrostatically, which dominated the adsorptive performance.

Britt et al.[394] provided evidence regarding the potential utility of six MOFs, the Zn$_4$O(CO$_2$)$_6$ cluster linked by terephthalate (MOF-5), 2-amino terephthalate (IRMOF-3), benzene-1,3,5-tris(4-benzoate) (MOF-177), diacetylene-1,4-bis(4-benzoic acid) (IRMOF-62), Zn$_2$O$_2$(CO$_2$)$_2$ chains linked by 2,5-dihydroxy-terephthalate (CPO-27), and Cu-BTC, in the adsorption and separation of several hazardous gases or vapors, such as SO_2, chlorine, NH_3, benzene, ethylene oxide, and tetrahydro-thiophene. The outcomes were compared with BPL carbon. Numerous elements have been demonstrated to be significant in influencing the dynamic adsorption performance of these MOFs, including the open metal sites of Cu-BTC or CPO-27 (also known as M$_2$(dobdc)(H$_2$O)$_2$; H$_4$dobdc = 2,5-dihydroxyterephthalic acid) and the active adsorption site with specific functional groups (like NH_2 in IRMOF-3). The capacity of CPO-27 was six times greater than that of the BPL carbon and it outperformed the other MOFs in terms of SO_2 adsorption capacity. The presence of both the potentially reactive oxo group in CPO-27 and a highly reactive 5-coordinate zinc species is the cause of this advantageous adsorption. However, because Cl_2 does not naturally function as a ligand, Cu-BTC had a high efficiency that was on par with or higher than that of BPL carbon for all of the gases that were tested. Regarding NH_3, the adsorptive performance of IRMOF-3 is significantly enhanced by the presence of NH_2 in comparison to the virgin IRMOF-1 or

MOF-5. Due to the NH_3's propensity to form hydrogen bonds, IRMOF-3 was able to adsorb about 71 times as much NH_3 prior to breakthrough than BPL carbon.

In summary metal–organic frameworks (MOFs) are a novel class of adaptable porous materials with enormous surface areas, mechanical flexibility, programmable topologies, and tunable pore size and thickness. Adsorbents based on molecularly oxidized fuel (MOFs) are very suitable for absorbing gases, facilitating the assimilation of gaseous fuels and the elimination of greenhouse gases. A rigorous assessment was conducted on the adsorption of gaseous molecules utilizing MOFs. MOFs have potential as economical, moisture-stable adsorbents for natural gas.

3.1.4 Adsorption of antibiotics. In order to both prevent and treat major infections in living things, antibiotics are necessary. It is estimated that urine and feces excrete between 5 and 90 percent of the active antibiotic components that are eaten. According to Monahan et al.,[395] these substances pollute groundwater and surface water, encouraging the microbial resistance of natural water bodies. They are categorized as J01 medications for systemic antibacterial usage in accordance with the WHO's therapeutic chemical categorization.[396] Antibiotic excretion, however, can contaminate the environment and water sources, posing a threat to the world's ecology. Antibiotic overuse and drug resistance are the main causes of this pollution, which is becoming a global problem.[397]

Various methods are used to eliminate antibiotics, including membrane filtration, biological treatment, adsorption,[398] electrochemical treatment,[399] advanced oxidation technology,[400] and photodegradation.[401] Adsorption and photodegradation are particularly favored for their high efficacy, simplicity, low cost, sustainability, and versatility.[402] Nevertheless, there are inherent restrictions on these techniques that make them less effective and difficult to use widely. These restrictions include things like the efficiency of removal, the complexity of function, and the production of byproducts that may cause cancer and mutations. MOFs' huge specific surface area, well-organized pores, and structural plasticity allow them to tackle these issues.

For the purpose of adsorbing nitrofuran antibiotics from wastewater, Lei et al.[403] created a stable Cd-MOF (MOF-1) and created a composite with macroporous, elastic, and inexpensive melamine foam (MOF-1@MF) via a one-pot solvothermal synthesis. Strong hydrogen bonding between MOF-1's urea groups and the antibiotics' $–NO_2$ groups was made possible. A chemically resistant, hydrophobic Zn-based MOF-1 ([{Zn(hfdba)(L1)}·DMF]$_n$) and its membrane have been recently created by Mukherjee et al.[404] for the detection of dangerous nitro-explosives and nitrofuran antibiotics, as well as for the adsorption of TNP from aqueous solutions. This MOF-1 exhibits outstanding ultralow sensitivity for precisely detecting TNP and NZF in environmental samples, thanks to its evenly functionalized lozenge-shaped pores.

Tetracycline adsorption from water was studied by Xia et al.[405] utilizing three Zr-MOFs: MOF-525, NU-1000, and

UiO-66. While NU-1000 had a BET surface area of 1487 m^2 g^{-1} with a type-IV adsorption isotherm, UiO-66 and MOF-525 had BET surface values of 1249 and 2224 m^2 g^{-1} with type-I adsorption isotherms. They were all capable of showing maximum adsorption capacities of 145, 356, and 807 mg g^{-1}. According to Yang et al.,[406] doping Mn onto UiO-66 increased its surface area and active centers, which improved the material's capacity to remove tetracycline by 4.9 times when compared to unadulterated UiO-66. Because of mesopores, Zhang et al.[407] produced porous UiO-66 under reflux circumstances, which resulted in a 430% increase in tetracycline adsorption efficacy.

CuCo/MIL-101, a bimetallic doped material, for tetracycline adsorption was described by Jin et al.[408] They proposed that metal doping modifies surface electrical characteristics and strengthens chemical interactions, which impact antibiotics' electrostatic interactions. Zn-MIL-53(Fe) was used by Xiong et al.[409] to create magnetic carbon-aFe/Fe$_3$C under N_2 for tetracycline adsorption. According to Sun et al.,[410] incorporation of additional functional groups made possible by graphene oxide (GO) allowed UiO-66-(OH)$_2$/GO to greatly boost adsorption efficiency when compared to UiO-66-(OH)$_2$ alone. Tetracycline adsorption was further improved by Wang et al.[411] by in situ growth of UiO-66-(COOH)$_2$ on GO. Hydrogel–GO was used as a substrate for ZIF-67 growth by Kong et al.,[412] which reduced particle aggregation and increased adsorption efficiency.

In order to activate peroxymonosulfate for the oxidative degradation of oxytetracycline (OTC), Mao et al.[413] developed Co@C-600, a highly efficient magnetic carbon generated from a Co-based MOF. Electron paramagnetic resonance experiments verified that they used both radical (OH and SO_4^-) and non-radical pathways to achieve over 89% degradation of OTC in under 15 minutes. Tetracycline and norfloxacin were removed from an Fe MOF by both single and competitive adsorption processes, according to Zhou et al.[414] When comparing the competing system to the single adsorption, they discovered lower tetracycline and norfloxacin adsorption efficiency. The substance showed signs of durability and reusability.

Wu et al.[415] examined the use of a composite of Fe_3O_4 with HKUST-1, which is well-known for having a high surface area and accessible open metal sites (OMSs), to produce a water-stable magnetic composite (Fe_3O_4@HKUST-1). They investigated how well it eliminated medications called fluoroquinolones. Fe_3O_4 and other magnetic materials are highly valued for their ease of regeneration and separation in the presence of an external magnetic field. The protective effect of Fe_3O_4 nanoparticles on the Cu(II) metal sites, which thwarts breakdown by water molecules, is responsible for the water stability of these composites. Furthermore, Fe_3O_4@Cys@MIL125-NH$_2$ was created by Lian et al.[416] for the elimination of fluoroquinolones and could be retrieved using a magnet. MIL-101(Cr)–HSO$_3$ was created by Guo et al.[417] by functionalizing terephthalic acid with –HSO$_3$ in order to improve electrostatic interactions with fluoroquinolones. In order to remove levofloxacin from water, Chaturvedi et al.[418] produced Fe-based MOFs (MIL-100(Fe)) using a solid method. They achieved great adsorption efficiency

(87.34 mg g^{-1}), principally through electrostatic interactions and hydrogen bonding mechanisms.

The best removal efficiency for ciprofloxacin and tetracycline was determined by Kim et al.[419] utilizing a batch model to manufacture a rGO/alginate coated Al-based MOF adsorbent. At an operating temperature of 40 °C, the adsorbent exhibited the highest removal capacity of around 40.76 mg g^{-1} for ciprofloxacin and 43.76 mg g^{-1} for tetracycline at pH 7. The contact period was approximately 12 hours. In order to study ciprofloxacin adsorption behavior with various structural features, Li et al.[420] synthesized nanoporous carbon (NPC) using ZIF-8 derived carbonization. Yuan et al.[421] looked into the use of Konjac glucomannan (KGM) as a ZIF-8 carrier. KGM was chosen because it is inexpensive and biodegradable, which enables the formation of floating aerogels following lyophilization. According to the experimental findings, the aerogel could be effectively reused and demonstrated good adsorption performance for ciprofloxacin.

According to Moradi et al.,[422] the magnetic composite Fe$_3$O$_4$ MIL-100(Fe) and MOF-235(Fe) was utilized to adsorb ciprofloxacin. Additionally, Wu et al.[415] added Fe$_3$O$_4$ to HKUST-1 preparation to create a magnetic material (Fe$_3$O$_4$/HKUST-1) that can be recycled ten times for ciprofloxacin adsorption. Bayazit et al.[423] used a sedimentation process in another advancement. In order to create composite materials with excellent ciprofloxacin adsorption capabilities, he added MIL-101(Cr) during the precipitation method of creating Fe$_3$O$_4$ by allowing Fe$_3$O$_4$ to be deposited on the surface of MIL-101(Cr).

To effectively remove cephalexin (CFX) from wastewater, Zhao et al.[424] also synthesized another very stable Zr MOF PCN-777. The MOF in question demonstrated improved porosity, larger pore size, high specific surface area (2004 m^2 g^{-1}), and remarkable water stability. A mesoporous cage measuring 32 Å (a pore volume of 2.7 cm^3 g^{-1}), greater than cephalexin (12 Å × 7 Å), is present in PCN-777, which exhibits exceptional water stability and a high BET surface area of 2004 m^2 g^{-1}. PCN-777 demonstrated a maximum adsorption efficiency of 442.48 mg g^{-1} CFX at 303 K, higher than those of other types of adsorbents, such as activated carbon (AC), natural zeolites, SBA-15, etc. These results demonstrate PCN 777's appropriateness and potential use as an effective adsorbent for removing antibiotics from wastewater, as well as its ability to serve as a model for the synthesis and design of other adsorbents.

The effectiveness of the adsorptive removal of antibiotics from water was investigated by Gao et al.[425] in relation to the breathing effect or framework flexibility. For the adsorptive removal of sulfamethoxazole (SMZ, a sulphonamide antibiotic often used to treat urinary tract infections) from aqueous solution, three isomorphous flexible MIL-53 adsorbents, namely MIL-53(Cr), MIL-53(Al), and MIL-53(Fe), were selected. Due to its flexibility, MIL-53 can take on several shapes, such as the narrow pore (NP), large pore (LP), and intermediate pore (INP) forms, depending on which metal ions are chosen. In order to achieve quick and selective adsorption of sulfamethoxazole from H$_2$O solutions, Cheng et al.[426] created a surface molecularly imprinted polymer on a MOF (MIP-IL@UIO-66).

The MOF discussed above demonstrated a maximum adsorption efficiency of 284.66 mg g^{-1} and reached adsorption equilibrium in 10 minutes. With an adsorption effectiveness of over 92% even after five cycles of reusability, the adsorbent showed good stability and reusability. Sulfamethoxazole and other antibiotics may be more effectively removed from water, thanks to the synthesized MOF's superior adsorption efficiency, selectivity, quick adsorption rate, and reusability, as demonstrated in the study.

Azhar et al.[427] employed HKUST-1 in conjunction with open metal sites (OMS) to remove sulfachloropyridazine (SCP) from wastewater by adsorptive means. The pore volume (0.78 cm^3 g^{-1}) and pore size (1.7 nm) of HKUST-1 were both greater than those of SCP molecules (0.81 × 0.87 × 0.65 nm), suggesting that SCP would preferentially adsorb into the pores of HKUST-1. The BET surface area of HKUST-1 was estimated to be 1700 m^2 g^{-1}. At 298 K, HKUST-1's adsorption capacity of 384 mg g^{-1} toward SCP was observed, accompanied by a high rate of adsorption that was nearly finished in 15 minutes. An experiment was conducted by Zhao et al.[428] to remove the antibiotic chloramphenicol from wastewater using a new MOF-based adsorbent known as PCN-222. This MOF-based material quickly reached adsorption equilibrium and showed improved adsorption efficiency. The remarkable ability of PCN-222 to eliminate substances was attributed to its unique pore structure, H-bonding, and electrostatic interactions. The study's conclusions suggest that these materials might be used to successfully remove antibiotics like chloramphenicol from aquatic ecosystems. Yang et al.[429] created a porous magnetic derivative of MIL-101(Fe–Co) and used it in a related investigation to activate peroxymonosulfate, which broke down chloramphenicol in solution. After 120 minutes, the antibiotic had completely degraded at a catalyst concentration of 0.1 g L^{-1} (pH = 8.2). The principal oxidative species responsible for the breakdown of chloramphenicol have been identified as hydroxyl and sulfate radicals.

In order to recover 5-nitroimidazole antibiotics using LC-MS analysis, Lu et al.[430] employed highly porous MIL-101(Cr) as an adsorbent for the first time. They functionalized the framework with –NH$_2$ moieties and grafted urea or melamine into the OMS to create urea–MIL-101(Cr) and melamine–MIL-101(Cr) with BET surface areas of 1970 m^2 g^{-1}, 77 K from N$_2$ adsorption and 1350 m^2 g^{-1}, 77 K from N$_2$ adsorption, respectively, and investigated their potential for the adsorptive removal of NIABs (like metronidazole (MNZ), dimetridazole (DMZ), and menidazole (MZ)) from wastewater.

With a record-breaking adsorption capacity of 467.3 mg g^{-1}, Peng et al.[431] suggested using a highly flexible MOF MIL-53(Al) as a good adsorbent for the effective capture of dimetridazole (DMZ) from wastewater, outperforming all prior studies. Since the size of the pore channel changes with the concentration of DMZ, the results show that it may be widely employed for the adsorption of various DMZ concentrations. MOFs' great adsorption effectiveness is also a result of their enormous pore size. Additionally, for highly efficient adsorption of diclofenac sodium and chlorpromazine hydrochloride, Luo et al.[432]

decorated a MOF material ($[[(CH_3)_2NH_2]\{[Cu_2(L)\cdot(H_2O)_2]\cdot x$solvent$\}_n)$ to produce 3-D carboxylate groups because of improved π–π interactions. The adsorptive removal of antibiotics, namely the nitrofuran class (NFs) of antibiotics, using ultrarobust, hydrophobic, very porous Zr-MOFs (BUT-12 and BUT-13) was initially described by Wang et al.[433] Based on 77 K N_2 adsorption, the MOFs BUT-12 and BUT-13 showed ultrahigh BET surface areas of 3387 and 3948 m^2 g^{-1}, respectively, with pore widths of 24.7 and 30.2 Å.

3.2 Water desalination

To create high-purity or drinkable water for industrial usage, salt ions are extracted from saline water through the process of desalination. This section addresses several methods and how MOFs fit into the process.

3.2.1 Capacitive deionization.
Over the last ten years, capacitive deionization, or CDI, has drawn interest as a substitute water treatment technique. Using electrostatic forces between electrodes that are oppositely charged, CDI extracts ions from saline water. Regenerating saturated electrodes can also be accomplished by releasing the adsorbed ions into wash water through the application of a reverse potential gradient.[434] New materials are being developed and tested for membrane capacitive deionization. While a range of porous carbons, including activated carbon, reduced graphene oxide, carbon nanospheres, mesoporous carbon, carbon nanofibers, and nanotubes, have been employed as electrodes, their propensity to oxidize restricts their long-term and large-scale applications.[435]

In order to tackle this problem, MOFs were first used as active materials for capacitive deionization without carbonization by Wang et al.[436] They created a three-dimensional hybrid material with interconnected ZIF-67(Co) particles that promoted electron transmission by integrating ZIF-67(Co) into polypyrrole nanotubes in situ. As a result, an outstanding desalination capacity of 11.34 mg g^{-1} and good recyclable quality were obtained. The application of bimetal MOFs (BMOFs) with different Co/Zn ratios for improved membrane-based capacitive deionization was shown by Ding et al.[437] The specific surface area and graphitization were highly impacted by the Zn/Co molar ratio. With outstanding performance retention, the ideal porous carbon from BMOF (Zn = 3 : 1) attained a salt removal capacity of 45.62 mg g^{-1} at 1.4 V.

3.2.2 Forward osmosis (FO).
Although the concept of the forward osmosis (FO) process has been known for a long time, the process has received a lot of attention in the last ten years.[438] FO consists of two primary processes: pure water penetration from the diluted draw solution and osmotic dilution of the draw solution.[439] In order to remove new water from the feed solution, osmotic pressure must be created by the draw agents.[440]

A suitable thin-film nanocomposite (TFN) membrane was manufactured by Dai et al.[441] by introducing copper 1,4-benzene-dicarboxylate nanosheets (CuBDC-NS) into the PA active layer. The findings demonstrated that when 1.0 M NaCl was used in the AL-FS mode, the TFN membrane produced a 50% increase in water flux and a 50% decrease in reverse solute flux (RSF). Comparing conventional thin-film composite (TFC) membranes to a TFN membrane containing UiO-66 nanoparticles, Ma et al.[442] found that the TFN membrane doubled water flux and decreased RSF. In order to facilitate the FO process, Zirehpour et al.[443] added rod-shaped MOFs made of silver and 1,3,5-benzene tricarboxylic acid (3HBTC) to the polyamide (PA) layer of a TFN membrane. These MOFs' dangling carboxylic acid groups increased membrane hydrophilicity when they were distributed throughout the organic phase. The TFN membrane outperformed the TFC membrane (27 L m^{-2} h) in the Caspian Sea water test, with a water flux of 34 L m^{-2} h.

3.2.3 Reverse osmosis.
Using pressure to overcome osmotic pressure, reverse osmosis (RO) is a water purification technique that separates water molecules from impurities using a semi-permeable membrane. Considerable efforts have been undertaken to enhance the kinetics–energetics balance of the process because of its extensive global use.[444]

Hu et al.[158] proposed using MOF-embedded membranes for reverse osmosis desalination. A theoretical simulation was presented by them to illustrate the potential of ZIF-8(Zn) membranes at seawater concentrations in NaCl solutions. Hydrophobic ZIF-8(Zn) nanocrystals were experimentally added to the selective polyamide layer by Duan et al.,[445] who demonstrated an 88% increase in water permeability at even a modest MOF loading (0.05 wt%). Water permeability was improved by 162% in comparison to pure PA with additional increases in ZIF-8(Zn) loading.

The impact of ZIF-8(Zn) nanoparticles of different sizes (60, 150, and 250 nm) on the reverse osmosis capabilities of thin-film nanocomposite membranes was examined by Lee et al.[446] The interfacial area between ZIF-8(Zn) and the polyamide matrix was affected by the size-dependent deposition of nanoparticles on the support layer, which in turn affected the membrane's performance. Therefore, the performance of thin film nanocomposite membranes in reverse osmosis and interfacial polymerization is critically dependent on the filler size. Gupta et al.[447] compared five varieties of ZIF membranes—ZIF-25, ZIF-71, ZIF-93, ZIF-96, and ZIF-97—for water desalination in a different study using simulations. ZIF-96 showed the greatest affinity for water among the studied membranes, while ZIF-71, ZIF-25, and ZIF-96 showed increased water flux in comparison to ZIF-97 and ZIF-93.

Xu and Hu[5] developed a novel thin film nanocomposite membrane for water desalination by incorporating MIL-101(Cr) into a dense polyamide layer on a polysulfone substrate. MIL-101(Cr)'s porosity structure made it easier for direct water channels to form in the polyamide layer, which increased water permeance. Although the MOF loading was minimal (0.05%), the membrane showed a significant rejection of NaCl (>99%). Park et al.[448] created a thin film composite membrane for reverse osmosis by using HKUST-1(Cu) in the support layer. Sulfuric acid treatment increased HKUST-1(Cu)'s hydrophilicity, dispersion, and hydrolytic stability inside the polysulfone membrane. When compared to pure reverse osmosis membranes, this alteration maintained salt rejection efficacy while increasing water flux by 33%.
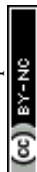
In order to functionalize the mesoporous structure of Zr-based MOF PCN-222 for reverse osmosis membranes, Bonett et al.[449] used post-synthetic modification (PSM). PCN-222 had poor salt rejection despite having a high water flux, which was improved by adding myristic acid via PSM to change the channel's dimensions and pore size distribution. The effect of adding ZIF-8(Zn) to membranes on fouling resistance was examined by Aljundi.[450] The inclusion of ZIF-8(Zn) improved the anti-fouling capabilities of the reverse osmosis membrane by reducing fouling, according to an evaluation using a bovine serum albumin fouling model. Other chemically stable MOFs, such as UiO-66(Zr), have also been used in reverse osmosis procedures. Lin et al.[451] developed hollow fiber-based thin film nanocomposite membranes with polydopamine-modified HKUST-1(Cu) for low-pressure reverse osmosis of brackish water. MOF particles were incorporated into the polyamide support matrix via interfacial polymerization, enhancing compatibility between the organic matrix and inorganic nanofillers. The MOF-composite membrane exhibited high pure water permeability (66.94 L m^{-2} h^{-1} bar^{-1}) with NaCl rejection rates of 98.2% and 97.4% at 2 and 4 bars, respectively.

3.2.4 Membrane distillation. Membrane distillation is a thermal desalination technique that involves the use of a hydrophobic membrane to separate hot saline solution from cold water streams. A partial pressure differential caused by the temperature gradient enables vapor from the saline side to cross the membrane and reach the cooler side. Because it transports vapor selectively and blocks solid and non-volatile species, the hydrophobic character of the membrane is essential for guaranteeing the accumulation of pure water.[436]

Using a novel two-step synthesis approach, MOF crystals were produced on alumina tube supports by Zuo and Chung.[452] To increase hydrophobicity and decrease surface energy, perfluoro molecules were then added. Using this method, a membrane with good desalination performance and a strong vacuum distillation flow of 32.3 L m^{-2} h^{-1} at 60 °C was produced.

A ZIF-8(Zn)/chitosan layer was added to the PVDF membrane surface in an ultrathin thin film composite membrane by Kebria et al.[453] in order to improve membrane distillation performance for water desalination. When exposed to seawater, the membrane's antifouling capabilities increased, and it demonstrated a 350% increase in permeate water flux with the ZIF-8/chitosan layer. It also showed very high NaCl rejection ($>99.5\%$). In order to create a unique super-hydrophobic nanofiber membrane for direct contact membrane distillation, Yang et al.[454] electrospun an Fe–BTC MOF and PVDF onto a nonwoven support material. The membrane demonstrated increased hydrophobicity (water contact angle: $138.06° \pm 2.18°$) and 99.9% NaCl rejection (35 g L^{-1}) in the direct contact membrane distillation process, achieving substrate attachment and a loading of up to 5 weight percent of the MOF.

3.2.5 Nanofiltration. Similar to reverse osmosis (RO), nanofiltration (NF) is a membrane liquid-separation technique.

Zhao et al.[455] used blending IP and preloading IP techniques to assess the interaction between the PA layer and three water-stable MOFs (MIL-53(Al), ZIF-8, and UiO-66-NH$_2$). In comparison to the control TFC membrane, their investigation showed that TFN membranes integrating these MOFs exhibited rougher surfaces, bigger PA layers, and higher surface negativity. Every TFN membrane showed improved performance; the TFN membrane containing UiO-66-NH$_2$ had the maximum permeability, around 1.3 times higher than those of the TFN membranes containing the other two MOFs.·CuBTC was added to the substrate layer of a polysulfone substrate by Misdan et al.[456] for NF procedures. With 0.25 weight percent CuBTC, they achieved a 25% improvement in pure water flux while keeping MgSO$_4$ rejection at 97.3%. When CuBTC was added, the membrane's hydrophilicity was enhanced, surface negativity was raised, and the surface became smoother, which decreased BSA adhesion.

Navarro et al.[457] used a Langmuir–Schaefer approach to creatively insert MOFs into the PA layer instead of blending them conventionally in the organic phase. After being placed on a cross-linked polyimide (P84) support, the MOF thin film underwent the standard IP procedure. Compared to traditional techniques that distribute MOFs throughout the organic phase, our strategy reduced the likelihood of MOF aggregation and thus membrane flaws. By adding palmitoyl chloride, Liu et al.[458] improved the dispersity of UiO-66-NH$_2$ within the PA layer. Because of this change, UiO-66-NH$_2$ is more polar in organic solvents, which lessens its tendency to aggregate. With 95% Na$_2$SO$_4$ rejection, the improved UiO-66-NH$_2$ demonstrated an increase in pure water flux from 8.1 to 12.4 L m^{-2} h bar. Over 80 hours of continuous filtering, the modified UiO-66-NH$_2$ demonstrated strong durability and consistent membrane performance, even though the non-modified nanofillers initially had higher permeability.

Zhu et al.[459] used the standard IP procedure with an organic solution after positioning UiO-66-NH$_2$ dispersed in aqueous solution using a vacuum filtering method. This method reduced MOF loss and allowed for regulated loading of UiO-66-NH$_2$, in contrast to conventional methods that cause MOF dispersion that is random and unpredictable. Better water movement access was made possible by the decreased interlocking effect without sacrificing membrane stability. ZIF-8 was used by Wang et al.[460] as a sacrificial template to create a crumpled PA layer. Through the IP method, ZIF-8 and single-walled CNTs were integrated into the PA layer. Water broke the coordination bonds in MOFs due to their limited hydrostability, which resulted in the collapse of MOF structures. According to their research, ZIF-67's geometric structure allowed for a higher effective surface area, which allowed for the accommodation of more water molecules. This led to an improved water flux of 1831 L m^{-2} h and a high Na$_2$SO$_4$ rejection rate of 97.2%.

3.3 Sensing

Because of its remarkable structural diversity and qualities, as well as its capacity to detect luminescence or electrochemical

changes, MOFs have demonstrated an amazing aptitude in the field of sensing applications. According to Lustig et al.,[461] MOFs have also demonstrated potential uses in the detection of a variety of analytes, including biomolecules, ionic species, and environmental pollutants. More precisely, detailed information will be given on DNA detection, ethylamine sensing based on MOF nanosheets, and luminous Fe^{3+} sensing.

Wang et al.[462] reported the application of surfactant as a surfactant-assisted approach in the ultrathin M-TCPP(Fe) nanosheets (M = Zn, Cu, and Co) for the quantitative detection of H_2O_2. After being constructed onto electrodes, GC/M-TCPP(Fe) nanosheets showed a standard amperometric response to H_2O_2, but with a rather low detection limit. With a detection limit in the range of 0.4×10^{-6}–$50 \times 1 \times 10^6$ M, good catalytic selectivity toward H_2O_2, high repeatability, and excellent long-term storage stability (at least five weeks), the GC/Co-TCPP(Fe) electrode demonstrated heme protein-like activity.

By taking advantage of their fluorescence quenching effect, Xu et al.[463] investigated the possibility of extremely sensitive and fast-response luminescence sensing of Fe^{3+} using luminescent MOF $Ti_2(HDOBDC)_2(H_2-DOBDC)$ (NTU-9-NS) nanosheets. The NTU-9-NS nanosheets' fluorescence quenching only takes 10 s after the addition of Fe^{3+}, in contrast to the bulky MOFs' slow response (typically several hours to a day), and their unique pore structure allows them to recognize compounds quickly. This is mainly because of the nanosheets' high dispersion and easy access to the active center on the surface. One possible explanation for NTU-9-NS's superior luminous sensing capability is the presence of easily accessible active sites on the nanosheet surface.

For the purpose of detecting cocaine, Su et al.[464] developed Au nanocluster/521-MOF nanosheet-embedded zirconium-based MOF nanosheet composites, such as ZnO@ZIF-8 nanorods, Ti@TiO$_2$/CdS/ZIF-67, and AuNCs@521-MOF. Typically, the immobilized AuNCs@521-MOF nanosheet with cocaine aptamer strands exhibited high electrochemical activity and bioaffinity, potentially creating a biosensitive platform for cocaine detection. This aptasensor demonstrated specific selectivity, a low detection limit of 0.44 ng^{-1} mL^{-1}, a wide detection range of 0.001–1.0 ng^{-1} mL^{-1}, and the ability to detect cocaine sensitivity.

The creation of a Cd-BTC MOF nanotube for the trace-level detection of nitroaromatic explosives was reported by Li et al.[465] 72.5% of the MOF nanotube's fluorescence was quenched after it was immersed in saturated vapor of 2,4-dinitrotoluene for ten seconds. Because of the special composition and structural benefits of LD MOFs, the Cd-BTC nanotube's response rate for 2,4-dinitrotoluene vapor was also among the highest values for reported fluorescence-based chemical sensing materials.

In order to accomplish two-color living cell imaging of intracellular adenosine, Wang et al.[466] employed lanthanide-based MOF nanosheets as the bioanalytical platforms. It's noteworthy that it is possible to modify the molecular ratio of the TAMRA-aptamer to the FAM aptamer loaded on dye-aptamer/MOF-Ln nanosheets in order to further detect tiny

molecules and DNA inside neurons. Also effectively used in this system was the target intracellular ATP. Additionally, this technique successfully administered the required intracellular ATP. Exfoliated ZSB-1 nanosheets have recently been employed as a fluorescence sensor to identify Fe^{3+} ions.[467] The detection limit for Fe^{3+} ions using the ultrathin ZSB-1 nanosheets was found to be 0.054×10^{-6} m, significantly lower than that of the bulk equivalent (0.110×10^{-6} m). Apart from quenching fluorescence, the LD MOF materials' fluorescence turn-on response was also examined for the purpose of detecting particular analytes, like volatile organic chemicals and uric acid.[468] Song[469] reported another MOF nanosheet with fluorescence sensing capabilities. $Mn(C_6H_8O_4)(H_2O)$ nanosheets demonstrated a lower detection limit (0.2 pM) and a comparatively wide linear detection range (1–200 pM) when combined with the hybrid chain reaction techniques. Additionally, this fluorescence sensing technology based on MOF nanosheets offered a reliable way to detect live cells.

By varying the fluorescence emission intensity and elevating the ethylamine content, Li et al.[470] were able to produce $[Zn(BDC)(H_2O)]_n$ sheets with fluorescence properties that could detect ethylamine both quantitatively and sensitively. A bio-friendly Pb(II)-based MOF nanotube was created for the purpose of detecting uric acid, as an example.[468] With a low detection limit of 4.3×10^{-3} m, the MOF nanotube exhibits strong selectivity for uric acid due to its host–guest interactions with it, resulting in responsive turn-on fluorescence.

A tunable optochemical platform based on MOF $\{(HNEt_3)\}_2[Zn_3BDC_4]$ solvent {solvent = DMF or DMA} nanosheets for the sensing of different small molecules was introduced by Chaudhari.[471] Normally, the tiny light-emitting molecules may be absorbed by these nanosheets. These functionalized guest@MOF porous nanosheets might incorporate the peculiar optical features, given the high host–guest interaction effect. Consequently, a "guest@host" composite system with adjustable luminescence characteristics can function as a platform for chemical sensing via photonics. The outstanding capacitance and humidity-sensing characteristics of Cu_3TCPP nanosheets were reported by Tian et al.[472] Despite the hydrophobic nature of the MOF's pores, the massive –COOH functional groups that are suspended around the edges of the nanosheets give the MOF nanosheets superior proton conductivity. The Cu_3TCPP nanosheets, which had been compacted into a pellet, demonstrated a high capacitance responsiveness and sensitivity at 1 kHz, along with a specific capacitance frequency characteristic at various relative humidities (RH). It's astounding that they had also shown a clear response peak from 60% to 98% RH, as well as good reversibility and repeatability over cycles of exposure and recovery from low to high RH.

In order to detect DNA, Zhao et al.[473] employed M-TCPP nanosheets (where M = Co, Cu, Zn, and Cd) as novel sensing platforms. More specifically, the MOF nanosheets may adsorb the ssDNA tagged with a dye, dimming the dye's fluorescence. Additionally, quantitative experiments were conducted using target DNA at different concentrations, showing very low

detection limits (20×10^{-12} M) and a broad detection range (0–5×10^{-12} M). All of these findings demonstrated the benefits of MOF nanosheets, which go beyond their larger surface area for DNA adsorption.

3.4 Photocatalytic degradation of pollutants

Photocatalysis (PC) utilizes semiconductor materials to initiate oxidation and reduction reactions through photon absorption, generating charge carriers (h^+/e^-).[8,474] Extending the lifetime of these photogenerated h^+/e^- pairs is crucial for effective PC, facilitating the production of reactive oxygen species (ROS) like hydroxyl radicals ($^{\bullet}OH$), superoxide radicals (by conversion of O_2 to $^{\bullet}O_2^-$), and positive holes (h^+). This approach harnesses solar radiation to enhance photoexcitation efficiency. Metal–organic frameworks (MOFs) operate similarly to semiconductors, where organic linkers act as valence bands and metallic clusters as conduction bands. In MOFs, photogenerated electrons in the lowest unoccupied molecular orbital (LUMO) convert O_2 to $^{\bullet}O_2^-$, while holes in the highest occupied molecular orbital (HOMO) generate $^{\bullet}OH$.[475]

3.4.1 Degradation of organic dyes. Significant amounts of wastewater are contaminated with dyes as a result of the dye industry's introduction of various synthetic dyes in recent years for use in printing, dyeing, medicine, and cosmetics. Every year, the textile sector alone generates about 100 tons of effluent from dyeing.[476] This effluent presents ongoing environmental concerns because it contains complex, refractory organic components with strong colors. Consequently, because MOF-based photocatalysts can drastically change dye hues, research has concentrated on employing them for dye degradation. $Cu_8Cl_5(CPT)_8(H_2O)_4(H_2O)_{20}(CH_3CN)_4$, a new multi-metal MOF, was synthesized by Chen et al.[477] by integrating the HCPT ligand with triazole and carboxylic acid functionalities. Under visible light with 30% H_2O_2, this MOF with a 3D interpenetrating network based on $[[Cu_2(CO_2)_4]]$ and $(Cu_4Cl)^{7+}$ clusters achieved 97% RhB degradation in 70 minutes. Mahmoodi et al. employed a green synthesis approach to produce Cu-based nanoporous MOF-199, which efficiently degraded Basic Blue 41 under UV light without oxidizing agents, achieving a 99% degradation rate at 0.04 g L^{-1} concentration. The catalyst primarily utilized generated $^{\bullet}OH$ radicals for degradation.[478]

Enhancing photocatalytic conditions of MOFs often involves incorporating external electron acceptors. Gao et al. studied Fe-based MIL-53 for acid orange 7 degradation and found initial inefficiencies due to electron–hole recombination under visible light. Addition of persulfate significantly improved degradation, nearing 100% efficiency within 90 minutes, by facilitating effective electron–hole separation and radical generation.[479] Despite advancements, standalone MOFs face challenges in meeting current photocatalytic demands for organic pollutant degradation. Composite catalysts combining MOFs with functionalized counterparts or other materials have emerged as viable solutions, leveraging heterojunctions to complement MOF deficiencies.[480]

TiO_2, as a well-established photocatalytic semiconductor, is commonly integrated into MOF-based catalysts. Traditional MOFs like Cu-based HKUST-1, Zn-based ZIF-8, and Ti-based MIL-125 have been combined with TiO_2 to enhance their catalytic activity for degrading dyes such as RhB or methyl orange.[481,482] However, these composite catalysts often exhibit limited effectiveness under visible light. In subsequent experiments, the composite catalyst with 5% PCN-222 content demonstrated superior photocatalytic performance, achieving a 98.5% degradation rate of RhB under visible light. This rate was ten times faster compared to either pure TiO_2 or PCN-222 alone. Analysis indicated that the composite material enhances MOFs' response to visible light and effectively suppresses electron–hole recombination by matching bandgap relationships. Key active species involved in dye degradation include h^+, $O_2^{\bullet-}$, and $^{\bullet}OH$ radicals, suggesting potential catalytic applications of MOFs under visible light.[483]

3.4.2 Degradation of pharmaceuticals and personal care products. Pharmaceuticals and personal care products (PPCPs) represent newly recognized water pollutants that have garnered significant attention. Since Daughton and Ternes first highlighted their environmental impact in 1999, countries worldwide have become increasingly concerned about PPCP pollution.[484] Due to their persistence in toxicity and tendency for bioaccumulation, PPCPs enter water environments through various pathways after use, leading to severe environmental consequences. These pollutants can adversely affect human health, induce genetic mutations in bacteria, and contribute to the development of drug-resistant pathogens.[485] Consequently, there is an urgent need to identify safe and effective methods for degrading PPCPs. MOF-based photocatalysts, as emerging materials, hold significant research promise for addressing this issue.

3.4.2.1 Degradation of antibiotics. Antibiotics are a prevalent category of substances within pharmaceuticals and personal care products (PPCPs). Current global annual antibiotic consumption is estimated to be between 100 000 and 200 000 tons.[486] To address the environmental impact of antibiotics, numerous studies have explored the degradation of antibiotics using MOF-based photocatalysts, targeting compounds such as β-lactams, tetracyclines, and quinolones. β-Lactam antibiotics, including penicillin and cephalosporins, are the most used antibacterial drugs.[487] Cephalosporins are widely utilized due to their broad-spectrum antibacterial properties. However, their extensive use necessitates the development of efficient degradation methods to mitigate environmental impact.

Askari et al.[488] developed a $CuWO_4/Bi_2S_3/ZIF-67$ ternary MOF-based heterojunction catalyst through a simple hydrothermal synthesis method. They investigated the photocatalytic degradation of cephalexin and metronidazole in a continuous flow mode, optimizing operating parameters using central composite design. Under optimal conditions and visible light irradiation, degradation efficiencies of cephalexin and metronidazole reached 90.1% and 95.6%, respectively, with maximum total organic carbon removal rates of 74% and 83.2%. The performance of the ternary photocatalyst significantly surpassed that of Bi_2S_3 and the binary $CuWO_4/Bi_2S_3$ catalyst,

exhibiting reaction rates nine and four times higher, respectively.

Wang et al.[460] examined the photocatalytic degradation of tetracycline using various Fe-based MOFs (Fe–MIL-101, Fe–MIL-100, and Fe–MIL-53). They found that MIL-101 exhibited the highest degradation efficiency, removing 96.6% of tetracycline under visible light irradiation for 3 hours at an initial concentration of 50 mg L^{-1}, outperforming MIL-100 and MIL-53 by factors of 1.7 and 2.4, respectively. Capture and ESR experiments identified $O_2^{\bullet-}$, $^{\bullet}OH$ radicals, and h^+ as the primary active species in the degradation process, demonstrating MIL-101's efficacy and providing insights into designing MOF-based catalysts for recalcitrant antibiotics.

Lei et al.[489] further optimized the photocatalytic degradation of tetracycline by constructing a composite catalyst using Fe-based MOF MIL-101 and non-metallic red phosphorus (RP). They synthesized the RP/MIL-101 heterojunction composite via a low-temperature solvothermal method. Under full-spectrum irradiation, the RP/MIL-101 catalyst with different red phosphorus mass fractions achieved tetracycline degradation efficiencies exceeding 85% within 80 minutes, significantly higher than the approximately 50% efficiency of MIL-101 alone. The RP/MIL-101 composite with 15% red phosphorus exhibited the best performance, with a degradation efficiency of 90.1% in 80 minutes.

3.4.2.2 Degradation of non-steroidal anti-inflammatory drugs. Non-steroidal anti-inflammatory drugs (NSAIDs), commonly used for fever and pain relief, are prevalent in daily life alongside antibiotics in PPCPs. Examples include acetaminophen (paracetamol), ibuprofen, and ketoprofen.[490] Despite their low biological toxicity, these drugs are stable and can accumulate in aquatic environments and organisms, leading to significant ecological impacts.[491]

For the photocatalytic degradation of paracetamol, Gomez-Aviles et al.[492] developed a hybrid Ti–Zr MOF photocatalyst by replacing some Ti atoms in the NH_2–MIL-125 MOF with Zr atoms using a solvothermal method. The catalyst with 15% Zr doping exhibited the highest activity, completely degrading paracetamol under simulated sunlight in 90 minutes. Total organic carbon (TOC) analysis indicated a 65.3% reduction, demonstrating substantial mineralization.

Cao et al.[493] synthesized a heterojunction composite catalyst of g-C_3N_4 and amino-functionalized In-based MOF MIL-68 using a solvothermal method with ultrasound assistance for the photocatalytic degradation of ibuprofen. The 10 wt% g-C_3N_4/MIL-68-NH_2 composite showed the highest activity, achieving a 93% degradation rate of ibuprofen under 180 minutes of visible light irradiation without additional oxidants. TOC removal efficiency reached 70%, and the reaction rate was 19.28 times that of g-C_3N_4 alone, highlighting its superior photocatalytic activity.

For ketoprofen degradation, Miao et al.[494] constructed a Pt/Ag-modified Ti-based MOF (MIL-125) photocatalyst using solvothermal and light deposition methods. The Pt/MIL-125/Ag composite exhibited a significant enhancement in visible light

response and photogenerated electron–hole separation due to the dual interface effect between MOF and precious metals. Using an XPA-7 photocatalytic device, the ketoprofen degradation rate reached 95.5% under 120 minutes of visible light irradiation, representing a 20-fold increase over MIL-125 alone. This demonstrates the effectiveness of dual interface design between semiconductors and precious metals for degrading recalcitrant organic pollutants.

3.4.3 Degradation of other organic pollutants. In recent years, MOF-based catalysts have also been studied for the photocatalytic degradation of residual organic pesticides in water and phenolic pollutants in chemical wastewater, such as those from petrochemicals. While these studies are less extensive than those on organic dyes and PPCPs, they primarily focus on common substances in pesticides like atrazine and malathion, as well as phenolic pollutants such as phenol and nitrophenol.

3.4.3.1 Degradation of organic pesticides. Atrazine is a widely used herbicide in agricultural crop production, but its low biodegradability results in environmental risks as it can leach into water systems through precipitation and runoff.[495] Photocatalytic degradation presents a viable solution. Xue et al. developed a MOF-based composite photocatalyst using BiOBr and UiO-66 via an in situ growth method to degrade atrazine under visible light. By forming a heterojunction with BiOBr, the recombination of UiO-66 photogenerated electron holes was reduced, enhancing visible light response. In a 240-minute reaction, 88% of atrazine was degraded, compared to 50% with BiOBr alone. The study also examined the impact of environmental factors, finding that low pH (3.1) conditions facilitated degradation, while other water qualities inhibited it. Capture experiments identified h^+ and $O_2^{\bullet-}$ as the active species.[496]

Similarly, malathion, an organophosphorus pesticide, poses environmental challenges due to its high toxicity, persistence, and residues.[497] Fakhri et al. constructed a ternary MOF-based heterojunction catalyst using graphene oxide and ZnO to degrade malathion, based on UiO-66. The Z-type heterojunction and graphene oxide's electron mobility enhanced charge carrier separation and visible light response of UiO-66. The UiO-66@45 ZG composite achieved 100% malathion degradation within 90 minutes. This study offers an effective strategy for designing MOF-based photocatalysts.[498]

3.4.3.2 Degradation of phenolic pollutants. Phenolic pollutants in water primarily originate from human activities, with industries such as petrochemical and pharmaceuticals often discharging these toxic, stable, and slow-degrading substances into aquatic systems.[499] Common phenolic pollutants include phenol, naphthol, chlorophenol, and nitrophenol.

Chen et al. developed a composite MOF-based photocatalyst, Pt@UiO-66-NH_2, by dispersing Pt on UiO-66-NH_2. To study phenol degradation, they created a photocatalytic membrane reactor (PMR) using α-Al_2O_3 as the base carrier. This catalyst, with a Pt/Zr ratio of 0.5, achieved 70% mineralization of phenol within 300 minutes under simulated sunlight. The

PMR showed good reusability and maintained high catalytic activity after multiple cycles, providing a scalable design strategy for degrading phenolic pollutants in water.[500]

For α-naphthol, a toxic phenolic pollutant, Abdelhameed *et al.* designed a multi-component nanocatalyst by combining MOFs ZIF-67, ZIF-8, and MIL-125-NH$_2$. The resulting ZIF-67@ZIF-8@MIL-125-NH$_2$ catalyst degraded 98.9% of α-naphthol under visible light within 120 minutes, significantly outperforming ZIF-8@MIL-125-NH$_2$ and ZIF-67@MIL-125-NH$_2$. This ternary MOF material retained a 94% degradation rate after five uses, showing promise for industrial wastewater treatment.[501]

For chlorophenols, Zhang *et al.* synthesized a mesoporous core–shell heterojunction catalyst using NH$_2$–MIL-125 and Bi$_2$MoO$_6$. This catalyst improved charge separation and provided ample active surface sites, achieving 93.28% and 92.19% degradation efficiency for dichlorophenol and trichlorophenol, respectively, under visible light in 180 minutes.

In a subsequent study, Zhang *et al.*[502] developed a hierarchical tandem core–shell heterojunction catalyst, NH$_2$–MIL-125(Ti)@ZnIn$_2$S$_4$/CdS, achieving 98.6% and 97.5% degradation efficiencies for dichlorophenol and trichlorophenol, respectively. For nitrophenol, Li *et al.* constructed a heterostructure using aminated Fe-based MOF NH$_2$–MIL-53 grown on g-C$_3$N$_4$ doped with pyromellitimide (g-C$_3$N$_4$/PDI). The resulting g-C$_3$N$_4$/PDI@MOF catalyst achieved 100% degradation of *p*-nitrophenol within 30 minutes under visible light and in the presence of H$_2$O$_2$, demonstrating the effectiveness of energy-level matching heterojunctions in enhancing photogenerated electron transfer for MOFs.[503]

3.4.3.3 Degradation of other PPCPs. In addition to pharmaceuticals, various chemicals in personal care products can enter the environment post-use, causing ecological issues. Notable examples include the fungicide triclosan and the industrial chemical bisphenol A (BPA). Triclosan, a broad-spectrum bactericide, is present in nearly all daily toiletries.[504]

To investigate triclosan degradation under visible light, Bariki *et al.* constructed a coupled semiconductor heterojunction using heat-resistant and acid-resistant Zr-based MOF UiO-66 and CdIn$_2$S$_4$ *via* a solvothermal method. The triclosan degradation rate reached 92% within 180 minutes, with a degradation rate constant approximately 12 times that of pure CdIn$_2$S$_4$, indicating the enhanced photocatalytic activity of the MOF-based photocatalyst. O$_2^{\bullet-}$ and $^{\bullet}$OH radicals were identified as the main active species in the degradation reaction.[505] Tang *et al.* developed a composite material by combining Cr-based MOF MIL-101 and the classic photocatalyst TiO$_2$ to degrade BPA. The TiO$_2$@MIL-101(Cr) composite catalyst, synthesized *via* a solvothermal method, demonstrated enhanced photocatalytic activity due to improved photogenerated electron–hole separation and reduced band gap width. In experiments, the composite catalyst achieved a 99.4% BPA degradation rate within 240 minutes under UV irradiation, significantly outperforming the individual catalysts.

Mechanistic studies confirmed that O$_2^{\bullet-}$ was the primary active species in the degradation process.[506]

4. Major challenges with the use of MOFs

In the last few years, great strides have been made in the energy and environmental applications of MOFs. In order to ensure robust field applications of MOF-based materials, a number of challenges as well as the potential research avenues for further investigation have been outlined here.

[1] The vast majority of documented research studies use popular MOF types like MIL, ZIF, PBAs, *etc.* as precursors or sacrificial templates for their investigations. In order to achieve optimal performance, it is crucial to investigate different MOFs, particularly those with characteristics that are specifically created. Furthermore, because of our limited knowledge of their reaction mechanisms, papers on metal chalcogenides, metal phosphides, and metal carbides are rather rare. Instead, the majority of documented investigations have concentrated on converting MOFs into carbonaceous materials, metal oxides, and their composites.

[2] When creating novel MOFs for the adsorption of contaminants, appropriate ligand and metal salt choices should be taken into account. It is important to monitor the reaction's operational parameters, such as temperature, pressure, solvent selection and quantity, to achieve tunable porosity forms and sizes as well as enhanced surface morphologies.

[3] A great deal of innovative MOF adsorbents still need to be created with intense and tenacious research interest for ground-breaking advancements for present and future applications, to highlight their potential for further laboratory, medical, industrial, and environmental usage.

[4] Although many MOF-derived materials have a high porosity and surface area, precise control over the size and shape of the pores is frequently lacking in the preparation processes of some of these materials. In order to effectively decontaminate water or wastewater systems containing an array of pollutants (*e.g.*, synthetic dyes, heavy metals, endocrine-disrupting chemicals, pesticides, food additives, veterinary, pharmaceutical, personal care products, antibiotics, biological and chemical weapons, and other industrial chemicals), future research into finding more practical MOF synthetic techniques should focus on achieving very low-cost MOFs that are more useful especially as adsorbents. Such methods should yield adsorbents that are capable of taking the place of the pricy commercial activated carbons.

[5] The incomplete knowledge of self-assembly in a confined reaction environment makes it challenging to determine the morphology and structure of MOF derivatives target structures for the new form MOFs. Given our poor understanding of the evolution mechanism, the conversion process from MOFs to their derivatives remains unclear. Understanding these mechanisms is aided by emerging technologies such as aberration-corrected high-angle annular dark-field imaging
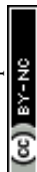
scanning transmission electron microscopy, X-ray absorption near edge structure, and X-ray absorption fine structure. Our ability to design and build appropriate MOFs with regular or hierarchical porosity, customizable composition, and high surface area will depend on our profound understanding of the self-assembly mechanism.

[6] The usage of MOFs is hindered by their small pore sizes, which are within the micropore ranges in diameter. This places a substantial restriction on the amount of contaminants that the frameworks can absorb. This means that MOFs with pores in the mesoporous range must now be synthesized in order to improve their use over other adsorbent materials. However, the MOFs' regeneration mechanism and reusability continue to be crucial. Therefore, more thorough research is needed in this field to discover a better or alternate physical technique for recovering the used MOF adsorbents in order to create a more feasible and cost-effective option.

[7] Hybrid materials produced from MOFs have demonstrated promising uses in energy conversion and storage, but their volumetric energy densities are very modest. This restriction is mostly caused by their low-density porous architectures. To better understand the impact of various electronic and chemical environments as well as structural influences on materials' function, additional MOFs should be added to derivatives and composites for energy applications.

[8] Ultimately, it is necessary to conduct parallel analyses of the side effects of various MOF adsorbents and applications in order to confidently reap the benefits of employing qualified adsorbents in pollutant removal. Regretfully, most researchers consistently overlook this crucial component. As a result, it is anticipated that risk assessments will evaluate how consumers use the products, how to safely dispose the synthesized materials and apply the same for the adsorption of waste products, and how they might affect the receiving bodies.

Notwithstanding these enormous obstacles, the progress made thus far is genuinely encouraging, and studies on the materials discussed in this review are only the beginning of the research on MOF-based materials. There are excellent prospects to realize the practical applications of MOF-based materials in the realms of environmental science and renewable energy with continued research contributions in these areas.

5. Conclusion and future research perspectives

The overuse of fossil fuels, environmental pollution resulting from the indiscriminate usage, and the release or leakage of hazardous gases from industries have all contributed to a growing concern regarding the effective storage of renewable energy and the management of environmental pollution. Ensuring the efficient storage and utilization of eco-friendly energy sources and the removal of hazardous substances are critical for safeguarding the ecosystem and maintaining public health. Finding innovative materials with appropriate qualities has emerged as a powerful strategy to lessen the growing

worries about environmental contamination. Current advancements in the study of metal–organic frameworks (MOFs), MOF composites, and MOF derivatives (such as metals, oxides, sulfides, and their composites) have shown the effectiveness of using MOF-based materials as precursors or sacrificial templates to prepare a variety of novel materials with unusual structures. Thus far, a multitude of MOF-derived hybrid materials with diverse compositions, morphologies, structures, characteristics, and functions have been successfully obtained and applied to a broad range of applications. Owing to their encouraging characteristics, MOF-derived hybrid micro-/nanostructures have found extensive application in energy storage and conversion devices, such as fuel cells, solar cells, batteries, and supercapacitors. Apart from their varied applications in the adsorption of dyes and heavy metals and the elimination of hazardous gases from environmental pollution control systems, they have better reusability characteristics than many traditional adsorbents, which is helpful for lowering processing expenses and related wastes using the pollutant removal procedures.

In order to gain a basic understanding of the adsorption, catalytic, and sensing mechanisms as well as the relationship between the structure and performance of MOF derivatives, numerous issues still need to be investigated at the lab scale in the future. This knowledge could offer guidance for the redesign and development of MOF-derived nanomaterials. Undoubtedly, in order to truly achieve environmental protection, more work needs to be done on MOF derivatives in order to realize their commercial applications. Scientists need to concentrate on simplified synthesis processes and optimizing costs while exploring ways to enhance their stability, selectivity, and reusability. Hence, to optimize their efficiency and guarantee their industrial applications under a variety of challenging circumstances, emphasis must be placed on the manufacture of MOF derivatives with distinctive features. Finally, future research should focus heavily on how to integrate MOF films with other parts of the devices for real-world use.

Data availability

No primary research results, software or codes have been included and no new data have been generated or analysed as part of this review.

Conflicts of interest

There are no conflicts to declare.

References

1 M. Yusuf, et al., Metal–organic framework-based composites for biogas and natural gas uptake: an overview of adsorption and storage mechanisms of gaseous fuels, Chem. Eng. J., 2023, 147302.

2 M. Mon, et al., Metal–organic framework technologies for water remediation: towards a sustainable ecosystem, J. Mater. Chem. A, 2018, 6(12), 4912–4947.

3 O. M. Yaghi, et al., Reticular synthesis and the design of new materials, Nature, 2003, 423(6941), 705–714.

4 K. Madhushani, et al., Metal–Organic Framework-based Composites for Energy, Catalytic, and Environmental Applications: A Critical Review, Inorg. Chem. Commun., 2023, 111446.

5 H. Xu and P. Hu, Progress on fundamentals of adsorption transport of metal–organic frameworks materials and sustainable applications for water harvesting and carbon capture, J. Cleaner Prod., 2023, 136253.

6 A. N. Amenaghawon, et al., A comprehensive review of recent advances in the synthesis and application of metal–organic frameworks (MOFs) for the adsorptive sequestration of pollutants from wastewater, Sep. Purif. Technol., 2023, 123246.

7 O. K. Farha, et al., Metal–organic framework materials with ultrahigh surface areas: is the sky the limit?, J. Am. Chem. Soc., 2012, 134(36), 15016–15021.

8 S. Gautam, et al., Metal oxides and metal organic frameworks for the photocatalytic degradation: a review, J. Environ. Chem. Eng., 2020, 8(3), 103726.

9 M. Moharramnejad, et al., A simple, robust, and efficient structural model to predict thermal stability of zinc metal–organic frameworks (Zn-MOFs): the QSPR approach, Microporous Mesoporous Mater., 2022, 336, 111815.

10 V. Ve Butova, et al., Metal–organic frameworks: structure, properties, methods of synthesis and characterization, Russ. Chem. Rev., 2016, 85(3), 280.

11 H. Deng, et al., Large-pore apertures in a series of metal–organic frameworks, Science, 2012, 336(6084), 1018–1023.

12 H. Furukawa, et al., Isoreticular expansion of metal–organic frameworks with triangular and square building units and the lowest calculated density for porous crystals, Inorg. Chem., 2011, 50(18), 9147–9152.

13 H. Furukawa, et al., The chemistry and applications of metal–organic frameworks, Science, 2013, 341(6149), 1230444.

14 K. Hofmann and F. Küspert, Verbindungen von kohlenwasserstoffen mit metallsalzen, Z. Anorg. Chem., 1897, 15(1), 204–207.

15 J. Rayner and H. M. Powell, 67 Structure of molecular compounds. Part X. Crystal structure of the compound of benzene with an ammonia–nickel cyanide complex, J. Am. Chem. Soc., 1952, 319–328.

16 B. F. Hoskins and R. Robson, Infinite polymeric frameworks consisting of three dimensionally linked rod-like segments, J. Am. Chem. Soc., 1989, 111(15), 5962–5964.

17 B. F. Hoskins and R. Robson, Design and construction of a new class of scaffolding-like materials comprising infinite polymeric frameworks of 3D-linked molecular rods. A reappraisal of the zinc cyanide and cadmium cyanide structures and the synthesis and structure of the diamond-related frameworks $[N(CH_3)_4][CuIZnII(CN)_4]$ and CuI $[4,4',4'',4'''$-tetracyanotetraphenylmethane] $BF_4 \cdot xC_6H_5NO_2$, J. Am. Chem. Soc., 1990, 112(4), 1546–1554.

18 M. Fujita, et al., Preparation, clathration ability, and catalysis of a two-dimensional square network material composed of cadmium(II) and 4,4'-bipyridine, J. Am. Chem. Soc., 1994, 116(3), 1151–1152.

19 O. M. Yaghi, G. Li and H. Li, Selective binding and removal of guests in a microporous metal–organic framework, Nature, 1995, 378(6558), 703–706.

20 H. Li, et al., Design and synthesis of an exceptionally stable and highly porous metal–organic framework, Nature, 1999, 402(6759), 276–279.

21 M. Eddaoudi, et al., Systematic design of pore size and functionality in isoreticular MOFs and their application in methane storage, Science, 2002, 295(5554), 469–472.

22 D. N. Dybtsev, H. Chun and K. Kim, Rigid and flexible: a highly porous metal–organic framework with unusual guest-dependent dynamic behavior, Angew. Chem., 2004, 116(38), 5143–5146.

23 C. Jeong, et al., A review on metal–organic frameworks for the removal of hazardous environmental contaminants, Sep. Purif. Technol., 2023, 305, 122416.

24 L. Pellenz, et al., A comprehensive guide for characterization of adsorbent materials, Sep. Purif. Technol., 2023, 305, 122435.

25 A. Mahmad, et al., Experimental and molecular modelling approach for rapid adsorption of Bisphenol A using Zr and Fe based metal–organic frameworks, Inorg. Chem. Commun., 2022, 142, 109604.

26 T. Yang, et al., Yttrium-based metal–organic frameworks: controllable synthesis, growth mechanism and the phase transformation to $Y_2O_3:Eu^{3+}$ phosphors, J. Lumin., 2019, 214, 116567.

27 M. Gopiraman, et al., Three-dimensional cheese-like carbon nanoarchitecture with tremendous surface area and pore construction derived from corn as superior electrode materials for supercapacitors, Appl. Surf. Sci., 2017, 409, 52–59.

28 R. Wang, et al., Transmission electron microscopy, Progress in Nanoscale Characterization and Manipulation, 2018, pp. 69–203.

29 P. Behera, et al., MOF derived nano-materials: a recent progress in strategic fabrication, characterization and mechanistic insight towards divergent photocatalytic applications, Coord. Chem. Rev., 2022, 456, 214392.

30 M. Thommes, Physical adsorption characterization of nanoporous materials, Chem. Ing. Tech., 2010, 82(7), 1059–1073.

31 G. Sargazi, et al., A systematic study on the use of ultrasound energy for the synthesis of nickel–metal organic framework compounds, Ultrason. Sonochem., 2015, 27, 395–402.

32 P. V. Dau, K. K. Tanabe and S. M. Cohen, Functional group effects on metal–organic framework topology, Chem. Commun., 2012, 48(75), 9370–9372.

33 H. R. Abid, et al., Synthesis, characterization, and CO_2 adsorption of three metal–organic frameworks (MOFs):

MIL-53, MIL-96, and amino-MIL-53, *Polyhedron*, 2016, **120**, 103–111.

34 Y. Zhao, *et al.*, Synthesis of metal–organic framework nanosheets with high relaxation rate and singlet oxygen yield, *Chem. Mater.*, 2018, **30**(21), 7511–7520.

35 W. W. Lestari, *et al.*, *Solvothermal and electrochemical synthetic method of HKUST-1 and its methane storage capacity*, *IOP Conference Series: Materials Science and Engineering*, IOP Publishing, 2016.

36 P. Kalimuthu, *et al.*, Comparative evaluation of Fe-, Zr-, and La-based metal–organic frameworks derived from recycled PET plastic bottles for arsenate removal, *Chemosphere*, 2022, **294**, 133672.

37 H. R. Abid, *et al.*, Enhanced CO_2 adsorption and selectivity of CO_2/N_2 on amino-MIL-53(Al) synthesized by polar co-solvents, *Energy Fuels*, 2017, **32**(4), 4502–4510.

38 L. Bromberg, *et al.*, Chromium(III) terephthalate metal organic framework (MIL-101): HF-free synthesis, structure, polyoxometalate composites, and catalytic properties, *Chem. Mater.*, 2012, **24**(9), 1664–1675.

39 K. Pandi, *et al.*, Design and synthesis of biopolymer-derived porous graphitic carbon covered iron-organic frameworks for depollution of arsenic from waters, *Chemosphere*, 2020, **254**, 126769.

40 X. He, *et al.*, Exceptional adsorption of arsenic by zirconium metal–organic frameworks: engineering exploration and mechanism insight, *J. Colloid Interface Sci.*, 2019, **539**, 223–234.

41 G. Lv, *et al.*, Selectivity adsorptive mechanism of different nitrophenols on UiO-66 and UiO-66-NH_2 in aqueous solution, *J. Chem. Eng. Data*, 2016, **61**(11), 3868–3876.

42 S. M. Prabhu, S. Imamura and K. Sasaki, Mono-, di-, and tricarboxylic acid facilitated lanthanum-based organic frameworks: insights into the structural stability and mechanistic approach for superior adsorption of arsenate from water, *ACS Sustainable Chem. Eng.*, 2019, **7**(7), 6917–6928.

43 S. Dang, Q.-L. Zhu and Q. Xu, Nanomaterials derived from metal–organic frameworks, *Nat. Rev. Mater.*, 2017, **3**(1), 1–14.

44 L. Wang, *et al.*, Metal–organic frameworks for energy storage: batteries and supercapacitors, *Coord. Chem. Rev.*, 2016, **307**, 361–381.

45 Y. Korenblit, *et al.*, High-rate electrochemical capacitors based on ordered mesoporous silicon carbide-derived carbon, *ACS Nano*, 2010, **4**(3), 1337–1344.

46 Y. Zhu, *et al.*, Carbon-based supercapacitors produced by activation of graphene, *Science*, 2011, **332**(6037), 1537–1541.

47 M. Kaempgen, *et al.*, Printable thin film supercapacitors using single-walled carbon nanotubes, *Nano Lett.*, 2009, **9**(5), 1872–1876.

48 G. Wang, L. Zhang and J. Zhang, A review of electrode materials for electrochemical supercapacitors, *Chem. Soc. Rev.*, 2012, **41**(2), 797–828.

49 P. Zhang, *et al.*, Formation of double-shelled zinc–cobalt sulfide dodecahedral cages from bimetallic zeolitic imidazolate frameworks for hybrid supercapacitors, *Angew. Chem.*, 2017, **129**(25), 7247–7251.

50 S. Kuyuldar, D. T. Genna and C. Burda, On the potential for nanoscale metal–organic frameworks for energy applications, *J. Mater. Chem. A*, 2019, **7**(38), 21545–21576.

51 D. Sheberla, *et al.*, Conductive MOF electrodes for stable supercapacitors with high areal capacitance, *Nat. Mater.*, 2017, **16**(2), 220–224.

52 H. Ji, *et al.*, Capacitance of carbon-based electrical double-layer capacitors, *Nat. Commun.*, 2014, **5**(1), 3317.

53 K. M. Choi, *et al.*, Supercapacitors of nanocrystalline metal–organic frameworks, *ACS Nano*, 2014, **8**(7), 7451–7457.

54 H. Wang, *et al.*, Metal–organic frameworks for energy applications, *Chem*, 2017, **2**(1), 52–80.

55 W. H. Li, *et al.*, Conductive metal–organic framework nanowire array electrodes for high-performance solid-state supercapacitors, *Adv. Funct. Mater.*, 2017, **27**(27), 1702067.

56 B. Liu, *et al.*, Metal–organic framework as a template for porous carbon synthesis, *J. Am. Chem. Soc.*, 2008, **130**(16), 5390–5391.

57 J. Yang, *et al.*, Metal–organic frameworks: a new promising class of materials for a high performance supercapacitor electrode, *J. Mater. Chem. A*, 2014, **2**(39), 16640–16644.

58 L. Wang, *et al.*, Flexible solid-state supercapacitor based on a metal–organic framework interwoven by electrochemically-deposited PANI, *J. Am. Chem. Soc.*, 2015, **137**(15), 4920–4923.

59 D. Feng, *et al.*, Robust and conductive two-dimensional metal–organic frameworks with exceptionally high volumetric and areal capacitance, *Nat. Energy*, 2018, **3**(1), 30–36.

60 S. Bi, *et al.*, Molecular understanding of charge storage and charging dynamics in supercapacitors with MOF electrodes and ionic liquid electrolytes, *Nat. Mater.*, 2020, **19**(5), 552–558.

61 Q. Li, *et al.*, Fabrication of ordered macro–microporous single-crystalline MOF and its derivative carbon material for supercapacitor, *Adv. Energy Mater.*, 2020, **10**(33), 1903750.

62 B. Y. Guan, *et al.*, Formation of onion-like $NiCo_2S_4$ particles via sequential ion-exchange for hybrid supercapacitors, *Adv. Mater.*, 2017, **29**(6), 1605051.

63 S. Sharma, K. K. Jain and A. Sharma, Solar cells: in research and applications—a review, *Mater. Sci. Appl.*, 2015, **6**(12), 1145.

64 M. Yahya, *et al.*, Organic/metal–organic photosensitizers for dye-sensitized solar cells (DSSC): recent developments, new trends, and future perceptions, *Dyes Pigm.*, 2021, **192**, 109227.

65 N. A. Karim, *et al.*, Nanostructured photoanode and counter electrode materials for efficient Dye-Sensitized Solar Cells (DSSCs), *Sol. Energy*, 2019, **185**, 165–188.

66 Z. L. Guo, *et al.*, Enhanced electron extraction using ZnO/ZnO–SnO_2 solid double-layer photoanode thin films for efficient dye sensitized solar cells, *Thin Solid Films*, 2019, **684**, 1–8.

67 X. Sun, et al., One-step preparation of mirror-like NiS nanosheets on ITO for the efficient counter electrode of dye-sensitized solar cells, Chem. Commun., 2014, 50(69), 9869–9871.

68 S. Peng, et al., $Ni_{1-x}Pt_x$ (x = 0–0.08) films as the photocathode of dye-sensitized solar cells with high efficiency, Nano Res., 2009, 2, 484–492.

69 M. Wu, et al., Low-cost dye-sensitized solar cell based on nine kinds of carbon counter electrodes, Energy Environ. Sci., 2011, 4(6), 2308–2315.

70 R. Trevisan, et al., PEDOT nanotube arrays as high performing counter electrodes for dye sensitized solar cells. Study of the interactions among electrolytes and counter electrodes, Adv. Energy Mater., 2011, 1(5), 781–784.

71 Y. Li, et al., Metal–organic frameworks: promising materials for improving the open circuit voltage of dye-sensitized solar cells, J. Mater. Chem., 2011, 21(43), 17259–17264.

72 W. Xing, et al., Tellurophene-based metal–organic framework nanosheets for high-performance organic solar cells, J. Power Sources, 2018, 401, 13–19.

73 G. Xiang, et al., Surface-specific interaction by structure-match confined pure high-energy facet of unstable $TiO_2(B)$ polymorph, Sci. Rep., 2013, 3(1), 1411.

74 H. A. Lopez, et al., Photochemical response of commercial MOFs: $Al_2(BDC)_3$ and its use as active material in photovoltaic devices, J. Phys. Chem. C, 2011, 115(45), 22200–22206.

75 J. Dou, et al., Metal–organic framework derived hierarchical porous anatase TiO_2 as a photoanode for dye-sensitized solar cell, Cryst. Growth Des., 2016, 16(1), 121–125.

76 Q. Fan, et al., High-performance as-cast nonfullerene polymer solar cells with thicker active layer and large area exceeding 11% power conversion efficiency, Adv. Mater., 2018, 30(6), 1704546.

77 S. Dai, et al., Fused nonacyclic electron acceptors for efficient polymer solar cells, J. Am. Chem. Soc., 2017, 139(3), 1336–1343.

78 N. D. Eastham, et al., Hole-transfer dependence on blend morphology and energy level alignment in polymer: ITIC photovoltaic materials, Adv. Mater., 2018, 30(3), 1704263.

79 K. Sasitharan, et al., Metal–organic framework nanosheets for enhanced performance of organic photovoltaic cells, J. Mater. Chem. A, 2020, 8(12), 6067–6075.

80 J. Song, et al., Progress and perspective on inorganic $CsPbI_2Br$ perovskite solar cells, Adv. Energy Mater., 2022, 12(40), 2201854.

81 W. Tress, Perovskite solar cells on the way to their radiative efficiency limit–insights into a success story of high open-circuit voltage and low recombination, Adv. Energy Mater., 2017, 7(14), 1602358.

82 M. I. H. Ansari, A. Qurashi and M. K. Nazeeruddin, Frontiers, opportunities, and challenges in perovskite solar cells: a critical review, J. Photochem. Photobiol., C, 2018, 35, 1–24.

83 Z. Wang, et al., Stability of perovskite solar cells: a prospective on the substitution of the A cation and X anion, Angew. Chem., Int. Ed., 2017, 56(5), 1190–1212.

84 Z. Chu, et al., Impact of grain boundaries on efficiency and stability of organic–inorganic trihalide perovskites, Nat. Commun., 2017, 8(1), 2230.

85 Z. Song, et al., Pathways toward high-performance perovskite solar cells: review of recent advances in organo-metal halide perovskites for photovoltaic applications, J. Photonics Energy, 2016, 6(2), 022001.

86 U. Ryu, et al., Nanocrystalline titanium metal–organic frameworks for highly efficient and flexible perovskite solar cells, ACS Nano, 2018, 12(5), 4968–4975.

87 A. V. Vinogradov, et al., The first depleted heterojunction TiO_2-MOF-based solar cell, Chem. Commun., 2014, 50(71), 10210–10213.

88 C. C. Lee, et al., Enhancing efficiency and stability of photovoltaic cells by using perovskite/Zr-MOF heterojunction including bilayer and hybrid structures, Adv. Sci., 2019, 6(5), 1801715.

89 M. Li, et al., Doping of $[In_2(phen)_3Cl_6]\cdot CH_3CN\cdot 2H_2O$ Indium-Based Metal–Organic Framework into Hole Transport Layer for Enhancing Perovskite Solar Cell Efficiencies, Adv. Energy Mater., 2018, 8(10), 1702052.

90 D. Shen, et al., Metal–organic frameworks at interfaces of hybrid perovskite solar cells for enhanced photovoltaic properties, Chem. Commun., 2018, 54(10), 1253–1256.

91 R. F. Service, The battery builder, American Association for the Advancement of Science, 2016.

92 R. Yuksel, et al., Metal–organic framework integrated anodes for aqueous zinc–ion batteries, Adv. Energy Mater., 2020, 10(16), 1904215.

93 H. Hong, et al., Ordered macro–microporous metal–organic framework single crystals and their derivatives for rechargeable aluminum–ion batteries, J. Am. Chem. Soc., 2019, 141(37), 14764–14771.

94 Y. Fu, et al., High-performance reversible aqueous Zn–ion battery based on porous MnO_x nanorods coated by MOF-derived N-doped carbon, Adv. Energy Mater., 2018, 8(26), 1801445.

95 M. E. Ziebel, et al., Effects of covalency on anionic redox chemistry in semiquinoid-based metal–organic frameworks, J. Am. Chem. Soc., 2020, 142(5), 2653–2664.

96 S. Zhou, et al., Cellulose nanofiber@ conductive metal–organic frameworks for high-performance flexible supercapacitors, ACS Nano, 2019, 13(8), 9578–9586.

97 Z. Zhang, H. Yoshikawa and K. Awaga, Monitoring the solid-state electrochemistry of Cu(2,7-AQDC)(AQDC = anthraquinone dicarboxylate) in a lithium battery: coexistence of metal and ligand redox activities in a metal–organic framework, J. Am. Chem. Soc., 2014, 136(46), 16112–16115.

98 K. Wada, et al., Multielectron-transfer-based rechargeable energy storage of two-dimensional coordination frameworks with non-innocent ligands, Angew. Chem., Int. Ed., 2018, 57(29), 8886–8890.

99 Q. Jiang, et al., A redox-active 2D metal–organic framework for efficient lithium storage with extraordinary high capacity, Angew. Chem., Int. Ed., 2020, 59(13), 5273–5277.
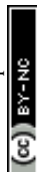
100 X. Lou, et al., Room-temperature synthesis of a cobalt 2,3,5,6-tetrafluoroterephthalic coordination polymer with enhanced capacity and cycling stability for lithium batteries, New J. Chem., 2017, 41(4), 1813–1819.

101 T. Gong, et al., Pillared-layer metal–organic frameworks for improved lithium-ion storage performance, ACS Appl. Mater. Interfaces, 2017, 9(26), 21839–21847.

102 F. Zou, et al., Metal organic frameworks derived hierarchical hollow NiO/Ni/graphene composites for lithium and sodium storage, ACS Nano, 2016, 10(1), 377–386.

103 P. Qi, et al., MOF derived composites for cathode protection: coatings of LiCoO$_2$ from UiO-66 and MIL-53 as ultra-stable cathodes, Chem. Commun., 2015, 51(62), 12391–12394.

104 X. Yang, et al., The catalytic effect of bismuth for VO^{2+}/VO^{2+} and V^{3+}/V^{2+} redox couples in vanadium flow batteries, J. Energy Chem., 2017, 26(1), 1–7.

105 P. Su, et al., Enhanced lithium storage capacity of Co$_3$O$_4$ hexagonal nanorings derived from Co-based metal organic frameworks, J. Mater. Chem. A, 2014, 2(41), 17408–17414.

106 H. Hu, et al., Unusual formation of CoSe@ carbon nanoboxes, which have an inhomogeneous shell, for efficient lithium storage, Angew. Chem., Int. Ed., 2016, 55(33), 9514–9518.

107 R. R. Kapaev, et al., Nickel(II) and copper(II) coordination polymers derived from 1,2,4,5-tetraaminobenzene for lithium-ion batteries, Chem. Mater., 2019, 31(14), 5197–5205.

108 T. L. A. Nguyen, et al., 3-D coordination polymers based on the tetrathiafulvalenetetracarboxylate (TTF-TC) derivative: synthesis, characterization, and oxidation issues, Inorg. Chem., 2010, 49(15), 7135–7143.

109 Z. Peng, et al., Triphenylamine-based metal–organic frameworks as cathode materials in lithium-ion batteries with coexistence of redox active sites, high working voltage, and high rate stability, ACS Appl. Mater. Interfaces, 2016, 8(23), 14578–14585.

110 W. Guo, W. Sun and Y. Wang, Multilayer CuO@ NiO hollow spheres: microwave-assisted metal–organic-framework derivation and highly reversible structure-matched stepwise lithium storage, ACS Nano, 2015, 9(11), 11462–11471.

111 G. Férey, et al., Mixed-valence Li/Fe-based metal–organic frameworks with both reversible redox and sorption properties, Angew. Chem., Int. Ed., 2007, 46(18), 3259–3263.

112 S. J. Yang, et al., Preparation and exceptional lithium anodic performance of porous carbon-coated ZnO quantum dots derived from a metal–organic framework, J. Am. Chem. Soc., 2013, 135(20), 7394–7397.

113 X.-F. Lu, et al., An alkaline-stable, metal hydroxide mimicking metal–organic framework for efficient electrocatalytic oxygen evolution, J. Am. Chem. Soc., 2016, 138(27), 8336–8339.

114 J. Zhang, et al., Double-shelled nanocages with cobalt hydroxide inner shell and layered double hydroxides outer shell as high-efficiency polysulfide mediator for lithium–sulfur batteries, Angew. Chem., 2016, 128(12), 4050–4054.

115 J. Zheng, et al., Lewis acid–base interactions between polysulfides and metal organic framework in lithium sulfur batteries, Nano Lett., 2014, 14(5), 2345–2352.

116 S. Bai, et al., Metal–organic framework-based separator for lithium–sulfur batteries, Nat. Energy, 2016, 1(7), 1–6.

117 A. E. Baumann, et al., Promoting sulfur adsorption using surface Cu sites in metal–organic frameworks for lithium sulfur batteries, J. Mater. Chem. A, 2018, 6(11), 4811–4821.

118 Y. He, et al., Simultaneously inhibiting lithium dendrites growth and polysulfides shuttle by a flexible MOF-based membrane in Li–S batteries, Adv. Energy Mater., 2018, 8(34), 1802130.

119 M. Li, et al., Metal–organic framework-based separators for enhancing Li–S battery stability: mechanism of mitigating polysulfide diffusion, ACS Energy Lett., 2017, 2(10), 2362–2367.

120 B. Liu, et al., Metal–organic frameworks/conducting polymer hydrogel integrated three-dimensional free-standing monoliths as ultrahigh loading Li–S battery electrodes, Nano Lett., 2019, 19(7), 4391–4399.

121 G. Xu, et al., Sulfur embedded in metal organic framework-derived hierarchically porous carbon nanoplates for high performance lithium–sulfur battery, J. Mater. Chem. A, 2013, 1(14), 4490–4496.

122 H. B. Wu, et al., Embedding sulfur in MOF-derived microporous carbon polyhedrons for lithium–sulfur batteries, Chem. – Eur. J., 2013, 19(33), 10804–10808.

123 T. Liu, et al., Selenium embedded in metal–organic framework derived hollow hierarchical porous carbon spheres for advanced lithium–selenium batteries, ACS Appl. Mater. Interfaces, 2016, 8(25), 16063–16070.

124 X.-J. Hong, et al., Cerium based metal–organic frameworks as an efficient separator coating catalyzing the conversion of polysulfides for high performance lithium–sulfur batteries, ACS Nano, 2019, 13(2), 1923–1931.

125 H. B. Wu, et al., Porous molybdenum carbide nano-octahedrons synthesized via confined carburization in metal–organic frameworks for efficient hydrogen production, Nat. Commun., 2015, 6(1), 6512.

126 J. Zhou, et al., The impact of the particle size of a metal–organic framework for sulfur storage in Li–S batteries, J. Mater. Chem. A, 2015, 3(16), 8272–8275.

127 X.-J. Hong, et al., Confinement of polysulfides within bi-functional metal–organic frameworks for high performance lithium–sulfur batteries, Nanoscale, 2018, 10(6), 2774–2780.

128 G. Zou, et al., Metal–organic framework-derived materials for sodium energy storage, Small, 2018, 14(3), 1702648.

129 J.-Y. Hwang, S.-T. Myung and Y.-K. Sun, Sodium-ion batteries: present and future, Chem. Soc. Rev., 2017, 46(12), 3529–3614.

130 P. Adelhelm, et al., From lithium to sodium: cell chemistry of room temperature sodium–air and sodium–sulfur batteries, Beilstein J. Nanotechnol., 2015, 6(1), 1016–1055.

131 K. Chayambuka, *et al.*, Sodium-ion battery materials and electrochemical properties reviewed, *Adv. Energy Mater.*, 2018, **8**(16), 1800079.

132 L. Wang, *et al.*, Rhombohedral Prussian white as cathode for rechargeable sodium-ion batteries, *J. Am. Chem. Soc.*, 2015, **137**(7), 2548–2554.

133 Y. Park, *et al.*, Sodium terephthalate as an organic anode material for sodium ion batteries, *Adv. Mater.*, 2012, **24**(26), 3562–3567.

134 L. Wang, *et al.*, A superior low-cost cathode for a Na–ion battery, *Angew. Chem., Int. Ed.*, 2013, **52**(7), 1964–1967.

135 X. Zhang, *et al.*, Metal–organic framework derived porous CuO/Cu_2O composite hollow octahedrons as high performance anode materials for sodium ion batteries, *Chem. Commun.*, 2015, **51**(91), 16413–16416.

136 Y. Yue, *et al.*, Mesoporous prussian blue analogues: template-free synthesis and sodium-ion battery applications, *Angew. Chem., Int. Ed.*, 2014, **53**(12), 3134–3137.

137 J. Park, *et al.*, Stabilization of hexaaminobenzene in a 2D conductive metal–organic framework for high power sodium storage, *J. Am. Chem. Soc.*, 2018, **140**(32), 10315–10323.

138 X. Zhang, *et al.*, Porous $CoFe_2O_4$ nanocubes derived from metal–organic frameworks as high-performance anode for sodium ion batteries, *J. Colloid Interface Sci.*, 2017, **499**, 145–150.

139 Y. Guo, *et al.*, $MgFe_2O_4$ hollow microboxes derived from metal–organic-frameworks as anode material for sodium-ion batteries, *Mater. Lett.*, 2017, **199**, 101–104.

140 Y. V. Kaneti, *et al.*, Fabrication of an MOF-derived heteroatom-doped Co/CoO/carbon hybrid with superior sodium storage performance for sodium-ion batteries, *J. Mater. Chem. A*, 2017, **5**(29), 15356–15366.

141 G. Zou, *et al.*, Cube-shaped porous carbon derived from MOF-5 as advanced material for sodium-ion batteries, *Electrochim. Acta*, 2016, **196**, 413–421.

142 X. Ge, Z. Li and L. Yin, Metal–organic frameworks derived porous core/shellCoP@ C polyhedrons anchored on 3D reduced graphene oxide networks as anode for sodium-ion battery, *Nano Energy*, 2017, **32**, 117–124.

143 Y. Zhang, *et al.*, Nitrogen-doped yolk–shell-structured CoSe/C dodecahedra for high-performance sodium ion batteries, *ACS Appl. Mater. Interfaces*, 2017, **9**(4), 3624–3633.

144 K.-N. Jung, *et al.*, Rechargeable lithium–air batteries: a perspective on the development of oxygen electrodes, *J. Mater. Chem. A*, 2016, **4**(37), 14050–14068.

145 P. Tan, *et al.*, Advances and challenges in lithium-air batteries, *Appl. Energy*, 2017, **204**, 780–806.

146 D. Wu, *et al.*, Metal–organic frameworks as cathode materials for $Li–O_2$ batteries, *Adv. Mater.*, 2014, **26**(20), 3258–3262.

147 X. Mu, *et al.*, Using a Heme-Based Nanozyme as Bifunctional Redox Mediator for $Li–O_2$ Batteries, *Batteries Supercaps*, 2020, **3**(4), 336–340.

148 B. D. McCloskey, *et al.*, Solvents' critical role in nonaqueous lithium–oxygen battery electrochemistry, *J. Phys. Chem. Lett.*, 2011, **2**(10), 1161–1166.

149 B. Liu, *et al.*, Stabilization of Li metal anode in DMSO-based electrolytes via optimization of salt–solvent coordination for $Li–O_2$ batteries, *Adv. Energy Mater.*, 2017, **7**(14), 1602605.

150 M. Yuan, *et al.*, Ultrathin two-dimensional metal–organic framework nanosheets with the inherent open active sites as electrocatalysts in aprotic $Li–O_2$ batteries, *ACS Appl. Mater. Interfaces*, 2019, **11**(12), 11403–11413.

151 W. Yan, *et al.*, Downsizing metal–organic frameworks with distinct morphologies as cathode materials for high-capacity $Li–O_2$ batteries, *Mater. Chem. Front.*, 2017, **1**(7), 1324–1330.

152 J. Read, Ether-based electrolytes for the lithium/oxygen organic electrolyte battery, *J. Electrochem. Soc.*, 2005, **153**(1), A96.

153 M. Mao, *et al.*, Charge storage mechanism of MOF-derived Mn_2O_3 as high performance cathode of aqueous zinc–ion batteries, *J. Energy Chem.*, 2021, **52**, 277–283.

154 G. Yuan, *et al.*, Two-dimensional CuO nanosheets-induced MOF composites and derivatives for dendrite-free zinc–ion batteries, *Nano Res.*, 2023, **16**(5), 6881–6889.

155 Y. Ren, *et al.*, Fabrication of copper-cobalt heterostructures confined inside N-doped carbon nanocages for long-lasting Zn-air batteries, *J. Power Sources*, 2022, **545**, 231908.

156 G. Fang, *et al.*, Recent advances in aqueous zinc–ion batteries, *ACS Energy Lett.*, 2018, **3**(10), 2480–2501.

157 K. W. Nam, *et al.*, Conductive 2D metal–organic framework for high-performance cathodes in aqueous rechargeable zinc batteries, *Nat. Commun.*, 2019, **10**(1), 4948.

158 Z. Hu, Y. Chen and J. Jiang, Zeolitic imidazolate framework-8 as a reverse osmosis membrane for water desalination: insight from molecular simulation, *J. Chem. Phys.*, 2011, **134**(13), 134705.

159 K. Sun, *et al.*, Oxygen vacancies enriched MOF-derived MnO/C hybrids for high-performance aqueous zinc ion battery, *J. Alloys Compd.*, 2022, **923**, 166470.

160 D. Jia, *et al.*, Manganese-based metal–organic-framework derived hydrophilic cathode with carbon nanotubes introduced for long-life and high-performance aqueous zinc–ion battery, *J. Alloys Compd.*, 2022, **910**, 164876.

161 X. Pu, *et al.*, High-performance aqueous zinc-ion batteries realized by MOF materials, *Nano-Micro Lett.*, 2020, **12**, 1–15.

162 X. Luo, *et al.*, Understanding of the electrochemical behaviors of aqueous zinc–manganese batteries: reaction processes and failure mechanisms, *Green Energy Environ.*, 2022, **7**(5), 858–899.

163 C. Li, *et al.*, An ultra-high endurance and high-performance quasi-solid-state fiber-shaped $Zn–Ag_2O$ battery to harvest wind energy, *J. Mater. Chem. A*, 2019, **7**(5), 2034–2040.

164 K. Sun, *et al.*, MOF-derived Zn/Co co-doped MnO/C microspheres as cathode and Ti_3C_2@Zn as anode for aqueous zinc–ion full battery, *Chem. Eng. J.*, 2023, **454**, 140394.

165 C. A. Laska, *et al.*, Effect of hydrogen carbonate and chloride on zinc corrosion investigated by a scanning flow cell system, *Electrochim. Acta*, 2015, **159**, 198–209.

166 Z. Sang, *et al.*, One-dimensional π–d conjugated conductive metal–organic framework with dual redox-active sites for high-capacity and durable cathodes for aqueous zinc batteries, *ACS Nano*, 2023, **17**(3), 3077–3087.

167 C. Li, *et al.*, Conductive flower-like Ni–PTA–Mn as cathode for aqueous zinc–ion batteries, *J. Alloys Compd.*, 2021, **882**, 160587.

168 B. He, *et al.*, Self-sacrificed synthesis of conductive vanadium-based metal–organic framework nanowire-bundle arrays as binder-free cathodes for high-rate and high-energy-density wearable Zn–ion batteries, *Nano Energy*, 2019, **64**, 103935.

169 D. Linde and T. B. Reddy, *Handbooks of batteries*, McGraw-Hill Newyork, 2001.

170 G. Toussaint, *et al.*, Development of a rechargeable zinc–air battery, *ECS Trans.*, 2010, **28**(32), 25.

171 W. Zhu, *et al.*, New structures of thin air cathodes for zinc–air batteries, *J. Appl. Electrochem.*, 2003, **33**, 29–36.

172 T. Dirkse and D. Kroon, Effect of ionic strength on the passivation of zinc electrodes in KOH solutions, *J. Appl. Electrochem.*, 1971, **1**(4), 293–296.

173 A. Franco, *et al.*, A 2D copper-imidazolate framework without thermal treatment as an efficient ORR electrocatalyst for Zn–air batteries, *J. Mater. Chem. A*, 2022, **10**(46), 24590–24597.

174 J. S. Lee, *et al.*, Metal–air batteries with high energy density: Li–air versus Zn–air, *Adv. Energy Mater.*, 2011, **1**(1), 34–50.

175 C. Guan, *et al.*, Decorating Co/CoN$_x$ nanoparticles in nitrogen-doped carbon nanoarrays for flexible and rechargeable zinc–air batteries, *Energy Storage Mater.*, 2019, **16**, 243–250.

176 W. Li, *et al.*, Core–Shell Carbon-Based Bifunctional Electrocatalysts Derived from COF@ MOF Hybrid for Advanced Rechargeable Zn–Air Batteries, *Small*, 2022, **18**(31), 2202018.

177 H. Zheng, *et al.*, Mn, N co-doped Co nanoparticles/porous carbon as air cathode for highly efficient rechargeable Zn–air batteries, *Nano Res.*, 2022, 1–7.

178 S. Agarwal, X. Yu and A. Manthiram, A pair of metal organic framework (MOF)-derived oxygen reduction reaction (ORR) and oxygen evolution reaction (OER) catalysts for zinc–air batteries, *Mater. Today Energy*, 2020, **16**, 100405.

179 H. Wang, *et al.*, Accelerating Triple Transport in Zinc-Air Batteries and Water Electrolysis by Spatially Confining Co Nanoparticles in Breathable Honeycomb-Like Macroporous N-Doped Carbon, *Small*, 2021, **17**(49), 2103517.

180 X. Duan, *et al.*, MOF-derived Co-MOF, O-doped carbon as trifunctional electrocatalysts to enable highly efficient Zn–air batteries and water-splitting, *J. Energy Chem.*, 2021, **56**, 290–298.

181 N. Pan, *et al.*, Conductive MOFs as bifunctional oxygen electrocatalysts for all-solid-state Zn–air batteries, *Chem. Commun.*, 2020, **56**(88), 13615–13618.

182 J. Li, *et al.*, Three-dimensional hierarchical conductive metal–organic frameworks/NiFe layered double hydroxide/carbon nanofibers: an efficient oxygen evolution reaction catalyst for Zn–air batteries, *Inorg. Chem. Front.*, 2022, **9**(20), 5335–5346.

183 A. Ponrouch, *et al.*, Towards a calcium-based rechargeable battery, *Nat. Mater.*, 2016, **15**(2), 169–172.

184 D. Monti, *et al.*, Multivalent batteries—prospects for high energy density: Ca batteries, *Front. Chem.*, 2019, **7**, 79.

185 P. Padigi, *et al.*, Potassium barium hexacyanoferrate–a potential cathode material for rechargeable calcium ion batteries, *J. Power Sources*, 2015, **273**, 460–464.

186 R. Cohen, Y. Lavi and E. Peled, Calorimetric Study of the Calcium/Sr(AlCl$_4$)$_2$-SOCl$_2$ Battery, *J. Electrochem. Soc.*, 1990, **137**(9), 2648.

187 B. Ji, *et al.*, Recent advances and perspectives on calcium–ion storage: key materials and devices, *Adv. Mater.*, 2021, **33**(2), 2005501.

188 M. E. Purbarani, J. Hyoung and S.-T. Hong, Crystal-water-free potassium vanadium bronze (K$_{0.5}$V$_2$O$_5$) as a cathode material for Ca–ion batteries, *ACS Appl. Energy Mater.*, 2021, **4**(8), 7487–7491.

189 T. N. Vo, *et al.*, Ultra-stable calcium ion batteries with Prussian blue nanodisks, *EcoMat*, 2023, **5**(2), e12285.

190 Z. Song, *et al.*, Origin of the high oxygen reduction reaction of nitrogen and sulfur co-doped MOF-derived nanocarbon electrocatalysts, *Mater. Horiz.*, 2017, **4**(5), 900–907.

191 Y. Ren, G. H. Chia and Z. Gao, Metal–organic frameworks in fuel cell technologies, *Nano Today*, 2013, **8**(6), 577–597.

192 G. E. Fenoy, *et al.*, Powering up the oxygen reduction reaction through the integration of O$_2$-adsorbing metal–organic frameworks on nanocomposite electrodes, *ACS Appl. Energy Mater.*, 2018, **1**(10), 5428–5436.

193 S. Bureekaew, *et al.*, One-dimensional imidazole aggregate in aluminium porous coordination polymers with high proton conductivity, *Nat. Mater.*, 2009, **8**(10), 831–836.

194 D. Gui, *et al.*, Unique proton transportation pathway in a robust inorganic coordination polymer leading to intrinsically high and sustainable anhydrous proton conductivity, *J. Am. Chem. Soc.*, 2018, **140**(19), 6146–6155.

195 J. M. Taylor, *et al.*, The role of a three dimensionally ordered defect sublattice on the acidity of a sulfonated metal–organic framework, *J. Am. Chem. Soc.*, 2015, **137**(35), 11498–11506.

196 D. Ji, *et al.*, Thin MoS$_2$ nanosheets grafted MOFs-derived porous Co–N–C flakes grown on electrospun carbon nanofibers as self-supported bifunctional catalysts for overall water splitting, *J. Mater. Chem. A*, 2017, **5**(45), 23898–23908.

197 W. Yang, *et al.*, A metal–organic framework devised Co–N doped carbon microsphere/nanofiber hybrid as a freestanding 3D oxygen catalyst, *Chem. Commun.*, 2017, **53**(28), 4034–4037.

198 C. Liu, *et al.*, Electrospun ZIF-based hierarchical carbon fiber as an efficient electrocatalyst for the oxygen reduction reaction, *J. Mater. Chem. A*, 2017, **5**(3), 1211–1220.

199 X.-Y. Dong, *et al.*, Synergy between isomorphous acid and basic metal–organic frameworks for anhydrous proton conduction of low-cost hybrid membranes at high
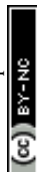
temperatures, *ACS Appl. Mater. Interfaces*, 2018, **10**(44), 38209–38216.

200 Y. Guo, *et al.*, Zwitterion threaded metal–organic framework membranes for direct methanol fuel cells, *J. Mater. Chem. A*, 2018, **6**(40), 19547–19554.

201 H. Chen, *et al.*, High conductive, long-term durable, anhydrous proton conductive solid-state electrolyte based on a metal–organic framework impregnated with binary ionic liquids: synthesis, characteristic and effect of anion, *J. Power Sources*, 2018, **376**, 168–176.

202 M. Sadakiyo, T. Yamada and H. Kitagawa, Rational designs for highly proton-conductive metal– organic frameworks, *J. Am. Chem. Soc.*, 2009, **131**(29), 9906–9907.

203 Q.-L. Zhu and Q. Xu, Metal–organic framework composites, *Chem. Soc. Rev.*, 2014, **43**(16), 5468–5512.

204 S. Rojas and P. Horcajada, Metal–organic frameworks for the removal of emerging organic contaminants in water, *Chem. Rev.*, 2020, **120**(16), 8378–8415.

205 H. Zhang, *et al.*, Metal–organic-framework-based materials as platforms for renewable energy and environmental applications, *Joule*, 2017, **1**(1), 77–107.

206 B. M. Connolly, *et al.*, Shaping the future of fuel: monolithic metal–organic frameworks for high-density gas storage, *J. Am. Chem. Soc.*, 2020, **142**(19), 8541–8549.

207 G. Yilmaz, *et al.*, Atomic-and Molecular-Level Design of Functional Metal–Organic Frameworks (MOFs) and Derivatives for Energy and Environmental Applications, *Adv. Sci.*, 2019, **6**(21), 1901129.

208 C. Byrne, G. Subramanian and S. C. Pillai, Recent advances in photocatalysis for environmental applications, *J. Environ. Chem. Eng.*, 2018, **6**(3), 3531–3555.

209 M. Rafatullah, *et al.*, Adsorption of methylene blue on low-cost adsorbents: a review, *J. Hazard. Mater.*, 2010, **177**(1–3), 70–80.

210 S.-H. Huo and X.-P. Yan, Metal–organic framework MIL-100(Fe) for the adsorption of malachite green from aqueous solution, *J. Mater. Chem.*, 2012, **22**(15), 7449–7455.

211 X.-X. Huang, *et al.*, Hierarchically mesostructured MIL-101 metal–organic frameworks: supramolecular template-directed synthesis and accelerated adsorption kinetics for dye removal, *CrystEngComm*, 2012, **14**(5), 1613–1617.

212 L. Li, *et al.*, A MOF/graphite oxide hybrid (MOF: HKUST-1) material for the adsorption of methylene blue from aqueous solution, *J. Mater. Chem. A*, 2013, **1**(35), 10292–10299.

213 D. Liu, *et al.*, Three-Dimensional Metal– Organic Frameworks Based on Tetrahedral and Square-Planar Building Blocks: Hydrogen Sorption and Dye Uptake Studies, *Inorg. Chem.*, 2010, **49**(20), 9107–9109.

214 S. Dadfarnia, *et al.*, Methyl red removal from water by iron based metal–organic frameworks loaded onto iron oxide nanoparticle adsorbent, *Appl. Surf. Sci.*, 2015, **330**, 85–93.

215 E. Haque, *et al.*, Adsorptive removal of methyl orange from aqueous solution with metal–organic frameworks, porous chromium–benzenedicarboxylates, *J. Hazard. Mater.*, 2010, **181**(1–3), 535–542.

216 Q. Yang, *et al.*, Selective separation of methyl orange from water using magnetic ZIF-67 composites, *Chem. Eng. J.*, 2018, **333**, 49–57.

217 K. Wang, *et al.*, Rational construction of defects in a metal–organic framework for highly efficient adsorption and separation of dyes, *Chem. Eng. J.*, 2016, **289**, 486–493.

218 K.-Y. A. Lin and H.-A. Chang, Ultra-high adsorption capacity of zeolitic imidazole framework-67 (ZIF-67) for removal of malachite green from water, *Chemosphere*, 2015, **139**, 624–631.

219 R. Qin and H. C. Zeng, Design and synthesis of supported nanoscale metal–organic frameworks: transformation from transition metal silicates, *ACS Sustainable Chem. Eng.*, 2018, **6**(11), 14979–14988.

220 T. Wang, *et al.*, Adsorption removal of organic dyes on covalent triazine framework (CTF), *Microporous Mesoporous Mater.*, 2014, **187**, 63–70.

221 E. Haque, J. W. Jun and S. H. Jhung, Adsorptive removal of methyl orange and methylene blue from aqueous solution with a metal–organic framework material, iron terephthalate (MOF-235), *J. Hazard. Mater.*, 2011, **185**(1), 507–511.

222 E. Haque, *et al.*, Dichotomous adsorption behaviour of dyes on an amino-functionalised metal–organic framework, amino-MIL-101(Al), *J. Mater. Chem. A*, 2014, **2**(1), 193–203.

223 Y. Zhou, *et al.*, An anionic single-walled metal–organic nanotube with an armchair (3, 3) topology as an extremely smart adsorbent for the effective and selective adsorption of cationic carcinogenic dyes, *Chem. Commun.*, 2018, **54**(24), 3006–3009.

224 C. Li, *et al.*, The strengthening role of the amino group in metal–organic framework MIL-53(Al) for methylene blue and malachite green dye adsorption, *J. Chem. Eng. Data*, 2015, **60**(11), 3414–3422.

225 S. Seth, G. Savitha and J. N. Moorthy, Diverse isostructural MOFs by postsynthetic metal node metathesis: anionic-to-cationic framework conversion, luminescence and separation of dyes, *J. Mater. Chem. A*, 2015, **3**(45), 22915–22922.

226 M. J. Dong, *et al.*, A luminescent dye@ MOF platform: emission fingerprint relationships of volatile organic molecules, *Angew. Chem.*, 2014, **126**(6), 1601–1605.

227 S. Luo and J. Wang, MOF/grasphene oxide composite as an efficient adsorbent for the removal of organic dyes from aqueous solution, *Environ. Sci. Pollut. Res.*, 2018, **25**, 5521–5528.

228 J. Abdi, *et al.*, Synthesis of metal–organic framework hybrid nanocomposites based on GO and CNT with high adsorption capacity for dye removal, *Chem. Eng. J.*, 2017, **326**, 1145–1158.

229 L. Li, *et al.*, The adsorption on magnetic hybrid Fe_3O_4/HKUST-1/GO of methylene blue from water solution, *J. Mater. Chem. A*, 2014, **2**(6), 1795–1801.

230 R. Pei, *et al.*, 3D-Printed metal–organic frameworks within biocompatible polymers as excellent adsorbents for organic dyes removal, *J. Hazard. Mater.*, 2020, **384**, 121418.

231 J. Hu, *et al.*, Enhanced adsorptive removal of hazardous anionic dye "congo red" by a Ni/Cu mixed-component

metal–organic porous material, *RSC Adv.*, 2014, **4**(66), 35124–35130.

232 M. Y. Masoomi, M. Bagheri and A. Morsali, Porosity and dye adsorption enhancement by ultrasonic synthesized Cd(II) based metal–organic framework, *Ultrason. Sonochem.*, 2017, **37**, 244–250.

233 M. Yang and Q. Bai, Flower-like hierarchical Ni-Zn MOF microspheres: efficient adsorbents for dye removal, *Colloids Surf., A*, 2019, **582**, 123795.

234 J. Liu, H. Yu and L. Wang, Superior absorption capacity of tremella like ferrocene based metal–organic framework in removal of organic dye from water, *J. Hazard. Mater.*, 2020, **392**, 122274.

235 J.-M. Yang, *et al.*, Rapid adsorptive removal of cationic and anionic dyes from aqueous solution by a Ce(III)-doped Zr-based metal–organic framework, *Microporous Mesoporous Mater.*, 2020, **292**, 109764.

236 N. Chen, *et al.*, Effect of structures on the adsorption performance of Cobalt Metal Organic Framework obtained by microwave-assisted ball milling, *Chem. Phys. Lett.*, 2018, **705**, 23–30.

237 H. Molavi, *et al.*, Selective dye adsorption by highly water stable metal–organic framework: long term stability analysis in aqueous media, *Appl. Surf. Sci.*, 2018, **445**, 424–436.

238 J. Zhang, F. Li and Q. Sun, Rapid and selective adsorption of cationic dyes by a unique metal–organic framework with decorated pore surface, *Appl. Surf. Sci.*, 2018, **440**, 1219–1226.

239 L. Huang, *et al.*, Magnetic Zr-MOFs nanocomposites for rapid removal of heavy metal ions and dyes from water, *Chemosphere*, 2018, **199**, 435–444.

240 S. Aslam, *et al.*, In situ one-step synthesis of Fe₃O₄@MIL-100(Fe) core-shells for adsorption of methylene blue from water, *J. Colloid Interface Sci.*, 2017, **505**, 186–195.

241 J.-M. Yang, A facile approach to fabricate an immobilized-phosphate zirconium-based metal–organic framework composite (UiO-66-P) and its activity in the adsorption and separation of organic dyes, *J. Colloid Interface Sci.*, 2017, **505**, 178–185.

242 F. Tan, *et al.*, Facile synthesis of size-controlled MIL-100(Fe) with excellent adsorption capacity for methylene blue, *Chem. Eng. J.*, 2015, **281**, 360–367.

243 Y. Shao, *et al.*, Magnetic responsive metal–organic frameworks nanosphere with core–shell structure for highly efficient removal of methylene blue, *Chem. Eng. J.*, 2016, **283**, 1127–1136.

244 X. Liu, *et al.*, Removal of methylene blue from aqueous solutions by an adsorbent based on metal–organic framework and polyoxometalate, *J. Alloys Compd.*, 2015, **648**, 986–993.

245 M. S. Tehrani and R. Zare-Dorabei, Highly efficient simultaneous ultrasonic-assisted adsorption of methylene blue and rhodamine B onto metal organic framework MIL-68(Al): central composite design optimization, *RSC Adv.*, 2016, **6**(33), 27416–27425.

246 Q. Yang, *et al.*, An anionic In(III)-based metal–organic framework with Lewis basic sites for the selective

adsorption and separation of organic cationic dyes, *Chin. Chem. Lett.*, 2019, **30**(1), 234–238.

247 X. Song, *et al.*, Facile synthesis of metal–organic framework UiO-66 for adsorptive removal of methylene blue from water, *Chem. Phys.*, 2020, **531**, 110655.

248 M. D. Firouzjaei, *et al.*, Experimental and molecular dynamics study on dye removal from water by a graphene oxide–copper–metal organic framework nanocomposite, *J. Water Process Eng.*, 2020, **34**, 101180.

249 V. D. Doan, *et al.*, Utilization of waste plastic pet bottles to prepare copper-1, 4-benzenedicarboxylate metal–organic framework for methylene blue removal, *Sep. Sci. Technol.*, 2020, **55**(3), 444–455.

250 B. Li, *et al.*, Dyes encapsulated in a novel flexible metal–organic framework show tunable and stimuli-responsive phosphorescence, *Dyes Pigm.*, 2020, **174**, 108017.

251 B. Sherino, *et al.*, Simultaneous removal of carcinogenic anionic and cationic dyes from environmental water using a new Zn-based metal–organic framework, *Sep. Sci. Technol.*, 2021, **56**(2), 330–343.

252 H. Guo, *et al.*, Metal–organic framework MIL-125(Ti) for efficient adsorptive removal of Rhodamine B from aqueous solution, *Appl. Organomet. Chem.*, 2015, **29**(1), 12–19.

253 H. Tian, *et al.*, Preparation and performance study of MgFe₂O₄/metal–organic framework composite for rapid removal of organic dyes from water, *J. Solid State Chem.*, 2018, **257**, 40–48.

254 L. Zeng, *et al.*, Trichloroacetic acid-modulated synthesis of polyoxometalate@UiO-66 for selective adsorption of cationic dyes, *J. Colloid Interface Sci.*, 2018, **516**, 274–283.

255 H. Liu, X. Ren and L. Chen, Synthesis and characterization of magnetic metal–organic framework for the adsorptive removal of Rhodamine B from aqueous solution, *J. Ind. Eng. Chem.*, 2016, **34**, 278–285.

256 C. Yang, *et al.*, Indium-based metal–organic framework/graphite oxide composite as an efficient adsorbent in the adsorption of rhodamine B from aqueous solution, *J. Alloys Compd.*, 2016, **687**, 804–812.

257 S.-Q. Deng, *et al.*, Hydrolytically stable nanotubular cationic metal–organic framework for rapid and efficient removal of toxic oxo-anions and dyes from water, *Inorg. Chem.*, 2019, **58**(4), 2899–2909.

258 S. A. Sadat, *et al.*, Rapid room-temperature synthesis of cadmium zeolitic imidazolate framework nanoparticles based on 1,1′-carbonyldiimidazole as ultra-high-efficiency adsorbent for ultrasound-assisted removal of malachite green dye, *Appl. Surf. Sci.*, 2019, **467**, 1204–1212.

259 N. M. Mahmoodi, *et al.*, Synthesis of pearl necklace-like ZIF-8@ chitosan/PVA nanofiber with synergistic effect for recycling aqueous dye removal, *Carbohydr. Polym.*, 2020, **227**, 115364.

260 M. Trukawka, *et al.*, Carbonized metal–organic frameworks with trapped cobalt nanoparticles as biocompatible and efficient azo-dye adsorbent, *Environ. Sci. Eur.*, 2019, **31**(1), 1–15.
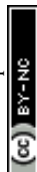
261 L.-W. Lee, *et al.*, Membrane adsorber containing a new Sm(III)–organic framework for dye removal, *Environ. Sci.: Nano*, 2019, **6**(4), 1067–1076.

262 X. Liu, *et al.*, Highly effective and fast removal of anionic carcinogenic dyes via an In 3-cluster-based cationic metal–organic framework with nitrogen-rich ligand, *Mater. Chem. Front.*, 2020, **4**(1), 182–188.

263 P. A. Kobielska, *et al.*, Metal–organic frameworks for heavy metal removal from water, *Coord. Chem. Rev.*, 2018, **358**, 92–107.

264 Y. Gu, *et al.*, Facile fabrication of composition-tunable Fe/Mg bimetal–organic frameworks for exceptional arsenate removal, *Chem. Eng. J.*, 2019, **357**, 579–588.

265 A. M. Nasir, *et al.*, Application of two-dimensional leaf-shaped zeolitic imidazolate framework (2D ZIF-L) as arsenite adsorbent: kinetic, isotherm and mechanism, *J. Mol. Liq.*, 2018, **250**, 269–277.

266 F. Ke, *et al.*, Highly selective removal of Hg^{2+} and Pb^{2+} by thiol-functionalized $Fe_3O_4@$ metal–organic framework core-shell magnetic microspheres, *Appl. Surf. Sci.*, 2017, **413**, 266–274.

267 M. Jaishankar, *et al.*, Toxicity, mechanism and health effects of some heavy metals, *Interdiscip. Toxicol.*, 2014, **7**(2), 60.

268 C. Wang, *et al.*, Superior removal of arsenic from water with zirconium metal–organic framework UiO-66, *Sci. Rep.*, 2015, **5**(1), 16613.

269 A. Sherlala, *et al.*, A review of the applications of organo-functionalized magnetic graphene oxide nanocomposites for heavy metal adsorption, *Chemosphere*, 2018, **193**, 1004–1017.

270 A. Sarkar and B. Paul, The global menace of arsenic and its conventional remediation-A critical review, *Chemosphere*, 2016, **158**, 37–49.

271 B.-J. Zhu, *et al.*, Iron and 1,3,5-benzenetricarboxylic metal–organic coordination polymers prepared by solvothermal method and their application in efficient As(V) removal from aqueous solutions, *J. Phys. Chem. C*, 2012, **116**(15), 8601–8607.

272 J.-B. Huo, *et al.*, Direct epitaxial synthesis of magnetic $Fe_3O_4@$UiO-66 composite for efficient removal of arsenate from water, *Microporous Mesoporous Mater.*, 2019, **276**, 68–75.

273 L. Li, Y. Xu and D. Zhong, Highly efficient adsorption and reduction of Cr(VI) ions by a core–shell $Fe_3O_4@$UiO-66@PANI composite, *J. Phys. Chem. A*, 2020, **124**(14), 2854–2862.

274 Z.-M. Liu, *et al.*, Novel hematite nanorods and magnetite nanoparticles prepared from MIL-100(Fe) template for the removal of As(V), *Mater. Lett.*, 2014, **132**, 8–10.

275 S. Hei, Y. Jin and F. Zhang, Fabrication of γ-Fe_3O_4 nanoparticles by solid-state thermolysis of a metal–organic framework, MIL-100(Fe), for heavy metal ions removal, *J. Chem.*, 2014, **2014**, DOI: 10.1155/2014/546956.

276 Y.-N. Wu, *et al.*, Amino acid assisted templating synthesis of hierarchical zeolitic imidazolate framework-8

277 B. Liu, *et al.*, Highly efficient removal of arsenic(III) from aqueous solution by zeolitic imidazolate frameworks with different morphology, *Colloids Surf., A*, 2015, **481**, 358–366.

278 M. Jian, *et al.*, Adsorptive removal of arsenic from aqueous solution by zeolitic imidazolate framework-8 (ZIF-8) nanoparticles, *Colloids Surf., A*, 2015, **465**, 67–76.

279 J. Li, *et al.*, Zeolitic imidazolate framework-8 with high efficiency in trace arsenate adsorption and removal from water, *J. Phys. Chem. C*, 2014, **118**(47), 27382–27387.

280 M. Massoudinejad, *et al.*, Ethylenediamine-functionalized cubic ZIF-8 for arsenic adsorption from aqueous solution: modeling, isotherms, kinetics and thermodynamics, *J. Mol. Liq.*, 2018, **255**, 263–268.

281 T. A. Vu, *et al.*, Arsenic removal from aqueous solutions by adsorption using novel MIL-53(Fe) as a highly efficient adsorbent, *RSC Adv.*, 2015, **5**(7), 5261–5268.

282 D. Xie, *et al.*, Bifunctional NH_2–MIL-88(Fe) metal–organic framework nanooctahedra for highly sensitive detection and efficient removal of arsenate in aqueous media, *J. Mater. Chem. A*, 2017, **5**(45), 23794–23804.

283 H. Wu, *et al.*, Arsenic removal from water by metal–organic framework MIL-88A microrods, *Environ. Sci. Pollut. Res.*, 2018, **25**, 27196–27202.

284 B. J. Abu Tarboush, *et al.*, Metal–organic framework-74 for ultratrace arsenic removal from water: experimental and density functional theory studies, *ACS Appl. Nano Mater.*, 2018, **1**(7), 3283–3292.

285 C. Zhang, *et al.*, A novel highly efficient adsorbent $\{[Co_4(L)_2(\mu_3\text{-OH})_2(H_2O)_3(4,4'\text{-bipy})_2](H_2O)_2\}_n$: synthesis, crystal structure, magnetic and arsenic(V) absorption capacity, *J. Solid State Chem.*, 2018, **261**, 22–30.

286 Z. Lv, *et al.*, MOFs-derived magnetic chestnut shell-like hollow sphere NiO/Ni@C composites and their removal performance for arsenic(V), *Chem. Eng. J.*, 2019, **362**, 413–421.

287 M. Gallegos-Garcia, K. Ramírez-Muñiz and S. Song, Arsenic removal from water by adsorption using iron oxide minerals as adsorbents: a review, *Miner. Process. Extr. Metall. Rev.*, 2012, **33**(5), 301–315.

288 S.-H. Ho, *et al.*, High-efficiency removal of lead from wastewater by biochar derived from anaerobic digestion sludge, *Bioresour. Technol.*, 2017, **246**, 142–149.

289 M. Ghorbani, O. Seyedin and M. Aghamohammadhassan, Adsorptive removal of lead(II) ion from water and wastewater media using carbon-based nanomaterials as unique sorbents: a review, *J. Environ. Manage.*, 2020, **254**, 109814.

290 L. Meng, *et al.*, Lead removal from water by a newly isolated Geotrichum candidum LG-8 from Tibet kefir milk and its mechanism, *Chemosphere*, 2020, **259**, 127507.

291 X.-X. Qiao, *et al.*, Highly efficient and selective removal of lead ions from aqueous solutions by conjugated microporous polymers with functionalized heterogeneous pores, *Cryst. Growth Des.*, 2019, **20**(1), 337–344.

292 M. R. Awual, An efficient composite material for selective lead(II) monitoring and removal from wastewater, *J. Environ. Chem. Eng.*, 2019, **7**(3), 103087.

293 Y. Huang, *et al.*, Heavy metal ion removal of wastewater by zeolite-imidazolate frameworks, *Sep. Purif. Technol.*, 2018, **194**, 462–469.

294 X. Luo, L. Ding and J. Luo, Adsorptive removal of Pb(II) ions from aqueous samples with amino-functionalization of metal–organic frameworks MIL-101(Cr), *J. Chem. Eng. Data*, 2015, **60**(6), 1732–1743.

295 G. Li, *et al.*, Amide-based covalent organic frameworks materials for efficient and recyclable removal of heavy metal lead(II), *Chem. Eng. J.*, 2019, **370**, 822–830.

296 J. M. Rivera, *et al.*, Highly efficient adsorption of aqueous Pb(II) with mesoporous metal–organic framework-5: an equilibrium and kinetic study, *J. Nanomater.*, 2016, **2016**, DOI: 10.1155/2016/8095737.

297 C.-X. Yu, *et al.*, Highly efficient and facile removal of Pb^{2+} from water by using a negatively charged azoxy-functionalized metal–organic framework, *Cryst. Growth Des.*, 2020, **20**(8), 5251–5260.

298 Z. S. Hasankola, R. Rahimi and V. Safarifard, Rapid and efficient ultrasonic-assisted removal of lead(II) in water using two copper-and zinc-based metal–organic frameworks, *Inorg. Chem. Commun.*, 2019, **107**, 107474.

299 Y. Wang, *et al.*, Metal–organic framework modified carbon paste electrode for lead sensor, *Sens. Actuators, B*, 2013, **177**, 1161–1166.

300 J. Zhang, *et al.*, Exploring a thiol-functionalized MOF for elimination of lead and cadmium from aqueous solution, *J. Mol. Liq.*, 2016, **221**, 43–50.

301 C. Yu, Z. Shao and H. Hou, A functionalized metal–organic framework decorated with O$^-$ groups showing excellent performance for lead(II) removal from aqueous solution, *Chem. Sci.*, 2017, **8**(11), 7611–7619.

302 Q. Qin, *et al.*, An efficient approach for Pb(II) and Cd(II) removal using manganese dioxide formed in situ, *Chem. Eng. J.*, 2011, **172**(1), 68–74.

303 N. Yin, K. Wang and Z. Li, Novel melamine modified metal–organic frameworks for remarkably high removal of heavy metal Pb(II), *Desalination*, 2018, **430**, 120–127.

304 A. Abbasi, T. Moradpour and K. Van Hecke, A new 3D cobalt(II) metal–organic framework nanostructure for heavy metal adsorption, *Inorg. Chim. Acta*, 2015, **430**, 261–267.

305 R. Ricco, *et al.*, Lead(II) uptake by aluminium based magnetic framework composites (MFCs) in water, *J. Mater. Chem. A*, 2015, **3**(39), 19822–19831.

306 D. T. Sun, *et al.*, Rapid, selective heavy metal removal from water by a metal–organic framework/polydopamine composite, *ACS Cent. Sci.*, 2018, **4**(3), 349–356.

307 A. Chakraborty, *et al.*, Post-synthetic metalation in an anionic MOF for efficient catalytic activity and removal of heavy metal ions from aqueous solution, *Chem. Commun.*, 2016, **52**(13), 2831–2834.

308 K. Shekhawat, S. Chatterjee and B. Joshi, Chromium toxicity and its health hazards, *Int. J. Adv. Res.*, 2015, **3**(7), 167–172.

309 T. Sathvika, *et al.*, A co-operative endeavor by nitrifying bacteria Nitrosomonas and Zirconium based metal organic framework to remove hexavalent chromium, *Chem. Eng. J.*, 2019, **360**, 879–889.

310 H. Saleem, U. Rafique and R. P. Davies, Investigations on post-synthetically modified UiO-66-NH$_2$ for the adsorptive removal of heavy metal ions from aqueous solution, *Microporous Mesoporous Mater.*, 2016, **221**, 238–244.

311 Q. Zhang, *et al.*, A porous Zr-cluster-based cationic metal–organic framework for highly efficient Cr$_2$O$_7^{2-}$ removal from water, *Chem. Commun.*, 2015, **51**(79), 14732–14734.

312 E. Tahmasebi, *et al.*, Application of mechanosynthesized azine-decorated zinc(II) metal–organic frameworks for highly efficient removal and extraction of some heavy-metal ions from aqueous samples: a comparative study, *Inorg. Chem.*, 2015, **54**(2), 425–433.

313 Z. Noraee, *et al.*, Use of metal–organic framework to remove chromium(VI) from aqueous solutions, *J. Environ. Health Sci. Eng.*, 2019, **17**, 701–709.

314 Q. Yang, *et al.*, Fabrication of core–shell Fe$_3$O$_4$@MIL-100(Fe) magnetic microspheres for the removal of Cr(VI) in aqueous solution, *J. Solid State Chem.*, 2016, **244**, 25–30.

315 L. Aboutorabi, *et al.*, Metal–organic framework based on isonicotinate N-oxide for fast and highly efficient aqueous phase Cr(VI) adsorption, *Inorg. Chem.*, 2016, **55**(11), 5507–5513.

316 J. Guo, J.-J. Li and C.-C. Wang, Adsorptive removal of Cr(VI) from simulated wastewater in MOF BUC-17 ultrafine powder, *J. Environ. Chem. Eng.*, 2019, **7**(1), 102909.

317 H. Fei, *et al.*, A cationic metal–organic solid solution based on Co(II) and Zn(II) for chromate trapping, *Chem. Mater.*, 2013, **25**(5), 647–652.

318 A. Maleki, *et al.*, Adsorption of hexavalent chromium by metal organic frameworks from aqueous solution, *J. Ind. Eng. Chem.*, 2015, **28**, 211–216.

319 X. Li, *et al.*, Mechanistic insight into the interaction and adsorption of Cr(VI) with zeolitic imidazolate framework-67 microcrystals from aqueous solution, *Chem. Eng. J.*, 2015, **274**, 238–246.

320 L.-L. Li, *et al.*, Cr(VI) removal via anion exchange on a silver-triazolate MOF, *J. Hazard. Mater.*, 2017, **321**, 622–628.

321 S. Jamshidifard, *et al.*, Incorporation of UiO-66-NH$_2$ MOF into the PAN/chitosan nanofibers for adsorption and membrane filtration of Pb(II), Cd(II) and Cr(VI) ions from aqueous solutions, *J. Hazard. Mater.*, 2019, **368**, 10–20.

322 L. Huang, *et al.*, Portable colorimetric detection of mercury(II) based on a non-noble metal nanozyme with tunable activity, *Inorg. Chem.*, 2019, **58**(2), 1638–1646.

323 H. Lohren, *et al.*, Toxicity of organic and inorganic mercury species in differentiated human neurons and human astrocytes, *J. Trace Elem. Med. Biol.*, 2015, **32**, 200–208.

324 Y. Zhao, *et al.*, Environmental applications of diatomite minerals in removing heavy metals from water, *Ind. Eng. Chem. Res.*, 2019, **58**(27), 11638–11652.

325 S. Halder, *et al.*, A Ni-based MOF for selective detection and removal of Hg^{2+} in aqueous medium: a facile strategy, *Dalton Trans.*, 2017, **46**(6), 1943–1950.

326 F. Ke, *et al.*, Thiol-functionalization of metal–organic framework by a facile coordination-based postsynthetic strategy and enhanced removal of Hg^{2+} from water, *J. Hazard. Mater.*, 2011, **196**, 36–43.

327 A. E. Poste, *et al.*, Bioaccumulation and biomagnification of mercury in African lakes: the importance of trophic status, *Sci. Total Environ.*, 2015, **506**, 126–136.

328 L. Liang, *et al.*, Incorporation of In_2S_3 nanoparticles into a metal–organic framework for ultrafast removal of Hg from water, *Inorg. Chem.*, 2018, **57**(9), 4891–4897.

329 N. D. Rudd, *et al.*, Highly efficient luminescent metal–organic framework for the simultaneous detection and removal of heavy metals from water, *ACS Appl. Mater. Interfaces*, 2016, **8**(44), 30294–30303.

330 H. Yang, *et al.*, Three-dimensional macroporous Carbon/Zr-2,5-dimercaptoterephthalic acid metal–organic frameworks nanocomposites for removal and detection of Hg(II), *Sens. Actuators, B*, 2020, **320**, 128447.

331 W. H. Yin, *et al.*, Functionalizing a metal–organic framework by a photoassisted multicomponent postsynthetic modification approach showing highly effective Hg(II) removal, *Inorg. Chem.*, 2018, **57**(15), 8722–8725.

332 J. Li, *et al.*, Metal–organic framework-based materials: superior adsorbents for the capture of toxic and radioactive metal ions, *Chem. Soc. Rev.*, 2018, **47**(7), 2322–2356.

333 P. Zhou, *et al.*, Application of nanoparticles alleviates heavy metals stress and promotes plant growth: an overview, *Nanomaterials*, 2020, **11**(1), 26.

334 S. Kul, Removal of Cu(II) from aqueous solutions using modified sewage sludge ash, *Int. J. Environ. Sci. Technol.*, 2021, **18**(12), 3795–3806.

335 P. Senthil Kumar, C. Senthamarai and A. Durgadevi, Adsorption kinetics, mechanism, isotherm, and thermodynamic analysis of copper ions onto the surface modified agricultural waste, *Environ. Prog. Sustainable Energy*, 2014, **33**(1), 28–37.

336 S. Bagheri, *et al.*, Role of copper in the onset of Alzheimer's disease compared to other metals, *Front. Aging Neurosci.*, 2018, **9**, 446.

337 M. R. Awual, *et al.*, Trace copper(II) ions detection and removal from water using novel ligand modified composite adsorbent, *Chem. Eng. J.*, 2013, **222**, 67–76.

338 H. E. Patton, *The Effectiveness of Point-of-Use Treatment in Improving Home Drinking Water Quality in Rural Households*, Virginia Tech, 2023.

339 M. Yusuf, K. Song and L. Li, Fixed bed column and artificial neural network model to predict heavy metals adsorption dynamic on surfactant decorated graphene, *Colloids Surf., A*, 2020, **585**, 124076.

340 A. M. Ghaedi, *et al.*, Factorial experimental design for the optimization of highly selective adsorption removal of lead and copper ions using metal organic framework MOF-2(Cd), *J. Mol. Liq.*, 2018, **272**, 15–26.

341 K. Wang, Z. Tian and N. Yin, Significantly enhancing Cu(II) adsorption onto Zr-MOFs through novel cross-flow disturbance of ceramic membrane, *Ind. Eng. Chem. Res.*, 2018, **57**(10), 3773–3780.

342 N. Bakhtiari and S. Azizian, Adsorption of copper ion from aqueous solution by nanoporous MOF-5: a kinetic and equilibrium study, *J. Mol. Liq.*, 2015, **206**, 114–118.

343 Z. Rao, *et al.*, Surface decoration of amino-functionalized metal–organic framework/graphene oxide composite onto polydopamine-coated membrane substrate for highly efficient heavy metal removal, *ACS Appl. Mater. Interfaces*, 2017, **9**(3), 2594–2605.

344 T.-T. Zheng, *et al.*, A luminescent metal organic framework with high sensitivity for detecting and removing copper ions from simulated biological fluids, *Dalton Trans.*, 2017, **46**(8), 2456–2461.

345 N. M. Mahmoodi, *et al.*, Bio-based magnetic metal–organic framework nanocomposite: ultrasound-assisted synthesis and pollutant (heavy metal and dye) removal from aqueous media, *Appl. Surf. Sci.*, 2019, **480**, 288–299.

346 M. Garmsiri and H. R. Mortaheb, Enhancing performance of hybrid liquid membrane process supported by porous anionic exchange membranes for removal of cadmium from wastewater, *Chem. Eng. J.*, 2015, **264**, 241–250.

347 A. H. Dökmeci, Environmental impacts of heavy metals and their bioremediation, *Heavy Metals-Their Environmental Impacts and Mitigation*, IntechOpen, 2020.

348 H. Zhang and M. Reynolds, Cadmium exposure in living organisms: a short review, *Sci. Total Environ.*, 2019, **678**, 761–767.

349 R. A. Alani, *An Assessment of Drinking Water from Various Zip Codes in the Greater Houston Area for Potential Heavy Metal Contamination Using ICPMS*, Texas Southern University, 2022.

350 Y. Wang, *et al.*, A metal–organic framework and conducting polymer based electrochemical sensor for high performance cadmium ion detection, *J. Mater. Chem. A*, 2017, **5**(18), 8385–8393.

351 M. Roushani, Z. Saedi and Y. M. Baghelani, Removal of cadmium ions from aqueous solutions using TMU-16-NH$_2$ metal organic framework, *Environ. Nanotechnol., Monit. Manage.*, 2017, 7, 89–96.

352 Y. Wang, *et al.*, Functionalized metal–organic framework as a new platform for efficient and selective removal of cadmium(II) from aqueous solution, *J. Mater. Chem. A*, 2015, **3**(29), 15292–15298.

353 E. Rahimi and N. Mohaghegh, Removal of toxic metal ions from sungun acid rock drainage using mordenite zeolite, graphene nanosheets, and a novel metal–organic framework, *Mine Water Environ.*, 2016, **35**(1), 18.

354 S. Hou, *et al.*, Green synthesis and evaluation of an iron-based metal–organic framework MIL-88B for efficient

decontamination of arsenate from water, *Dalton Trans.*, 2018, **47**(7), 2222–2231.

355 C. O. Audu, *et al.*, The dual capture of As(v) and As(iii) by UiO-66 and analogues, *Chem. Sci.*, 2016, **7**(10), 6492–6498.

356 K. Leus, *et al.*, Removal of arsenic and mercury species from water by covalent triazine framework encapsulated γ-Fe$_2$O$_3$ nanoparticles, *J. Hazard. Mater.*, 2018, **353**, 312–319.

357 W. Yu, *et al.*, Metal–organic framework (MOF) showing both ultrahigh As(v) and As(iii) removal from aqueous solution, *J. Solid State Chem.*, 2019, **269**, 264–270.

358 M. Lu, *et al.*, Highly efficient removal of Pb^{2+} by a sandwich structure of metal–organic framework/GO composite with enhanced stability, *New J. Chem.*, 2019, **43**(2), 1032–1037.

359 M. A. Karimi, *et al.*, Highly efficient removal of toxic lead ions from aqueous solutions using a new magnetic metal–organic framework nanocomposite, *J. Chin. Chem. Soc.*, 2019, **66**(10), 1327–1335.

360 Y. Wu, *et al.*, Synthesis of two novel H$_4$TCPBDA-based metal–organic frameworks and their application in lead ion adsorption, *J. Mater. Sci.*, 2019, **54**(3), 2093–2101.

361 C. Lei, *et al.*, Fabrication of metal–organic frameworks@ cellulose aerogels composite materials for removal of heavy metal ions in water, *Carbohydr. Polym.*, 2019, **205**, 35–41.

362 G.-P. Li, *et al.*, Thiol-functionalized pores via post-synthesis modification in a metal–organic framework with selective removal of Hg(ii) in water, *Inorg. Chem.*, 2019, **58**(5), 3409–3415.

363 L. Fu, *et al.*, Post-modification of UiO-66-NH$_2$ by resorcyl aldehyde for selective removal of Pb(ii) in aqueous media, *J. Cleaner Prod.*, 2019, **229**, 470–479.

364 Z. Shi, *et al.*, Magnetic metal organic frameworks (MOFs) composite for removal of lead and malachite green in wastewater, *Colloids Surf., A*, 2018, **539**, 382–390.

365 Y.-H. Zou, *et al.*, A mesoporous cationic metal–organic framework with a high density of positive charge for enhanced removal of dichromate from water, *Dalton Trans.*, 2019, **48**(20), 6680–6684.

366 Y. Zheng, *et al.*, A facile fabrication of MOF for selective removal of chromium(iii) from aqueous solution, *J. Dispersion Sci. Technol.*, 2019, **40**(6), 918–924.

367 J. Li, *et al.*, Synthesis of highly porous inorganic adsorbents derived from metal–organic frameworks and their application in efficient elimination of mercury(ii), *J. Colloid Interface Sci.*, 2018, **517**, 61–71.

368 C. Yu, *et al.*, Efficient and selective removal of copper(ii) from aqueous solution by a highly stable hydrogen-bonded metal–organic framework, *Cryst. Growth Des.*, 2018, **18**(5), 3082–3088.

369 C. Liu, *et al.*, Ultrafast Removal of Cadmium(ii) by Green Cyclodextrin Metal–Organic-Framework-Based Nanoporous Carbon: Adsorption Mechanism and Application, *Chem. – Asian J.*, 2019, **14**(2), 261–268.

370 E. Martínez-Ahumada, *et al.*, MOF Materials for the Capture of Highly Toxic H$_2$S and SO$_2$, *Organometallics*, 2020, **39**(7), 883–915.

371 A. O. Yazaydın, *et al.*, Screening of metal–organic frameworks for carbon dioxide capture from flue gas using a combined experimental and modeling approach, *J. Am. Chem. Soc.*, 2009, **131**(51), 18198–18199.

372 C. Petit and T. J. Bandosz, Exploring the coordination chemistry of MOF-graphite oxide composites and their applications as adsorbents, *Dalton Trans.*, 2012, **41**(14), 4027–4035.

373 A. M. Ebrahim and T. J. Bandosz, Effect of amine modification on the properties of zirconium–carboxylic acid based materials and their applications as NO$_2$ adsorbents at ambient conditions, *Microporous Mesoporous Mater.*, 2014, **188**, 149–162.

374 I.-H. Choi, *et al.*, Gas sorption properties of a new three-dimensional in-abdc mof with a diamond net, *Front. Mater.*, 2019, **6**, 218.

375 C. A. Fernandez, *et al.*, Gas-induced expansion and contraction of a fluorinated metal–organic framework, *Cryst. Growth Des.*, 2010, **10**(3), 1037–1039.

376 T. G. Glover, *et al.*, MOF-74 building unit has a direct impact on toxic gas adsorption, *Chem. Eng. Sci.*, 2011, **66**(2), 163–170.

377 C. Petit, *et al.*, Reactive adsorption of acidic gases on MOF/graphite oxide composites, *Microporous Mesoporous Mater.*, 2012, **154**, 107–112.

378 L. Hamon, *et al.*, Comparative study of hydrogen sulfide adsorption in the MIL-53(Al, Cr, Fe), MIL-47(V), MIL-100(Cr), and MIL-101(Cr) metal–organic frameworks at room temperature, *J. Am. Chem. Soc.*, 2009, **131**(25), 8775–8777.

379 L. Hamon, *et al.*, Molecular insight into the adsorption of H$_2$S in the flexible MIL-53(Cr) and rigid MIL-47(V) MOFs: infrared spectroscopy combined to molecular simulations, *J. Phys. Chem. C*, 2011, **115**(5), 2047–2056.

380 R. Kitaura, *et al.*, Porous coordination-polymer crystals with gated channels specific for supercritical gases, *Angew. Chem., Int. Ed.*, 2003, **42**(4), 428–431.

381 H. Dathe, *et al.*, Metal organic frameworks based on Cu^{2+} and benzene-1,3,5-tricarboxylate as host for SO$_2$ trapping agents, *C. R. Chim.*, 2005, **8**(3–4), 753–763.

382 O. J. García-Ricard and A. J. Hernández-Maldonado, Cu$_2$(pyrazine-2,3-dicarboxylate)$_2$(4,4'-bipyridine) porous coordination sorbents: activation temperature, textural properties, and CO$_2$ adsorption at low pressure range, *J. Phys. Chem. C*, 2010, **114**(4), 1827–1834.

383 Z. Zhao, Z. Li and Y. Lin, Adsorption and diffusion of carbon dioxide on metal–organic framework (MOF-5), *Ind. Eng. Chem. Res.*, 2009, **48**(22), 10015–10020.

384 B. Xiao, *et al.*, High-capacity hydrogen and nitric oxide adsorption and storage in a metal–organic framework, *J. Am. Chem. Soc.*, 2007, **129**(5), 1203–1209.

385 J. A. Mason, *et al.*, Evaluating metal–organic frameworks for post-combustion carbon dioxide capture via temperature swing adsorption, *Energy Environ. Sci.*, 2011, **4**(8), 3030–3040.

386 H. Li, *et al.*, Incorporation of alkylamine into metal–organic frameworks through a Brønsted acid–base
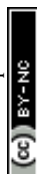
reaction for CO_2 capture, *ChemSusChem*, 2016, **9**(19), 2832–2840.

387 Y. L. Huang, L. Jiang and T. B. Lu, Modulation of gas sorption properties through cation exchange within an anionic metal–organic framework, *ChemPlusChem*, 2016, **81**(8), 780–785.

388 A. O. Yazaydın, *et al.*, Enhanced CO_2 adsorption in metal–organic frameworks via occupation of open-metal sites by coordinated water molecules, *Chem. Mater.*, 2009, **21**(8), 1425–1430.

389 P. D. Dietzel, V. Besikiotis and R. Blom, Application of metal–organic frameworks with coordinatively unsaturated metal sites in storage and separation of methane and carbon dioxide, *J. Mater. Chem.*, 2009, **19**(39), 7362–7370.

390 S. R. Caskey, A. G. Wong-Foy and A. J. Matzger, Dramatic tuning of carbon dioxide uptake via metal substitution in a coordination polymer with cylindrical pores, *J. Am. Chem. Soc.*, 2008, **130**(33), 10870–10871.

391 H. Furukawa, *et al.*, Ultrahigh porosity in metal–organic frameworks, *Science*, 2010, **329**(5990), 424–428.

392 P. L. Llewellyn, *et al.*, High uptakes of CO_2 and CH_4 in mesoporous metal organic frameworks MIL-100 and MIL-101, *Langmuir*, 2008, **24**(14), 7245–7250.

393 J. R. Karra and K. S. Walton, Effect of open metal sites on adsorption of polar and nonpolar molecules in metal–organic framework Cu-BTC, *Langmuir*, 2008, **24**(16), 8620–8626.

394 D. Britt, D. Tranchemontagne and O. M. Yaghi, Metal–organic frameworks with high capacity and selectivity for harmful gases, *Proc. Natl. Acad. Sci. U. S. A.*, 2008, **105**(33), 11623–11627.

395 C. Monahan, *et al.*, Antibiotic residues in the aquatic environment–current perspective and risk considerations, *J. Environ. Sci. Health, Part A: Toxic/Hazard. Subst. Environ. Eng.*, 2021, **56**(7), 733–751.

396 J. Wilkinson, *et al.*, Occurrence, fate and transformation of emerging contaminants in water: an overarching review of the field, *Environ. Pollut.*, 2017, **231**, 954–970.

397 F. Hooriabad Saboor, *et al.*, The effectiveness of MOFs for the removal of pharmaceuticals from aquatic environments: a review focused on antibiotics removal, *Chem. – Asian J.*, 2022, **17**(4), e202101105.

398 M. Stylianou, *et al.*, Adsorption and removal of seven antibiotic compounds present in water with the use of biochar derived from the pyrolysis of organic waste feedstocks, *J. Environ. Chem. Eng.*, 2021, **9**(5), 105868.

399 P. Song, *et al.*, Electrocoagulation treatment of arsenic in wastewaters: a comprehensive review, *Chem. Eng. J.*, 2017, **317**, 707–725.

400 S. K. Mondal, A. K. Saha and A. Sinha, Removal of ciprofloxacin using modified advanced oxidation processes: kinetics, pathways and process optimization, *J. Cleaner Prod.*, 2018, **171**, 1203–1214.

401 K. Qin, *et al.*, A review of bismuth-based photocatalysts for antibiotic degradation: insight into the photocatalytic degradation performance, pathways and relevant mechanisms, *Environ. Res.*, 2021, **199**, 111360.

402 K.-W. Jung, J.-H. Kim and J.-W. Choi, Synthesis of magnetic porous carbon composite derived from metal–organic framework using recovered terephthalic acid from polyethylene terephthalate (PET) waste bottles as organic ligand and its potential as adsorbent for antibiotic tetracycline hydrochloride, *Composites, Part B*, 2020, **187**, 107867.

403 M. Lei, *et al.*, A water-stable Cd-MOF and corresponding MOF@ melamine foam composite for detection and removal of antibiotics, explosives, and anions, *Sep. Purif. Technol.*, 2022, **286**, 120433.

404 D. Mukherjee, *et al.*, Devising robust hydrophobic MOFs and its membrane for ultra-sensitive aqueous phase detection of antibiotics and toxic nitro-explosives and adsorption of TNP, *J. Environ. Chem. Eng.*, 2023, **11**(5), 110528.

405 J. Xia, Y. Gao and G. Yu, Tetracycline removal from aqueous solution using zirconium-based metal–organic frameworks (Zr-MOFs) with different pore size and topology: adsorption isotherm, kinetic and mechanism studies, *J. Colloid Interface Sci.*, 2021, **590**, 495–505.

406 Z.-h Yang, *et al.*, Mn-doped zirconium metal–organic framework as an effective adsorbent for removal of tetracycline and Cr(VI) from aqueous solution, *Microporous Mesoporous Mater.*, 2019, **277**, 277–285.

407 Y. Zhang, *et al.*, Synthesis of hierarchical-pore metal–organic framework on liter scale for large organic pollutants capture in wastewater, *J. Colloid Interface Sci.*, 2018, **525**, 39–47.

408 J. Jin, *et al.*, Cu and Co nanoparticles co-doped MIL-101 as a novel adsorbent for efficient removal of tetracycline from aqueous solutions, *Sci. Total Environ.*, 2019, **650**, 408–418.

409 W. Xiong, *et al.*, Metal–organic frameworks derived magnetic carbon-αFe/Fe$_3$C composites as a highly effective adsorbent for tetracycline removal from aqueous solution, *Chem. Eng. J.*, 2019, **374**, 91–99.

410 Y. Sun, *et al.*, Adsorptive removal of dye and antibiotic from water with functionalized zirconium-based metal organic framework and graphene oxide composite nanomaterial Uio-66-(OH)$_2$/GO, *Appl. Surf. Sci.*, 2020, **525**, 146614.

411 K. Wang, *et al.*, Highly effective pH-universal removal of tetracycline hydrochloride antibiotics by UiO-66-(COOH)$_2$/GO metal–organic framework composites, *J. Solid State Chem.*, 2020, **284**, 121200.

412 Y. Kong, *et al.*, Enhanced tetracycline adsorption using alginate-graphene-ZIF67 aerogel, *Colloids Surf., A*, 2020, **588**, 124360.

413 W. Mao, *et al.*, Efficient cobalt-based metal–organic framework derived magnetic Co@C-600 Nanoreactor for peroxymonosulfate activation and oxytetracycline degradation, *Colloids Surf., A*, 2022, **648**, 129234.

414 Y. Zhou, *et al.*, Simultaneous removal of tetracycline and norfloxacin from water by iron-trimesic metal–organic frameworks, *J. Environ. Chem. Eng.*, 2022, **10**(3), 107403.

415 G. Wu, et al., Magnetic copper-based metal organic framework as an effective and recyclable adsorbent for removal of two fluoroquinolone antibiotics from aqueous solutions, J. Colloid Interface Sci., 2018, 528, 360–371.

416 L. Lian, et al., Magnetic solid-phase extraction of fluoroquinolones from water samples using titanium-based metal–organic framework functionalized magnetic microspheres, J. Chromatogr. A, 2018, 1579, 1–8.

417 X. Guo, et al., Exploration of functional MOFs for efficient removal of fluoroquinolone antibiotics from water, Microporous Mesoporous Mater., 2019, 286, 84–91.

418 G. Chaturvedi, et al., Removal of fluoroquinolone drug, levofloxacin, from aqueous phase over iron based MOFs, MIL-100(Fe), J. Solid State Chem., 2020, 281, 121029.

419 N. Kim, et al., Effective sequestration of tetracycline and ciprofloxacin from aqueous solutions by Al-based metal organic framework and reduced graphene oxide immobilized alginate biosorbents, Chem. Eng. J., 2022, 450, 138068.

420 S. Li, X. Zhang and Y. Huang, Zeolitic imidazolate framework-8 derived nanoporous carbon as an effective and recyclable adsorbent for removal of ciprofloxacin antibiotics from water, J. Hazard. Mater., 2017, 321, 711–719.

421 Y. Yuan, et al., Preparation of konjac glucomannan-based zeolitic imidazolate framework-8 composite aerogels with high adsorptive capacity of ciprofloxacin from water, Colloids Surf., A, 2018, 544, 187–195.

422 S. E. Moradi, et al., Effective removal of ciprofloxacin from aqueous solutions using magnetic metal–organic framework sorbents: mechanisms, isotherms and kinetics, J. Iran. Chem. Soc., 2016, 13, 1617–1627.

423 Ş. S. Bayazit, et al., Preparation of magnetic MIL-101(Cr) for efficient removal of ciprofloxacin, Environ. Sci. Pollut. Res., 2017, 24, 25452–25461.

424 Y. Zhao, et al., Synergistic effect of electrostatic and coordination interactions for adsorption removal of cephalexin from water using a zirconium-based metal–organic framework, J. Colloid Interface Sci., 2020, 580, 256–263.

425 Y. Gao, et al., Understanding the adsorption of sulfonamide antibiotics on MIL-53s: metal dependence of breathing effect and adsorptive performance in aqueous solution, J. Colloid Interface Sci., 2019, 535, 159–168.

426 G. Cheng, et al., Surface imprinted polymer on a metal–organic framework for rapid and highly selective adsorption of sulfamethoxazole in environmental samples, J. Hazard. Mater., 2022, 423, 127087.

427 M. R. Azhar, et al., Excellent performance of copper based metal organic framework in adsorptive removal of toxic sulfonamide antibiotics from wastewater, J. Colloid Interface Sci., 2016, 478, 344–352.

428 X. Zhao, et al., A metal–organic framework with large 1-D channels and rich OH sites for high-efficiency chloramphenicol removal from water, J. Colloid Interface Sci., 2018, 526, 28–34.

429 L.-X. Yang, J.-C. E. Yang and M.-L. Fu, Magnetic CoFe$_2$O$_4$ nanocrystals derived from MIL-101(Fe/Co) for peroxymonosulfate activation toward degradation of chloramphenicol, Chemosphere, 2021, 272, 129567.

430 N. Lu, et al., Experimental and molecular docking investigation on metal–organic framework MIL-101(Cr) as a sorbent for vortex assisted dispersive micro-solid-phase extraction of trace 5-nitroimidazole residues in environmental water samples prior to UPLC-MS/MS analysis, Anal. Bioanal. Chem., 2016, 408, 8515–8528.

431 Y. Peng, et al., Flexibility induced high-performance MOF-based adsorbent for nitroimidazole antibiotics capture, Chem. Eng. J., 2018, 333, 678–685.

432 Z. Luo, et al., A 3D stable metal–organic framework for highly efficient adsorption and removal of drug contaminants from water, Polymers, 2018, 10(2), 209.

433 B. Wang, et al., Highly stable Zr(ıv)-based metal–organic frameworks for the detection and removal of antibiotics and organic explosives in water, J. Am. Chem. Soc., 2016, 138(19), 6204–6216.

434 M. S. Gaikwad and C. Balomajumder, Capacitive deionization for desalination using nanostructured electrodes, Anal. Lett., 2016, 49(11), 1641–1655.

435 S. Dutta, et al., Metal–organic frameworks for water desalination, Adv. Funct. Mater., 2023, 2304790.

436 Z. Wang, et al., Nanoarchitectured metal–organic framework/polypyrrole hybrids for brackish water desalination using capacitive deionization, Mater. Horiz., 2019, 6(7), 1433–1437.

437 M. Ding, et al., Bimetallic metal–organic framework derived porous carbon nanostructures for high performance membrane capacitive desalination, J. Mater. Chem. A, 2017, 5(13), 6113–6121.

438 M. Kadhom and B. Deng, Metal–organic frameworks (MOFs) in water filtration membranes for desalination and other applications, Appl. Mater. Today, 2018, 11, 219–230.

439 S. Xiong, et al., Novel thin film composite forward osmosis membrane of enhanced water flux and anti-fouling property with N-[3-(trimethoxysilyl) propyl] ethylenediamine incorporated, J. Membr. Sci., 2016, 520, 400–414.

440 D. L. Shaffer, et al., Forward osmosis: where are we now?, Desalination, 2015, 356, 271–284.

441 R. Dai, et al., Porous metal organic framework CuBDC nanosheet incorporated thin-film nanocomposite membrane for high-performance forward osmosis, J. Membr. Sci., 2019, 573, 46–54.

442 D. Ma, et al., Thin-film nanocomposite (TFN) membranes incorporated with super-hydrophilic metal–organic framework (MOF) UiO-66: toward enhancement of water flux and salt rejection, ACS Appl. Mater. Interfaces, 2017, 9(8), 7523–7534.

443 A. Zirehpour, A. Rahimpour and M. Ulbricht, Nano-sized metal organic framework to improve the structural properties and desalination performance of thin film composite forward osmosis membrane, J. Membr. Sci., 2017, 531, 59–67.

444 S. Lin and M. Elimelech, Kinetics and energetics trade-off in reverse osmosis desalination with different configurations, Desalination, 2017, 401, 42–52.

445 J. Duan, et al., High-performance polyamide thin-film-nanocomposite reverse osmosis membranes containing hydrophobic zeolitic imidazolate framework-8, J. Membr. Sci., 2015, 476, 303–310.

446 T. H. Lee, et al., ZIF-8 particle size effects on reverse osmosis performance of polyamide thin-film nanocomposite membranes: importance of particle deposition, J. Membr. Sci., 2019, 570, 23–33.

447 K. M. Gupta, K. Zhang and J. Jiang, Water desalination through zeolitic imidazolate framework membranes: significant role of functional groups, Langmuir, 2015, 31(48), 13230–13237.

448 H. M. Park, K. Y. Jee and Y. T. Lee, Preparation and characterization of a thin-film composite reverse osmosis membrane using a polysulfone membrane including metal–organic frameworks, J. Membr. Sci., 2017, 541, 510–518.

449 B. L. Bonnett, et al., PCN-222 metal–organic framework nanoparticles with tunable pore size for nanocomposite reverse osmosis membranes, ACS Appl. Mater. Interfaces, 2020, 12(13), 15765–15773.

450 I. H. Aljundi, Desalination characteristics of TFN-RO membrane incorporated with ZIF-8 nanoparticles, Desalination, 2017, 420, 12–20.

451 Y. Lin, Y. Chen and R. Wang, Thin film nanocomposite hollow fiber membranes incorporated with surface functionalized HKUST-1 for highly-efficient reverses osmosis desalination process, J. Membr. Sci., 2019, 589, 117249.

452 J. Zuo and T.-S. Chung, Metal–organic framework-functionalized alumina membranes for vacuum membrane distillation, Water, 2016, 8(12), 586.

453 M. R. S. Kebria, et al., Experimental and theoretical investigation of thin ZIF-8/chitosan coated layer on air gap membrane distillation performance of PVDF membrane, Desalination, 2019, 450, 21–32.

454 F. Yang, et al., Metal–organic frameworks supported on nanofiber for desalination by direct contact membrane distillation, ACS Appl. Mater. Interfaces, 2018, 10(13), 11251–11260.

455 Y.-y Zhao, et al., Impacts of metal–organic frameworks on structure and performance of polyamide thin-film nanocomposite membranes, ACS Appl. Mater. Interfaces, 2019, 11(14), 13724–13734.

456 N. Misdan, et al., CuBTC metal organic framework incorporation for enhancing separation and antifouling properties of nanofiltration membrane, Chem. Eng. Res. Des., 2019, 148, 227–239.

457 M. Navarro, et al., Thin-film nanocomposite membrane with the minimum amount of MOF by the Langmuir–schaefer technique for nanofiltration, ACS Appl. Mater. Interfaces, 2018, 10(1), 1278–1287.

458 H. Liu, et al., Enhanced dispersibility of metal–organic frameworks (MOFs) in the organic phase via surface modification for TFN nanofiltration membrane preparation, RSC Adv., 2020, 10(7), 4045–4057.

459 J. Zhu, et al., MOF-positioned polyamide membranes with a fishnet-like structure for elevated nanofiltration performance, J. Mater. Chem. A, 2019, 7(27), 16313–16322.

460 Z. Wang, et al., Nanoparticle-templated nanofiltration membranes for ultrahigh performance desalination, Nat. Commun., 2018, 9(1), 2004.

461 W. P. Lustig, et al., Metal–organic frameworks: functional luminescent and photonic materials for sensing applications, Chem. Soc. Rev., 2017, 46(11), 3242–3285.

462 Y. Wang, et al., Bioinspired design of ultrathin 2D bimetallic metal–organic-framework nanosheets used as biomimetic enzymes, Adv. Mater., 2016, 28(21), 4149–4155.

463 H. Xu, et al., Metal–organic framework nanosheets for fast-response and highly sensitive luminescent sensing of Fe^{3+}, J. Mater. Chem. A, 2016, 4(28), 10900–10905.

464 F. Su, et al., Two-dimensional zirconium-based metal–organic framework nanosheet composites embedded with Au nanoclusters: a highly sensitive electrochemical aptasensor toward detecting cocaine, ACS Sens., 2017, 2(7), 998–1005.

465 R. Li, et al., A rational self-sacrificing template route to metal–organic framework nanotubes and reversible vapor-phase detection of nitroaromatic explosives, Small, 2011, 8(2), 225–230.

466 H.-S. Wang, et al., Lanthanide-based metal–organic framework nanosheets with unique fluorescence quenching properties for two-color intracellular adenosine imaging in living cells, NPG Asia Mater., 2017, 9(3), e354.

467 L. J. Han, et al., A Highly Solvent-Stable Metal–Organic Framework Nanosheet: Morphology Control, Exfoliation, and Luminescent Property, Small, 2018, 14(17), 1703873.

468 X. Xin, et al., Fluorescence turn-on detection of uric acid by a water-stable metal–organic nanotube with high selectivity and sensitivity, J. Mater. Chem. C, 2017, 5(3), 601–606.

469 W.-J. Song, Intracellular DNA and microRNA sensing based on metal–organic framework nanosheets with enzyme-free signal amplification, Talanta, 2017, 170, 74–80.

470 Z.-Q. Li, et al., Fabrication of nanosheets of a fluorescent metal–organic framework $[Zn(BDC)(H_2O)]_n$ (BDC = 1,4-benzenedicarboxylate): ultrasonic synthesis and sensing of ethylamine, Inorg. Chem. Commun., 2008, 11(11), 1375–1377.

471 A. K. Chaudhari, et al., Optochemically responsive 2D nanosheets of a 3D metal–organic framework material, Adv. Mater., 2017, 29(27), 1701463.

472 M. Tian, et al., Synthesis of large and uniform Cu_3TCPP truncated quadrilateral nano-flake and its humidity sensing properties, RSC Adv., 2016, 6(92), 88991–88995.

473 M. Zhao, et al., Ultrathin 2D metal–organic framework nanosheets, Adv. Mater., 2015, 27(45), 7372–7378.

474 S. A. Younis, et al., Metal–organic framework as a photocatalyst: progress in modulation strategies and environmental/energy applications, Prog. Energy Combust. Sci., 2020, 81, 100870.

475 T. Zhang, et al., Modulating photoelectronic performance of metal–organic frameworks for premium photocatalysis, Coord. Chem. Rev., 2019, 380, 201–229.

476 B. Mu and A. Wang, Adsorption of dyes onto palygorskite and its composites: a review, J. Environ. Chem. Eng., 2016, 4(1), 1274–1294.

477 D.-M. Chen, et al., An acid-base resistant polyoxometalate-based metal–organic framework constructed from {Cu₄Cl}⁷⁺ and {Cu₂(CO₂)₄} clusters for photocatalytic degradation of organic dye, J. Solid State Chem., 2020, 287, 121384.

478 N. M. Mahmoodi and J. Abdi, Nanoporous metal–organic framework (MOF-199): synthesis, characterization and photocatalytic degradation of Basic Blue 41, Microchem. J., 2019, 144, 436–442.

479 Y. Gao, et al., Accelerated photocatalytic degradation of organic pollutant over metal–organic framework MIL-53(Fe) under visible LED light mediated by persulfate, Appl. Catal., B, 2017, 202, 165–174.

480 X. Zhang, et al., Functionalized metal–organic frameworks for photocatalytic degradation of organic pollutants in environment, Chemosphere, 2020, 242, 125144.

481 D. Tuncel and A. Ökte, Efficient photoactivity of TiO₂-hybrid-porous nanocomposite: effect of humidity, Appl. Surf. Sci., 2018, 458, 546–554.

482 C. Xue, et al., MIL-125 and NH₂–MIL-125 modified TiO₂ nanotube array as efficient photocatalysts for pollute degradation, Chem. Lett., 2018, 47(6), 711–714.

483 L. Li, et al., Fabrication of a novel type visible-light-driven heterojunction photocatalyst: metal-porphyrinic metal organic framework coupled with PW12/TiO₂, Chem. Eng. J., 2020, 386, 123955.

484 C. G. Daughton and T. A. Ternes, Pharmaceuticals and personal care products in the environment: agents of subtle change?, Environ. Health Perspect., 1999, 107(6), 907–938.

485 M. Xu, et al., Occurrence and ecological risk of pharmaceuticals and personal care products (PPCPs) and pesticides in typical surface watersheds, China, Ecotoxicol. Environ. Saf., 2019, 175, 289–298.

486 Q. Chen, et al., Photocatalytic degradation of amoxicillin by carbon quantum dots modified K₂Ti₆O₁₃ nanotubes: effect of light wavelength, Chin. Chem. Lett., 2019, 30(6), 1214–1218.

487 J. Chen, et al., Multiple roles of Cu(II) in catalyzing hydrolysis and oxidation of β-lactam antibiotics, Environ. Sci. Technol., 2016, 50(22), 12156–12165.

488 N. Askari, et al., Fabrication of CuWO₄/Bi₂S₃/ZIF67 MOF: a novel double Z-scheme ternary heterostructure for boosting visible-light photodegradation of antibiotics, Chemosphere, 2020, 251, 126453.

489 X. Lei, et al., Constructing novel red phosphorus decorated iron-based metal organic framework composite with efficient photocatalytic performance, Appl. Surf. Sci., 2020, 528, 146963.

490 I. Sudano, et al., Nonsteroidal antiinflammatory drugs, acetaminophen, and hypertension, Curr. Hypertens. Rep., 2012, 14, 304–309.

491 T. Ding, et al., Toxicity, degradation and metabolic fate of ibuprofen on freshwater diatom Navicula sp, J. Hazard. Mater., 2017, 330, 127–134.

492 A. Gómez-Avilés, et al., Mixed Ti–Zr metal–organic-frameworks for the photodegradation of acetaminophen under solar irradiation, Appl. Catal., B, 2019, 253, 253–262.

493 W. Cao, et al., In-situ fabrication of g-C₃N₄/MIL-68(In)-NH₂ heterojunction composites with enhanced visible-light photocatalytic activity for degradation of ibuprofen, Chem. Eng. J., 2020, 391, 123608.

494 S. Miao, et al., Improved photocatalytic degradation of ketoprofen by Pt/MIL-125(Ti)/Ag with synergetic effect of Pt-MOF and MOF-Ag double interfaces: mechanism and degradation pathway, Chemosphere, 2020, 257, 127123.

495 L. Yue, et al., Adsorption–desorption behavior of atrazine on agricultural soils in China, J. Environ. Sci., 2017, 57, 180–189.

496 Y. Xue, et al., Efficient degradation of atrazine by BiOBr/UiO-66 composite photocatalyst under visible light irradiation: environmental factors, mechanisms and degradation pathways, Chemosphere, 2018, 203, 497–505.

497 Y. Liu, et al., The degradation behaviour, residue distribution, and dietary risk assessment of malathion on vegetables and fruits in China by GC-FPD, Food Control, 2020, 107, 106754.

498 H. Fakhri and H. Bagheri, Two novel sets of UiO-66@metal oxide/graphene oxide Z-scheme heterojunction: insight into tetracycline and malathion photodegradation, J. Environ. Sci., 2020, 91, 222–236.

499 F. Ghanbari and M. Moradi, Application of peroxymonosulfate and its activation methods for degradation of environmental organic pollutants, Chem. Eng. J., 2017, 310, 41–62.

500 S. S. Chen, et al., De Novo synthesis of platinum-nanoparticle-encapsulated UiO-66-NH₂ for photocatalytic thin film fabrication with enhanced performance of phenol degradation, J. Hazard. Mater., 2020, 397, 122431.

501 R. M. Abdelhameed, M. Abu-Elghait and M. El-Shahat, Hybrid three MOFs composites (ZIF-67@ZIF-8@MIL-125-NH₂): enhancement the biological and visible-light photocatalytic activity, J. Environ. Chem. Eng., 2020, 8(5), 104107.

502 S. Zhang, et al., Surface-defect-rich mesoporous NH₂–MIL-125(Ti)@Bi₂MoO₆ core-shell heterojunction with improved charge separation and enhanced visible-light-driven photocatalytic performance, J. Colloid Interface Sci., 2019, 554, 324–334.

503 Y. Li, et al., Construction of g-C₃N₄/PDI@MOF heterojunctions for the highly efficient visible light-driven degradation of pharmaceutical and phenolic micropollutants, Appl. Catal., B, 2019, 250, 150–162.

504 H. Wang, et al., Synthesis and applications of novel graphitic carbon nitride/metal–organic frameworks mesoporous photocatalyst for dyes removal, Appl. Catal., B, 2015, 174, 445–454.

505 R. Bariki, et al., Facile synthesis and photocatalytic efficacy of UiO-66/CdIn₂S₄ nanocomposites with flowerlike 3D-microspheres towards aqueous phase decontamination of triclosan and H₂ evolution, Appl. Catal., B, 2020, 270, 118882.

506 Y. Tang, et al., Anatase TiO₂@MIL-101(Cr) nanocomposite for photocatalytic degradation of bisphenol A, Colloids Surf., A, 2020, 596, 124745.